Meddelanden från Stockholms universitets
institution för geologiska vetenskaper No 388

2023/24-Estonia
– Analysis of material deposited near a fracture on the MS *Estonia* shipwreck

Christophe Dupraz, Susanne Sjöberg, Julie Boisard, Courtney Stairs, Viktor Sjöberg,
Pieter T. Visscher, Andreas Karlsson, Haoyi Yao, and Bert Allard

Stockholm 2024

Front Page: Fracture on the starboard side of the MS Estonia shipwreck. Picture taken by Ocean Discovery AB during the summer 2022 expedition.

Meddelanden
från
Stockholms universitets institution
för
geologiska vetenskaper
No 388

2023/24-Estonia
– Analysis of material deposited near a fracture on the MS *Estonia* shipwreck

Christophe Dupraz[a], Susanne Sjöberg[a], Julie Boisard[b], Courtney Stairs[b], Viktor Sjöberg[c], Pieter T. Visscher[d], Andreas Karlsson[e], Haoyi Yao[a], and Bert Allard[c].

[a] *Department of Geological Sciences, Stockholm University, Sweden*
[b] *Department of Biology, Lund University, Sweden*
[c] *Man-Technology-Environment Research Centre (MTM) Örebro University, Sweden*
[d] *Department of Marine Sciences, University of Connecticut, USA*
[e] *Swedish Museum of Natural History, Stockholm, Sweden*

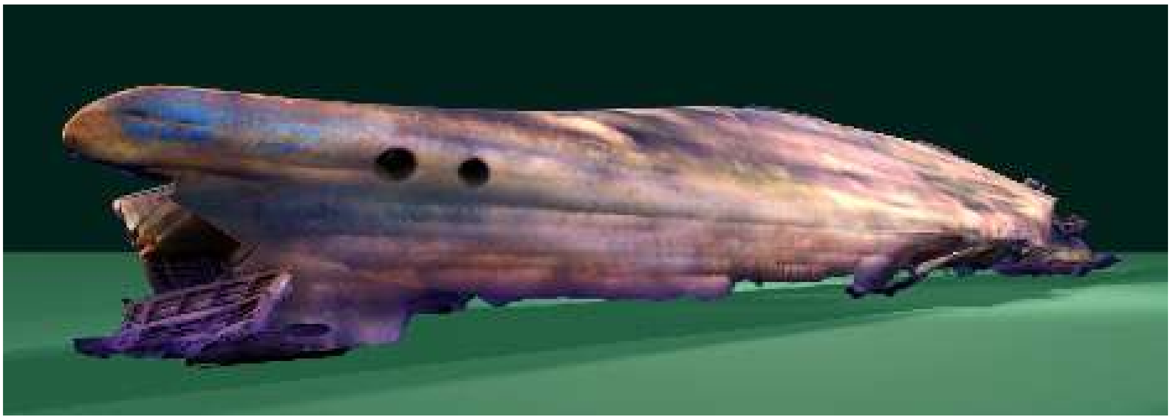

Photos from https://estonia.shk.se/en/3d-model

CONTENTS

ACKNOWLEDGMENTS

We thank the Master of the vessel Finn Gaute Harsjöen and the crews of the Viking Reach, the Offshore manager Bjarte Christiansen of Reach Subsea AS, and the Swedish Accident Investigation Authority for organizing the expedition and collecting the samples. The Swedish Accident Investigation Authority and the Estonian Safety Investigation Bureau provided key background information and feedback throughout the project, which is gratefully acknowledged. Draupnir Einarsson is thanked for cutting and preparing the steel samples. We thank Christoph Neururer and Alexandre Salzmann from Fribourg University for their assistance in SEM-EDS and XRD analysis.

SUMMARY

The MS *Estonia* sank while traveling from Tallinn, Estonia, to Stockholm, Sweden, on September 28, 1994. The shipwreck now rests on the seabed approximately 53 km NW of the Estonian island Hiiuma. Film material from the Discovery+ documentary by Henrik Evertsson in September 2020 revealed a previously unnoticed hole in the starboard side hull. Photogrammetric documentation of the wreck conducted by Ocean Discovery in 2022 showed that this damage is part of a 22 m-long fracture ending in another hole. Surveys of the bottom conditions have demonstrated that the shipwreck is situated in a trench and flanked by exposed bedrock, which coincides with the location of the damage in the hull.

The Swedish Accident Investigation Authority (SHK) requested an investigation of material deposited on the hull of the MS *Estonia* shipwreck present at the front hole on the starboard side. Based on the summer 2022 expedition photo documentation, four main areas were identified: (1) A reference area covered by uniform material seen throughout the shipwreck. (2) the upper fracture area with disrupted reference material, (3) the lower fracture area with steel bent inwards, mainly having a black color, (4) a beam resting on the seabed. In total, 13 locations within the areas were sampled. The mandate was to determine the sources of the components detected in this material based on a detailed characterization of elemental and mineralogical content, particle morphology, and microbial community composition.

The methodological approach included sequential acid leaching followed by ICP-MS for bulk elemental composition assessment and GC-IRMS for nutrient profiling (C, N, S). Phase analysis, morphological description, and associated chemical composition were conducted using X-ray diffraction and SEM-EDS analyses. Microbial diversity was determined through DNA extraction, rRNA gene sequencing, and subsequent taxonomic profiling.

The results of the investigation show that all detected sample components can be traced back to three known sources: the steel hull and its corrosion products, chemical components dissolved in the Baltic Sea water, and the sedimentary particles supplied from the surrounding bedrock and sediments. The samples were categorized into four groups reflecting the predominant material input sources: (1) Group 1 consists of reference samples serving as a baseline for comparison with other samples (2) Group 2 contains hull deposits that predominantly consist of clastic sediment supplied from the surrounding bedrock and sediments. (3) Group 3 contains hull deposits mainly comprising iron-rich phases indicative of in situ corrosion processes. These samples include steel fragments (pearlite) and traces of what likely is the hull paint. (4) Group 4 contains surface deposits collected from a beam resting on the sea floor, exhibiting a combined sedimentary and metallic signature.

The Group 2 samples are predominantly composed of siliciclastic sediment. The sporadic presence of iron-rich minerals indicates that the steel hull's contribution is negligible. Siliciclastic sediments are initially derived from contact with the adjacent bedrock and seafloor sediment. Over the course of thirty years, a complex interplay of sedimentary processes, including vigorous bottom currents, gravity-driven sediment flows, and fluctuations in thermohaline circulation patterns, all likely contributed to sediment resuspension, bringing it into contact with the ship hull. The composition of these samples is similar to reference sample H12, which was collected away from the damaged steel and likely reflects the condition of the intact hull. The metal-dominated samples (Groups 3 and 4) mainly reflect the steel composition and its corrosion products, as well as dissolved ions from the Baltic Sea water (e.g., SO_4^{2-}, HS^-, CO_3^{2-}), Ca^{2+}, and Mg^{2+}). Some of these samples are enriched in trace elements (e.g., Mn, Ni, Co, Cu, Cr) that predominantly originate from the hull's steel and are concentrated through selective leaching of iron during the corrosion process (enriching the rust deposits in trace elements). The detected sulfate-reducing bacteria likely enhance the selective leaching process and also concentrate trace elements in their biomass. Additionally, remnants of hull coatings (paint) may constitute a significant source of trace elements.

The damage inflicted to the hull at the fractured area removed the anticorrosion coating covering the steel, thus exposing the unprotected steel to seawater corrosion. The resulting corrosion products form three principal layers that vary in composition mainly as a function of the absence or presence of oxygen. (1) The biofouling layer colonizes most of the hull surface and is composed of macroscopic and microscopic encrusting eukaryotes and sediment (oxic environment). This zone produces the sediment-dominated samples (Group 2). (2) The outer corrosion layer in contact with oxygenated water is mainly composed of orange-brown Fe(III)-oxyhydroxides (lepidocrocite and goethite). These fully oxidized phases are only present in one Group 3 sample. (3) The black oxygen-depleted inner layer is directly in contact with the steel and is typically composed of Fe(II)-rich or a mixture of Fe(II) and Fe(III) corrosion products (e.g., various types of green rust (GR) and iron sulfides). This zone produces most of the Group 3 and 4 samples.

In conclusion, this study indicates that the deposits associated with the hole on the starboard side of the MS *Estonia* are the result of natural processes, including biofouling (microorganism accumulation on the steel surface), siliciclastic sediment incorporation, and natural corrosion of exposed steel. The predominantly black appearance of the corrosion layer is attributed to the documented dysoxic conditions at the seabed, favoring the formation of darker minerals like green rust and iron sulfides.

INTRODUCTION

The MS *Estonia* sank while traveling from Tallinn, Estonia, to Stockholm, Sweden, on September 28, 1994. The shipwreck lies at the bottom of the Baltic Sea, approximately 53 km NW of the Estonian island Hiiumaa (Jakobsson et al., 2021). Film material published in the Discovery+ documentary by Henrik Evertsson in September 2020, revealed a previously not observed hole in the hull on the starboard side of MS *Estonia*. Photogrammetry documentation of the wreck conducted by Ocean Discovery in 2022 showed that this damage is part of a 22 m-long fracture that runs from this position towards the stern. The hull is indented along the fracture and ends with another hole, closer to the stern. Surveys of the bottom conditions around the shipwreck identified exposed bedrock next to the damaged hull area (Jakobsson et al., 2021; Estonian Safety Investigation Bureau, 2023).

The present investigation was requested by the Swedish Accident Investigation Authority (SHK). The requested task consisted of analyzing material deposited on the hull of the MS *Estonia* shipwreck, observed in association with the front hole on the starboard side. In summary, material deposited in 13 locations close to the fracture was analyzed in terms of element content, microbial community composition, mineralogy, and particle morphology. A piece of steel, cut out from the sampled area, was also analyzed for reference purposes.

The objective of the conducted analyses was to identify the sources of components found in the sampled material. This expertise involved the participation of three working groups from three universities: Stockholm University, serving as the principal investigator, handled the initial sample treatment, phase analysis, and morphological characterization of the solid samples. Örebro University took on the chemical analysis of both the solid samples and the seawater. Lund University conducted the biochemical characterization of the microbial communities. Planning of the sampling expedition, including deciding the design of the sampling procedure, was conducted during a series of meetings in the spring of 2023. These meetings were chaired by the Swedish Accident Investigation Authority (SHK) and included participants from Reach Subsea and Stockholm University (SU).

SAMPLING AND METHOD

SITE DESCRIPTION AND SAMPLING AREA

The Baltic Sea is a brackish water basin with a stable halocline at approximately 60 to 80 m water depth (Fehr et al., 2010), conditions which are confirmed to prevail in the area around the MS *Estonia* (Jakobsson et al., 2021; Estonian Safety Investigation Bureau, 2023). The boundary between oxic and anoxic water layers coincides with the halocline and was found at 75 m depth during the summer 2022 expedition (Jakobsson et al., 2021). The shallowest part of the shipwreck is located at a depth of around 57 m, where the water is relatively well oxidized, while the deeper parts of the wreck are situated in mainly anoxic (absence of oxygen) to dysoxic (oxygen below 2ml/l) water (Jakobsson et al., 2021). However, measurements carried out over a longer time period show that oxygen concentrations close to the seabed are highly variable and thus creating alternating oxic-anoxic conditions (Estonian Safety Investigation Bureau, 2023). In addition, the shipwreck is thought to have moved over the years,

MS *Estonia* is 155 m long and 24 m wide, and there are two major deformation zones located 69 m and 89 m, respectively, from the stern, making the total area of deformation at least 22 m long (Estonian Safety Investigation Bureau, 2023). The requested task consisted of analyzing material deposited on the hull of the MS *Estonia* shipwreck, observed in association with the front hole on the starboard side (Fig. 1). The sampling site is located close to the seabed at a water depth of 79 to 81 m, and thus situated in the deeper anoxic to dysoxic zone. However, since the shipwreck is thought to have moved over the years, an alternating oxic-anoxic environment can not be excluded. At this site the ship rests in a trench, bordered by exposed bedrock (Jakobsson et al., 2021). The indentation in the hull, located on the western side of the investigated fracture, is found to correspond well with the positioning of exposed bedrock (Estonian Safety Investigation Bureau, 2023). Based on photo documentation that was carried out during the summer of 2022 expedition, four main areas of were identified: (1) a reference area seemingly covered by the same material observed all over the shipwreck, (2) the upper fracture area where the material in the reference area appears to be disrupted, (3) the lower area which mainly has a black color and where parts of the steel is bent inwards, and (4) a beam resting on the seabed. In total, material deposited on 13 locations within this area was collected (Fig. 2 and 3).

HULL SAMPLES

A remotely operated underwater vehicle (ROV) equipped with a suction sampler (Bluefield Geoservices, UK) was used for collecting material attached to the hull of the MS *Estonia* shipwreck. A pump and filter carousel were mounted on the (ROV). The carousel magazine contained seven compartments of which six were equipped with 26 µm filters (Bluefield, filter screen material type: 304 Stainless Steel). Filter screen composition is given in Table 1. The seventh container was left empty and used for flushing. Between each sampling position, the carousel was driven to the empty compartment where the pump was used to flush the hoses. Then the carousel rotated to the next filter in turn. The ROV manipulator arm was used to move the suction arm into position and left to suck 2-3 seconds, collecting sample material into the filter containers. Sampling positions and suction sampling method are shown in Fig. 1–5. The filters (pore size 26 µm), containing the collected samples, were then placed in sample containers, sealed *in-situ* and brought back to the surface. The samples that were collected are listed in Table 2. Sample descriptions are based on ocular inspection of the samples before analyses, and grain sizes are defined according to Wentworth (1922).

Table 1. Filter screen composition: Type 304 (UNS S30400) stainless steel (World Material, 2024).

Element	wt.%
C	≤0.07
Si	≤0.75
Mn	≤2.00
P	≤0.045
S	≤0.03
Cr	17.5 - 19.5
Ni	8.0 - 10.5
N	≤0.1
Fe	Balance

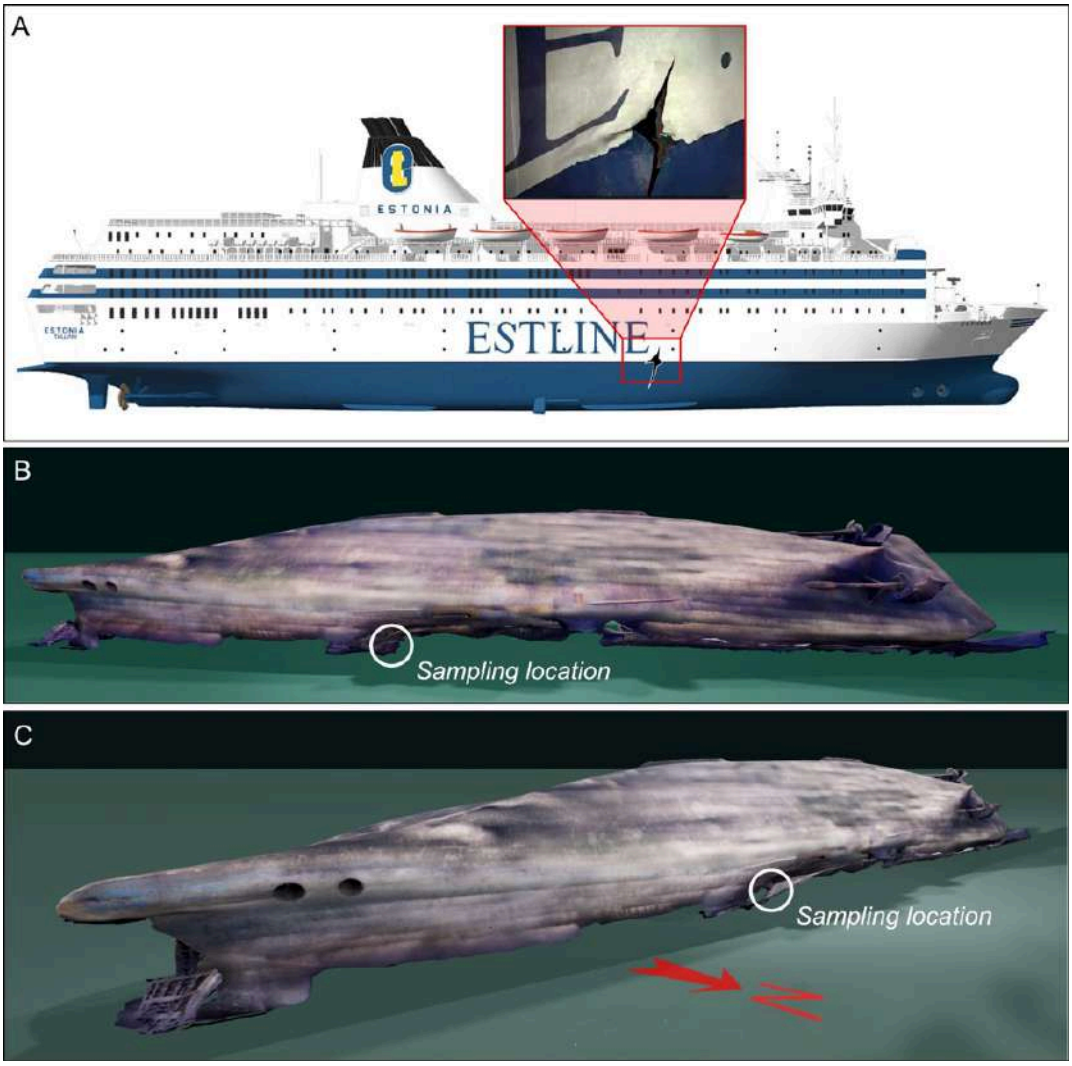

Figure 1. Location of the sampling area (photos modified from photo documentation by Ocean Discovery AB, https://estonia.shk.se/en/ship).

At the surface on board the research vessel, the filters, containing the collected samples, were divided in two and placed in sterile 50 mL polypropylen tubes (Sarstedt). One set of samples was placed in -20°C and the other set in +4°C. Sample H13 was scraped off a cut out piece of the hull and collected in 2 ml cryotubes (VWR, article no. 479-1220, manufactured by Radnor Corporate Center for VWR, Radnor PA, USA) using sterile plastic/metal forceps. One 2 mL sample was put in -20°C and the other set in +4°C. All samples were delivered to the Department of Geological Sciences at Stockholm University in unbroken cold chains, -20°C and +4°C respectively. Upon return to the laboratory, the samples that were kept at +4°C were subsampled for element analyses and stored at 4°C until further analysis. Samples kept at -20°C were subsampled in the laboratory for DNA extraction, amplification and sequencing. These subsamples were transferred directly in to -80°C, where they were stored until analysis. Sampling data are given in Table 2. Sample descriptions are based on visual inspection of the samples before analyses, and grain sizes are defined according to Wentworth (1922).

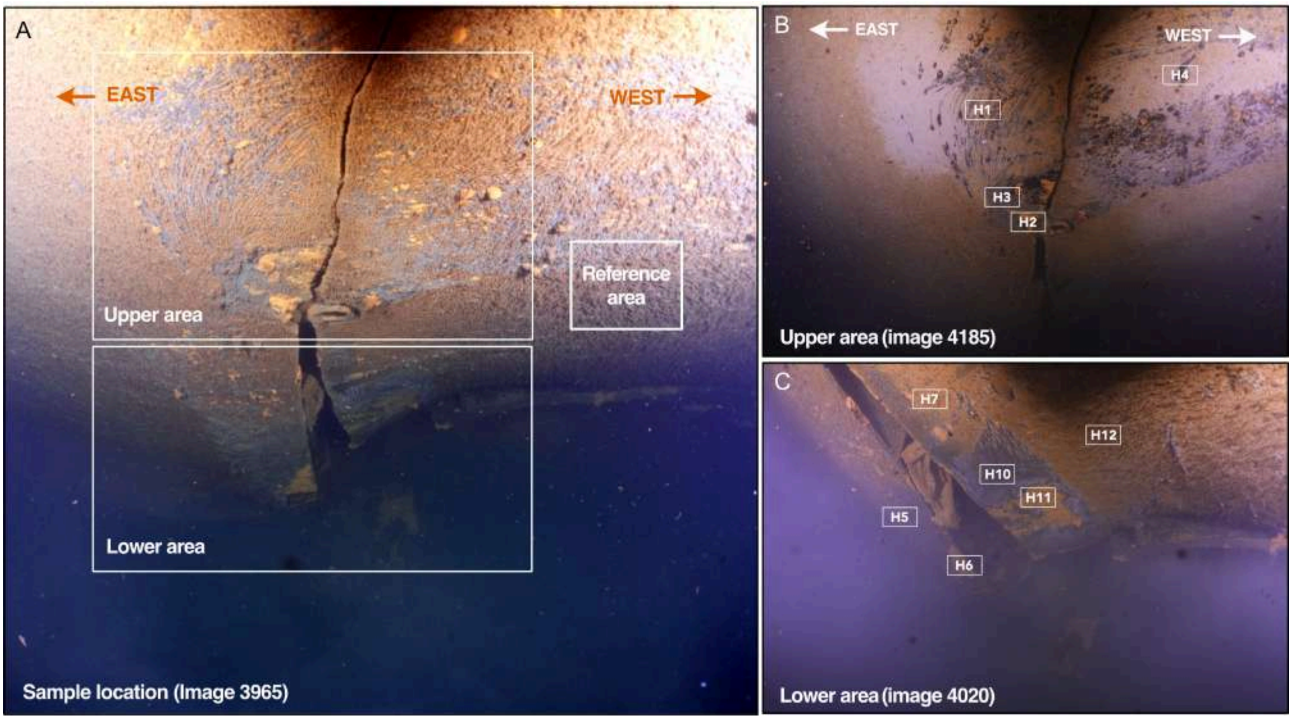

Figure 2. Detail of sampling location (see insert Fig. 1).

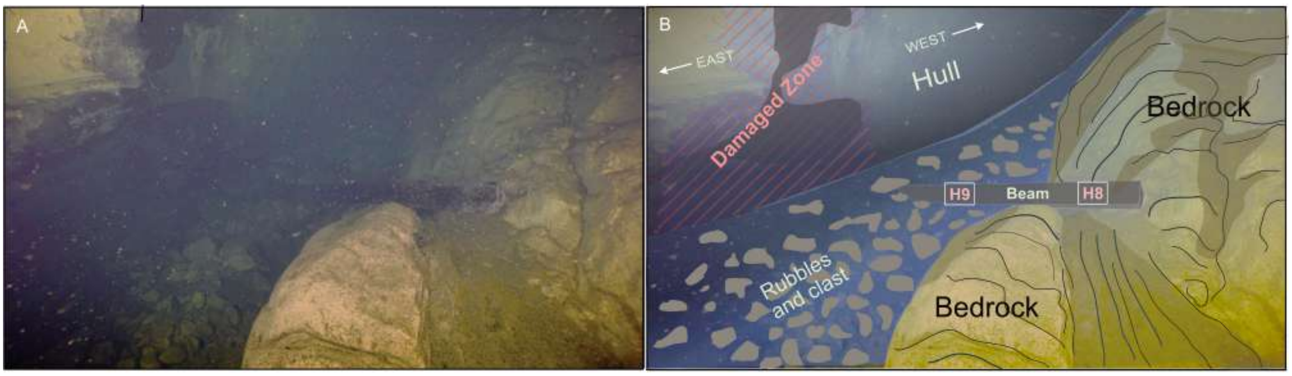

Figure 3. Photo showing the sampled beam resting on the seafloor and the exposed bedrock. The beam appears to have fallen out through the fracture from the interior of MS *Estonia* (photo modified from Jakobsson et al., 2021).

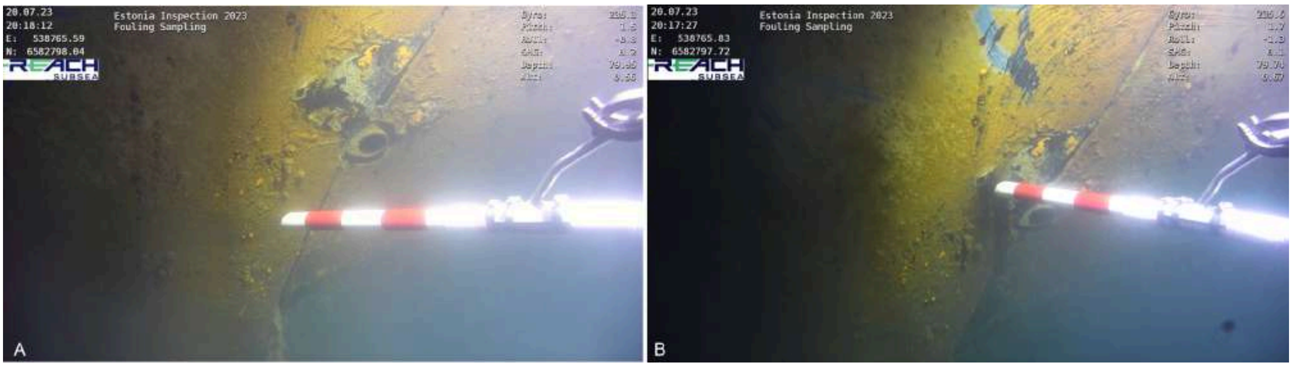

Figure 4. Photos showing the suction sampler (Bluefield Geoservices) attached to remotely operated underwater vehicle (ROV).

Cut-out steel plate

The steel plate was 670 mm long and 145 mm at the widest point (Fig. 5 and 6). Fig. 5 shows the fracture and indicates the location of the plate that was removed. At Stockholm University, an approximately 80 mm long piece of the plate was separated from the original plate using a band saw and thereafter subsampled, as shown in Fig. 6. The saw blade was cooled with compressed air to keep the heat generation to a minimum. Paint was not observed on the plate when visually inspected. The remaining portion was returned to the Swedish Accident Investigation Authority (SHK). The B-series of samples (Fig. 6) were washed in ethanol (99%) and used for elemental analyses and the A-series of samples were treated as follows and used for microscopy. A tap drill (Granlunds), with the tap removed, was used to cut out cylinders with a diameter of 4 mm from the steel samples. Washing with ethanol was conducted between each step. The steel cylinders were thereafter mounted in epoxy until further preparation for scanning electron microscopy coupled to energy-dispersive X-ray spectrometry.

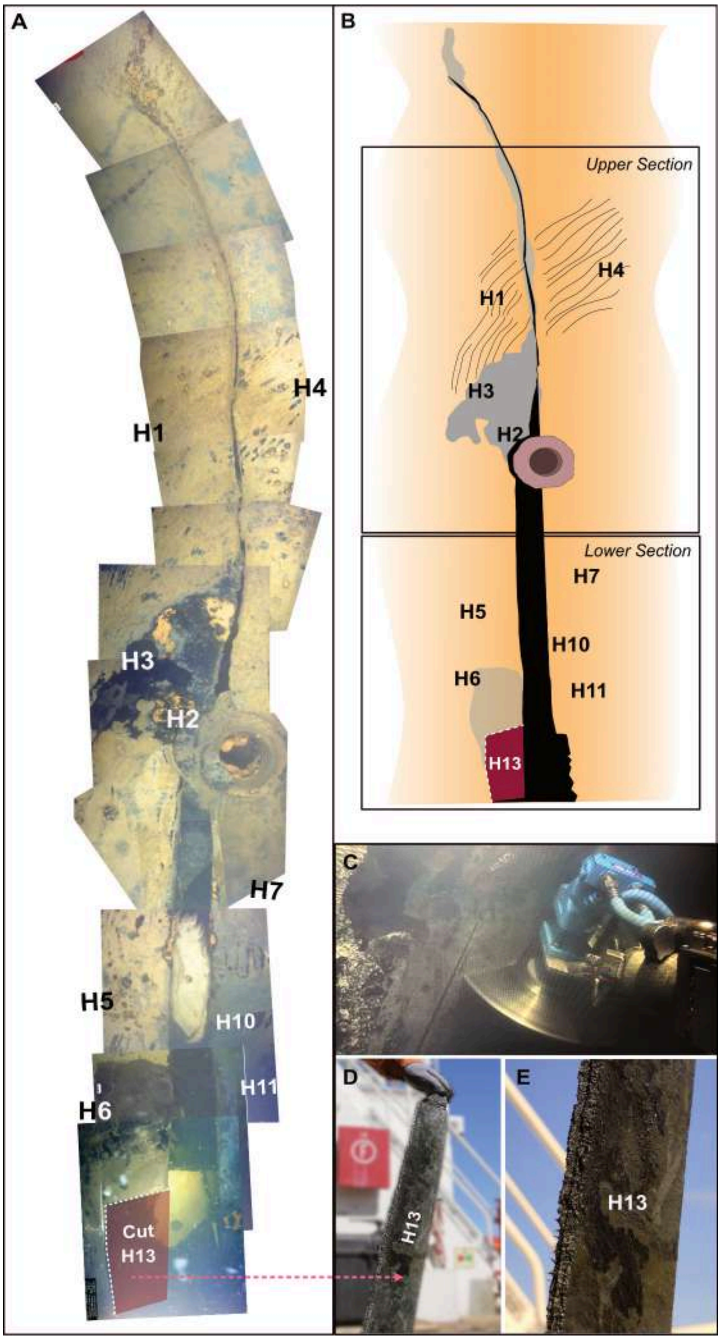

Figure 5. (A) Composite image extracted from the video 'Estonia examination starboard forward damage' (https://vimeo.com/872832997?share=copy), showing the entire length of the fracture with the sample location and the position from which the metal plate was cut out. **(B)** Sketch showing sampling locations. **(C)** Photo showing the steel plate being cut out from the hull. **(D)** The cut-out steel plate. **(E)** Close-up of (D).

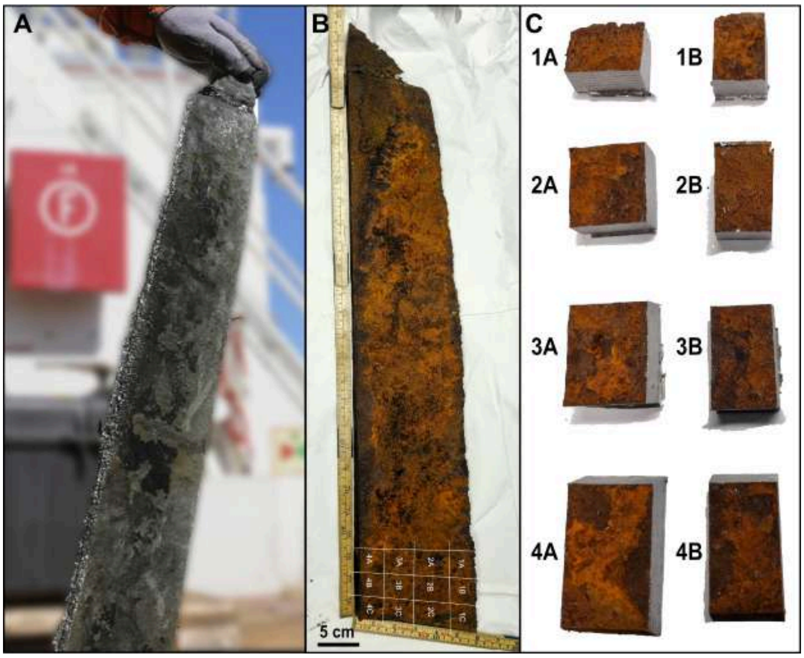

Figure 6. Subsampling of the cut-out steel plate. **(A)** Metal surface covered by black precipitates before and just as it was brought up to the fully oxygenated surface environment. **(B)** Metal surface after exposure to air. **(C)** Subsamples used for SEM-EDS analyses (1A-4A) and subsamples used for element analyses (1B-3B).

Table 2. Collected samples. The listed coordinates for sample locations are given with reference to Universal Transverse Mercator (UTM) zone 34N and WGS84. The coordinates represent the sample area as a whole (for details sample positions refer to Fig. 2, 3, 4.

Sample id.	*Water depth*	*Position (E, N)*	*Site description**	*Sample description*	*Method*
ES-23-H1	79 m	538766.40°, 6582798.12°	Site located in the upper area of the sampling zone, east of the fracture towards the bow.	Brownish gel-like sample containing medium to coarse grain sand particles.	Suction - collection of sample on filter.
ES-23-H2	79 m	538766.40°, 6582798.12°	Site located in the upper area of the sampling zone, east of the fracture towards the bow.	Brown-red muddy sample with medium sized black stray grains.	Suction - collection of sample on filter.
ES-23-H3	79 m	538766.40°, 6582798.12°	Site located in the upper area of the sampling zone, east of the fracture towards the bow.	Black-green sample forming flakes when drying.	Suction - collection of sample on filter.
ES-23-H4	79 m	538766.40°, 6582798.12°	Site located in the upper right area of the sampling zone, west of the fracture towards the stern.	Greyish clayey sample containing stray grains of medium grain sand.	Suction - collection of sample on filter.
ES-23-H5	80 m	538766.40°, 6582798.12°	Site located in the lower area of the sampling zone, east of the fracture towards the bow.	Brownish medium grain sand containing black stray grains.	Suction - collection of sample on filter.
ES-23-H6	80 m	538766.40°, 6582798.12°	Site located in the lower area of the sampling zone, east of the fracture towards the bow.	Brown-red medium grain sand.	Suction - collection of sample on filter.
ES-23-H7	80 m	538766.40°, 6582798.12°	Site located in the lower area of the sampling zone, west of the fracture towards the stern.	Brown-black fine grained sample forming threads of particles.	Suction - collection of sample on filter.
ES-23-H8	81 m	538766.40°, 6582798.12°	Beam resting on the seafloor below the fracture. Sample collected from the part of the beam furthest away from the ship.	Black fine grained sample with dark red aggregates of particles (possibly oxidized material).	Suction - collection of sample on filter.
ES-23-H9	81 m	538766.40°, 6582798.12°	Beam resting on the seafloor below the fracture. Sample collected from the part of the beam closest to the ship.	Black fine grained sample	Suction - collection of sample on filter.
ES-23-H10	80 m	538766.40°, 6582798.12°	Site located in the lower area of the sampling zone, west of the fracture towards the stern.	Black fine grained sample forming flakes when drying. Containing millimeter-ized brick red flakes (possibly oxidized material).	Suction - collection of sample on filter.
ES-23-H11	80 m	538766.40°, 6582798.12°	Site located in the lower area of the sampling zone, west of the fracture towards the stern.	Brown-black sample forming flakes when drying. Containing millimeter-sized brick red flakes (possibly oxidized material).	Suction - collection of sample on filter.
ES-23-H12	80 m	538766.40°, 6582798.12°	Site located in the lower area of the sampling zone, west of the fracture towards the stern.	Greyish fluffy mud-like sample containing stray grains of medium grain sand.	Suction - collection of sample on filter.
ES-23-H13	80 m	538766.40°, 6582798.12°	Sample scraped from steel plate cut out from the lower area of the sampling zone, east of the fracture towards the bow.	Black fine grained seemingly homogenous sample.	Scraped from steel plate cut out from the hull.
ES-23-S1-S4	80 m	538766.40°, 6582798.12°	Piece of steel cut out from the lower area of the sampling zone, east of the fracture towards the bow.	Greyish black surface that oxidizes in contact with air.	Piece of steel cut out from the hull.

** See Fig. 2 and 3 for sampling locations.*

WATER SAMPLES

Nalgene™ sterile analytical filter units (Thermo Fischer Scientific, article no 130-4020PK) were used for the recovery of microorganisms and particles (devices exceed recovery requirements set forth in ISO 7704). Cellulose nitrate (CN) membranes, 47 mm in diameter and 0.2 µm pore size. Filters were carefully placed in sterile 50 ml polypropylene tubes (Sarstedt Inc., Newton NC, USA).

Water samples used for elemental analyses were collected in sterile 50 ml polypropylene tubes (Sarstedt). Tubes were pre-rinsed with sample water before filling them with sample. Samples were acidified with concentrated nitric acid (HNO_3, suprapur) immediately after sampling and stored at 4°C.

GEOCHEMISTRY

LEACHING OF SAMPLES

Samples collected from the hull and beam surfaces (H-series of samples) were dried at room temperature until constant weight to remove the remaining seawater (Table 3). The samples were then dissolved in a two-step leaching procedure: (1) 65% HNO_3, liquid/solid ratio ca 10, and in sequence (2) 25% HF, 2 times, liquid/solid ratio ca 20; room temperature, 20 hrs. Samples from the cut-out steel plate (S-series) were leached with a 1:1 mixture of 65% HNO_3 and 37% HCl, liquid/solid ratio ca 20, room temperature, 20 hrs. All samples (H- and S-series) were completely dissolved except S1B (leaching of hole piece, initial weight 32.8 g), and the leachates were filtered (0.20 µm polypropylene syringe filter) prior to analysis (ICP-MS).

Table 3. Samples from the hull surface (dry sample weight).

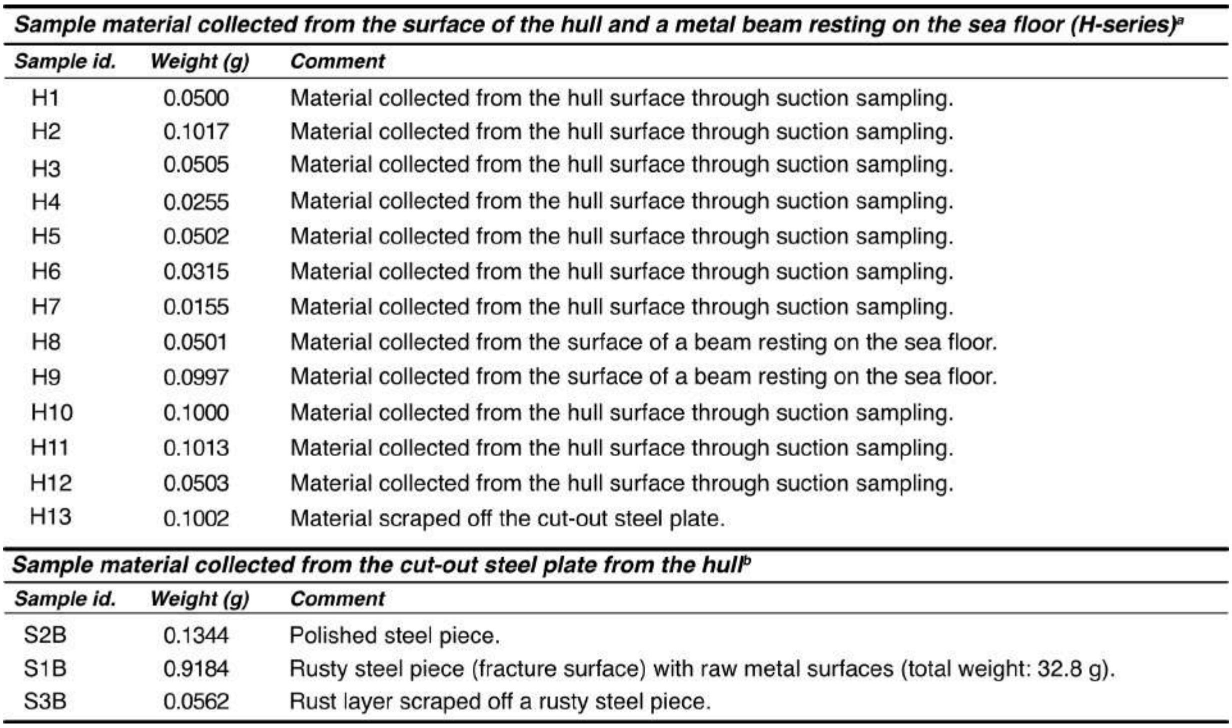

Sample material collected from the surface of the hull and a metal beam resting on the sea floor (H-series)[a]

Sample id.	*Weight (g)*	*Comment*
H1	0.0500	Material collected from the hull surface through suction sampling.
H2	0.1017	Material collected from the hull surface through suction sampling.
H3	0.0505	Material collected from the hull surface through suction sampling.
H4	0.0255	Material collected from the hull surface through suction sampling.
H5	0.0502	Material collected from the hull surface through suction sampling.
H6	0.0315	Material collected from the hull surface through suction sampling.
H7	0.0155	Material collected from the hull surface through suction sampling.
H8	0.0501	Material collected from the surface of a beam resting on the sea floor.
H9	0.0997	Material collected from the surface of a beam resting on the sea floor.
H10	0.1000	Material collected from the hull surface through suction sampling.
H11	0.1013	Material collected from the hull surface through suction sampling.
H12	0.0503	Material collected from the hull surface through suction sampling.
H13	0.1002	Material scraped off the cut-out steel plate.

Sample material collected from the cut-out steel plate from the hull[b]

Sample id.	*Weight (g)*	*Comment*
S2B	0.1344	Polished steel piece.
S1B	0.9184	Rusty steel piece (fracture surface) with raw metal surfaces (total weight: 32.8 g).
S3B	0.0562	Rust layer scraped off a rusty steel piece.

[a] *See Fig. 2 and 3.* [b] *See Fig. 6.*

ELEMENTAL ANALYSIS (ICP-MS AND GC-IRMS)

Elemental analysis was conducted using inductively coupled plasma mass-spectrometry (ICP-MS; Agilent 7500cx). Quantitative measurements of 29 elements using the Merck 10580 multielement standard was done in the range of 0.01 µg/L up to 10000 µg/L (Table 3). External calibration was conducted and ^{103}Rh was used as the internal standard for all measured elements. Quantitative results adjusted according to the internal standard were obtained using the provided software "MassHunter". Appropriate dilution of the samples prior to analysis was done using deionized water and 1% nitric acid.

Table 4. Concentration ranges for elements in the multielement standard.

Element	Range(µg/L)	Element	Range(µg/L)	Element	Range(µg/L)	Element	Range(µg/L)
^{107}Ag	0.01 - 100	^{59}Co	0.01 - 100	^{55}Mn	0.01 - 100	^{125}Te	0.01 - 100
^{27}Al	0.01 - 100	^{53}Cr	0.01 - 100	^{95}Mo	0.01 - 100	^{205}Tl	0.01 - 100
^{75}As*	0.1 - 1000	^{63}Cu$^{(*)}$	0.01 – 100	^{23}Na	0.01 – 100	^{238}U	0.01 – 100
^{138}Ba	0.01 – 100	^{56}Fe*	0.1 - 1000	^{60}Ni	0.01 - 100	^{51}V*	0.01 - 100
^{9}Be	0.1 - 1000	^{71}Ga	0.01 - 100	^{total}Pb	0.01 - 100	^{66}Zn	0.1 - 1000
^{209}Bi	0.01 - 100	^{39}K*	0.01 - 100	^{85}Rb	0.01 - 100		
^{43}Ca	1 - 10000	^{7}Li	0.01 - 100	^{82}Se*	0.1 - 1000		
^{111}Cd	0.01 - 100	^{24}Mg	0.01 - 100	^{88}Sr	0.01 - 100		

** Use of collision cell for interference correction. For Cu only on samples from digestion of steel samples.*
^{total} Measurement of 204, 206, 207 and 208 and using the total signal to account for possible isotope fractionation processes.

The ICP-MS instrument was equipped with a MicroMist nebulizer feed from a peristaltic pump at 0.1 rps using 0.89 ID tubing. A Scott double pass spray chamber was used to couple the nebulizer to the torch and was operating at 2°C. The plasma was working at 1500 W at a plasma-to-sampling cone distance of 8 mm. Carrier gas flow and make up gas flow were optimized at 0.90 and 0.20 L/min, respectively. Collision gas flow was optimized for iron to 5 mL/min and the same setting was used for the other 5 elements that was also analyzed in collision mode.

Concentrations of C, N and S were determined using a Thermo EA-Isolink CN Flash IRMS Elemental Analyzer for TOC, TC/TN and a Thermo EA-Isolink CNHOS Flash Elemental Analyzer for total CNS. The mortared sample powder (12 mg for organic carbon analyses and 10 mg for the remaining analyses) was placed in a silver (TOC) or tin capsule. All samples were prepared in triplicate: one set of samples was acidified with a total of 200 µL of 10% HCl and left to react and dry overnight at 60°C while the other set of samples were left untreated. The acidified samples were used to determine concentrations for total organic carbon (TOC) and the other two sets of samples were used to determine concentrations of (1) total carbon (TC) and total nitrogen (TN), and (2) total sulfur (TS). In total, concentrations of 5 mg/kg or higher were recorded for 25 elements (22 by ICP-MS), however not for Si and O. Concentration levels for Si (H-series) were assessed from SEM-EDS-spectra.

PHASE ANALYSIS AND MICROSCOPY

X-RAY DIFFRACTION

The mineral content of the samples was determined using X-ray powder diffraction analysis. A few drops of acetone were added to each sample (ES-23-H1 to ES-23-H13) and finely ground into a powder which was loaded on a PANalytical sample holder with a 27 mm diameter area. The sample was subsequently measured with a PANalytical XPERT-PRO diffractometer, using CuKα radiation from 5° to 70° 2θ with a step size of 0.001° 2θ at 40 mA and 45 kV and a spinning sample holder. Diffractograms were analyzed with PANalytical HighScore Plus software at Stockholm University and with PDXL 2 software package from Rigaku using the International Centre for Diffraction Data (ICDD) PDF-4+ database at Fribourg University.

SCANNING ELECTRON MICROSCOPY (SEM) – ENERGY DISPERSIVE SPECTROSCOPY (EDS)

Scanning electron microscopy analyses were conducted at the Swedish Museum of Natural History, Stockholm and Fribourg University. In Stockholm, samples were imaged using a Thermo Fisher (previously FEI) Quanta FEG (field emission gun) 650 scanning electron microscope (SEM). SEM images of a specimen were taken using a backscattered electron (BSE) detector). Accelerating voltage was set to 20kV and working distance to 10 mm. The SEM fitted with an Oxford Instruments X-Max (80mm^2) energy dispersive X-ray spectroscopy (EDS) was used to retrieve chemical information; the beam current was calibrated against Co metal, which in turn were calibrated against natural and synthetic minerals and metals for each respective element This allowed coupling of morphologies and structures to elemental composition. The analyses were conducted in low vacuum (~7 x 10^{-1} mbar) to reduce charging, which permits the use of uncoated samples. Sample H1 to H13 were transferred from the anoxic sample vials to stubs covered by carbon tape and directly placed in the low vacuum chamber. The influence of oxygen on samples should therefore be limited. In addition, steel plate samples and sample H13, which was scraped off the steel plate, were mounted in epoxy and polished to enable observation of cross-sections. Microscopy preparation was done by water cooled grinding down to mesh 1200 SiC paper followed by diamond polishing down to 1 µm and analyses were conducted in high vacuum. Element analyses were conducted using AZtec 6.1software and normalized to 100%. Since particles are small, the surrounding matrix may contribute to the elemental signal and should be considered as a possible source of error. In Fribourg, samples were visualized with a scanning electron microscope FEI XL30 Sirion FEG (Thermo Fisher Scientific, Waltham, MA, USA) in the Department of Geosciences, University of Fribourg, Switzerland. This microscope is equipped with an EDAX NEW-XL30 EDS detector (FEI Com- pant, Hillsboro, OR, USA). This technique was also used to produce element maps of specific sample regions (25 kV, 12 nA, dwell time 50 ms per pixel, 5 lm spot size).

MICROBIOLOGY

DNA extraction

Nalgene™ sterile analytical filter units (Thermo Fischer Scientific, article no 130-4020PK) with Cellulose nitrate (CN) membranes (47 mm in diameter and 0.2 µm pore size) were used for the recovery of microorganisms and particles. Filtered particles were scraped from CN membranes and stored in sterile low-binding 1.5 ml Microcentrifuge Tubes (VWR; article no 525-1493) at -20°, awaiting further processing. CN membranes were stored in sterile 15 ml polypropylene tubes (Sarstedt Inc., Newton NC, USA) and stored at -20° alongside the filtrate. DNA from 40-560 mg of the recovered particles was extracted using DNeasy PowerLyzer PowerSoil Kit (Qiagen, article no 12855-50). DNA was quantified with Thermo Scientific™ NanoDrop™ One.

Table 5. DNA extraction and quantification.

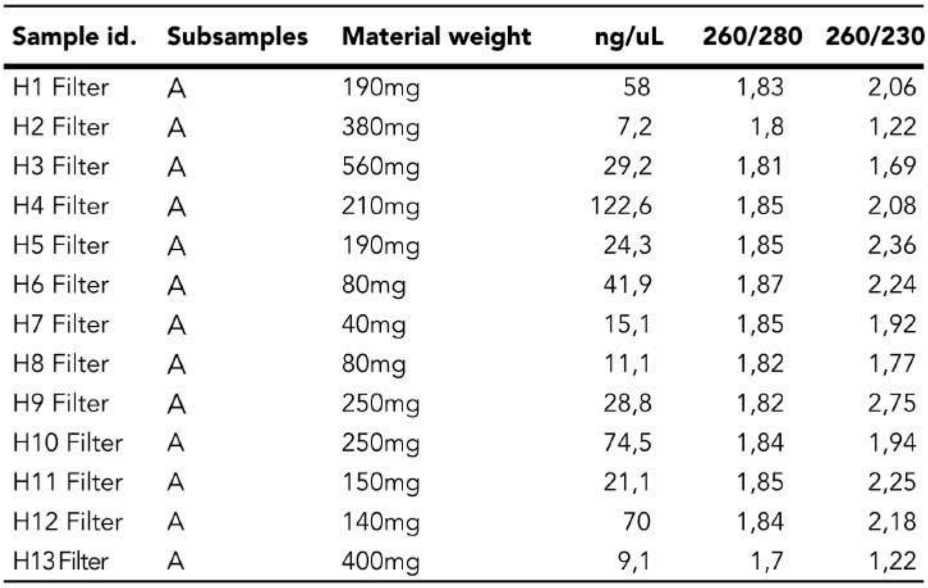

Sample id.	Subsamples	Material weight	ng/uL	260/280	260/230
H1 Filter	A	190mg	58	1,83	2,06
H2 Filter	A	380mg	7,2	1,8	1,22
H3 Filter	A	560mg	29,2	1,81	1,69
H4 Filter	A	210mg	122,6	1,85	2,08
H5 Filter	A	190mg	24,3	1,85	2,36
H6 Filter	A	80mg	41,9	1,87	2,24
H7 Filter	A	40mg	15,1	1,85	1,92
H8 Filter	A	80mg	11,1	1,82	1,77
H9 Filter	A	250mg	28,8	1,82	2,75
H10 Filter	A	250mg	74,5	1,84	1,94
H11 Filter	A	150mg	21,1	1,85	2,25
H12 Filter	A	140mg	70	1,84	2,18
H13 Filter	A	400mg	9,1	1,7	1,22

Small subunit rRNA amplicon sequencing

The V4 region of the bacterial 16S rRNA gene was amplified with 515F (5’-ACACTCTTTCCCTACACGACGCTCTTCCGATCTGTGYCAGCMGCCGCGGTAA-3’) and 806R (5’-GACTGGAGTTCAGACGTGTGCTCTTCCGATCTGGACTACNVGGGTWTCTAAT-3’) primers with Illumina adapters using Phire Green Hot Start II PCR Master Mix (ThermoScientific, article no F126S), and 1 µl of DNA, according to the user manual. The polymerase chain reaction (PCR) conditions were as follows: 98°C for 30 s, followed by 35 cycles of 98°C for 5 s, 50°C for 5 s and 72°C for 5 s, then 72°C for 1 min, and finally 10°C. The V4 region of the eukaryotic 18S rRNA gene was amplified with 3NDF (5’-ACACTCTTTCCCTACACGACGCTCTTCCGATCTGGCAAGTCTGGTGCCAG-3’) and 806R (5’GACTGGAGTTCAGACGTGTGCTCTTCCGATCTACGGTATCTRATCRTCTTCG-3’) primers with Illumina adapters using Phire Green Hot Start II PCR Master Mix (ThermoScientific, article no F126S), and 1 µl of DNA, according to the user manual. PCR conditions were as follows: 98°C for 30 s, followed by 35 cycles of 98°C for 5 s, 59°C for 5 s and 72°C for 5 s, then 72°C for 1 min, and finally 10°C.

For both 16S and 18S rRNA V4 gene PCR, each sample was amplified in 15 µL technical triplicates. Technical triplicates were pooled together and analyzed by electrophoresis in a 1.5% agarose gel to ensure amplification. PCR products were purified using AMPure XP beads (Beckman Coulter, A63880) according to the manufacturer's instructions, DNA was eluted in 30 ul of 5 mM Tris, pH 8.5. Library preparation and sequencing with Illumina MiSeq paired-end (2 x 300 bp) were performed using Eurofins NGSelect Amplicon 2nd PCR service. Eurofins processed with quality control of raw data using Cutadapt v2.7 (Martin, 2011), and merged the paired-end reads using FLASH v2.2.00 (Magoč and Salzberg, 2011).

TAXONOMIC PROFILING, RELATIVE ABUNDANCE, AND DIVERSITY ASSESSMENT OF MICROBIAL COMMUNITIES

The bioinformatics analysis pipeline nfcore/ampliseq (Straub et al., 2020) was used for denoising and taxonomic assignment of amplicons and downstream analysis. Merged paired-end reads were processed with the pipeline allowing the following analyses: sequencing quality control (FastQC) (Babraham Bioinformatics), Amplicon Sequence Variants (ASVs) inference with DADA2 (Callahan et al., 2016), ribosomal RNA sequences prediction (Barrnap) (Seemann, 2024), taxonomical classification (DADA2) using Silva (Quast et al., 2013) (16S) or PR2 (Guillou et al., 2013) (18S), absolute and relative feature/taxa count tables and plots, alpha rarefaction curves plots, alpha (ASV count, Shannon index) and beta (Bray Curtis PcoA) diversity indices computation and plots (QIIME2) (Bolyen et al., 2019). Relative abundance bubble plots were made with R tidyverse library (Wickham et al., 2019). All configuration files and output files are available in the Figshare repository.

RESULTS

The following section summarizes chemical, mineralogical, morphological, and biochemical data obtained from the hull, beam and steel samples of the MS *Estonia*. Data show that the sample components can be traced back to three known sources identified as follows: (1) the siliciclastic sediment surrounding the shipwreck, (2) the steel hull and its corrosion, and (3) elements in the Baltic Sea water. The siliciclastic deposits are primarily composed of quartz and aluminosilicates. The steel hull-derived phases are rich in Fe- and Fe-S-containing components as well as Mn and possible trace elements found in the steel (e.g., Cr, Ni). The Baltic Sea water provides typical ions (e.g., Ca^{2+}, Mg^{2+}, Na^{+}, Cl^{-}, CO_3^{2-}, SO_4^{2-}), present in several of phases (Fig. 7).

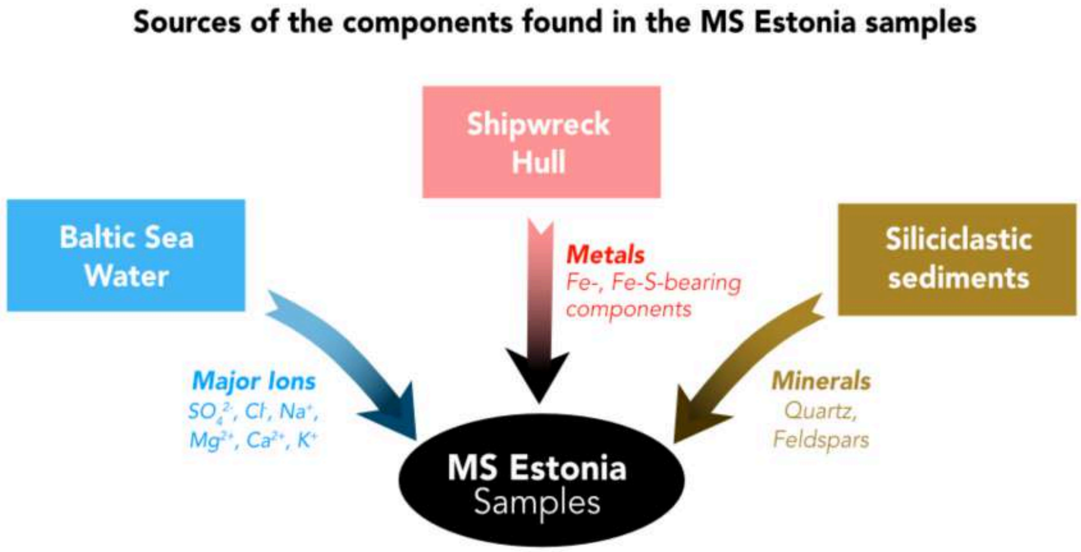

Sources of the components found in the MS Estonia samples

Figure 7. Sources of components found in the studied samples.

GEOCHEMISTRY

ELEMENTAL ANALYSES

Concentrations of elements (mg/kg, for elements with levels above 5 mg/kg) are given in Table 6a and 6b (note that Si and O are not included in the table). Element signatures characteristic of metals from the hull, from bottom sediments, as well as contribution from the seawater, are evident (c.f. Fig. 7):

- Elements extracted from samples H4, H5, H6, H7, H12, as well as H8 and H9 contain ca 30-45 g/kg Al, ca 10-12 g/kg Mg, ca 15-20 g/kg K, and also significant but low levels of Ba, Sr, Rb, Li.
- Metals extracted from the steel hull (sample S2B) consist predominantly of Fe (99%), Mn (0.5%) and trace levels of Ni, Co, Cu, and Cr. These metals are also found in considerable amounts in samples S3B and H13.
- Contributions from seawater salts: Precipitate levels of K, Na, Mg, Ca, and Ba may be correlated with the levels in the seawater (SWF), especially for samples with low Al-levels, possibly for sample H2 and, and to some extent, sample H13.
- Comparison with data from SEM-EDS spectra (see below) would give information on the levels of silicates in the samples (H-series) indicating sediment origin.

An extended analysis of data and assessments are given under 'Summary of data and interpretation'

Table 6A. Concentrations (mg/kg) for elements with levels above 5 mg/kg (Si and O not included) in: (1) samples collected from the cut-out metal piece from the hull (ES-23-S2B, S1B and S3B), (2) precipitates from the surface of the beam resting on the sea floor (ES-23-H8 and H9), and (3) water sampled close to the sea floor (SFW) with metal concentrations above 2 µg/L.

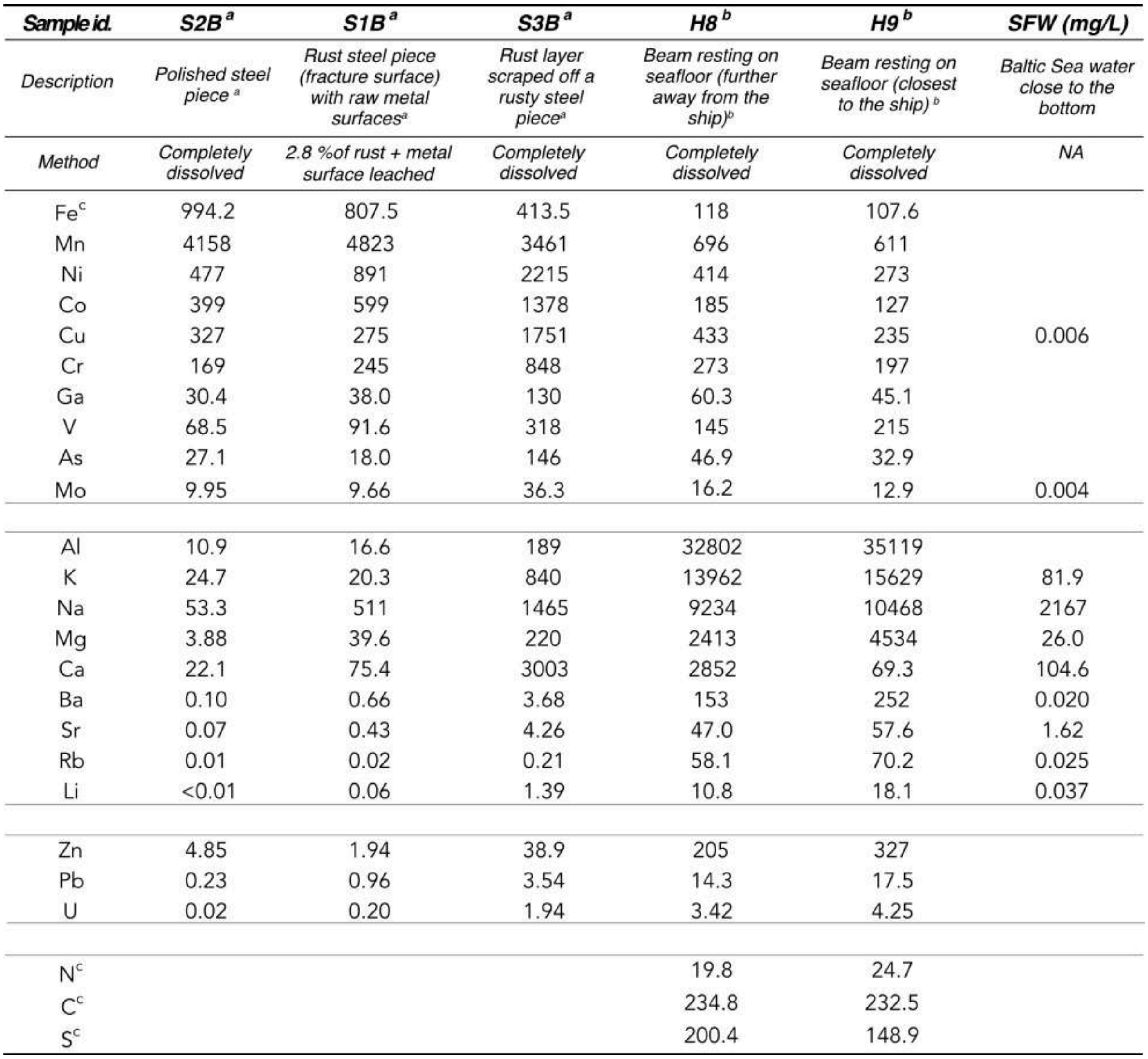

Sample id.	S2B [a]	S1B [a]	S3B [a]	H8 [b]	H9 [b]	SFW (mg/L)
Description	Polished steel piece [a]	Rust steel piece (fracture surface) with raw metal surfaces[a]	Rust layer scraped off a rusty steel piece[a]	Beam resting on seafloor (further away from the ship)[b]	Beam resting on seafloor (closest to the ship) [b]	Baltic Sea water close to the bottom
Method	Completely dissolved	2.8 %of rust + metal surface leached	Completely dissolved	Completely dissolved	Completely dissolved	NA
Fe[c]	994.2	807.5	413.5	118	107.6	
Mn	4158	4823	3461	696	611	
Ni	477	891	2215	414	273	
Co	399	599	1378	185	127	
Cu	327	275	1751	433	235	0.006
Cr	169	245	848	273	197	
Ga	30.4	38.0	130	60.3	45.1	
V	68.5	91.6	318	145	215	
As	27.1	18.0	146	46.9	32.9	
Mo	9.95	9.66	36.3	16.2	12.9	0.004
Al	10.9	16.6	189	32802	35119	
K	24.7	20.3	840	13962	15629	81.9
Na	53.3	511	1465	9234	10468	2167
Mg	3.88	39.6	220	2413	4534	26.0
Ca	22.1	75.4	3003	2852	69.3	104.6
Ba	0.10	0.66	3.68	153	252	0.020
Sr	0.07	0.43	4.26	47.0	57.6	1.62
Rb	0.01	0.02	0.21	58.1	70.2	0.025
Li	<0.01	0.06	1.39	10.8	18.1	0.037
Zn	4.85	1.94	38.9	205	327	
Pb	0.23	0.96	3.54	14.3	17.5	
U	0.02	0.20	1.94	3.42	4.25	
N[c]				19.8	24.7	
C[c]				234.8	232.5	
S[c]				200.4	148.9	

[a]*See Fig.6* [b]*See Fig.3* [c]*g/kg*

Table 6B. Concentrations (mg/kg) for elements with levels above 5 mg/kg (Si and O not included) in precipitates collected from the hull outer surface (ES-23-H-series except H8, H9) see Table 2.

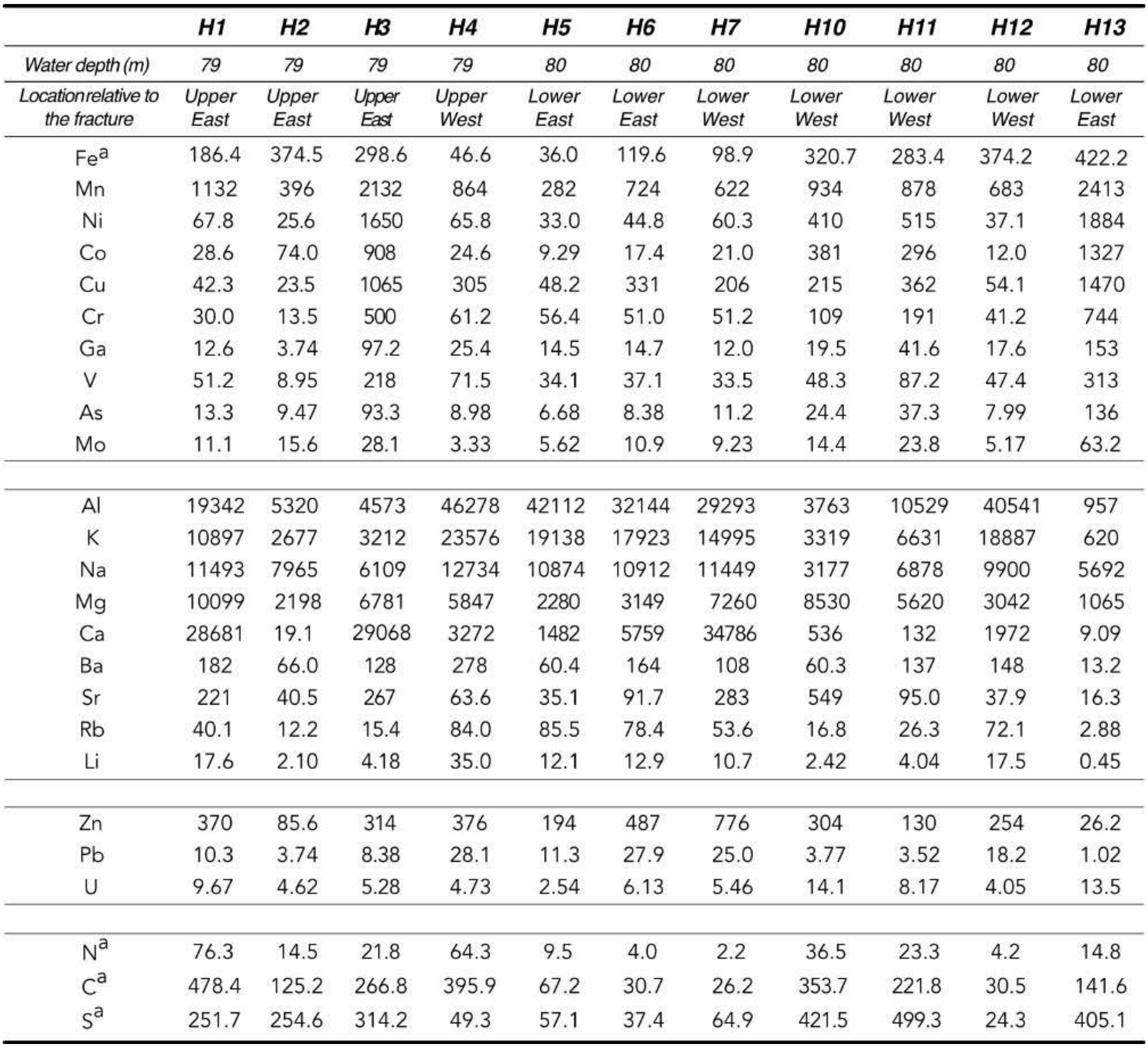

	H1	*H2*	*H3*	*H4*	*H5*	*H6*	*H7*	*H10*	*H11*	*H12*	*H13*
Water depth (m)	*79*	*79*	*79*	*79*	*80*	*80*	*80*	*80*	*80*	*80*	*80*
Location relative to the fracture	*Upper East*	*Upper East*	*Upper East*	*Upper West*	*Lower East*	*Lower East*	*Lower West*	*Lower West*	*Lower West*	*Lower West*	*Lower East*
Fe[a]	186.4	374.5	298.6	46.6	36.0	119.6	98.9	320.7	283.4	374.2	422.2
Mn	1132	396	2132	864	282	724	622	934	878	683	2413
Ni	67.8	25.6	1650	65.8	33.0	44.8	60.3	410	515	37.1	1884
Co	28.6	74.0	908	24.6	9.29	17.4	21.0	381	296	12.0	1327
Cu	42.3	23.5	1065	305	48.2	331	206	215	362	54.1	1470
Cr	30.0	13.5	500	61.2	56.4	51.0	51.2	109	191	41.2	744
Ga	12.6	3.74	97.2	25.4	14.5	14.7	12.0	19.5	41.6	17.6	153
V	51.2	8.95	218	71.5	34.1	37.1	33.5	48.3	87.2	47.4	313
As	13.3	9.47	93.3	8.98	6.68	8.38	11.2	24.4	37.3	7.99	136
Mo	11.1	15.6	28.1	3.33	5.62	10.9	9.23	14.4	23.8	5.17	63.2
Al	19342	5320	4573	46278	42112	32144	29293	3763	10529	40541	957
K	10897	2677	3212	23576	19138	17923	14995	3319	6631	18887	620
Na	11493	7965	6109	12734	10874	10912	11449	3177	6878	9900	5692
Mg	10099	2198	6781	5847	2280	3149	7260	8530	5620	3042	1065
Ca	28681	19.1	29068	3272	1482	5759	34786	536	132	1972	9.09
Ba	182	66.0	128	278	60.4	164	108	60.3	137	148	13.2
Sr	221	40.5	267	63.6	35.1	91.7	283	549	95.0	37.9	16.3
Rb	40.1	12.2	15.4	84.0	85.5	78.4	53.6	16.8	26.3	72.1	2.88
Li	17.6	2.10	4.18	35.0	12.1	12.9	10.7	2.42	4.04	17.5	0.45
Zn	370	85.6	314	376	194	487	776	304	130	254	26.2
Pb	10.3	3.74	8.38	28.1	11.3	27.9	25.0	3.77	3.52	18.2	1.02
U	9.67	4.62	5.28	4.73	2.54	6.13	5.46	14.1	8.17	4.05	13.5
N[a]	76.3	14.5	21.8	64.3	9.5	4.0	2.2	36.5	23.3	4.2	14.8
C[a]	478.4	125.2	266.8	395.9	67.2	30.7	26.2	353.7	221.8	30.5	141.6
S[a]	251.7	254.6	314.2	49.3	57.1	37.4	64.9	421.5	499.3	24.3	405.1

[a] *g/kg*

PHASE ANALYSIS AND MICROSCOPY

This section presents the key mineralogical and morphological features observed for each sample. The samples are presented in groups as a function of their main diagnostic signature:

> **Group 1** – Reference samples of (1) 'pristine' steel from the cut-out steel plate (Sample S2B), (2) non-fractured hull surface deposit (sample ES-23-H12) collected away from the damaged steel, likely to reflect the condition of the intact hull areas.
>
> **Group 2** – Hull deposit samples with a clastic sediment signature: Samples collected from the hull surface close to the fracture, largely composed by quartz and aluminosilicates (samples ES-23-H4, -H5, -H6, -H7).
>
> **Group 3** – Hull deposit samples with a metal signature. Samples collected from the hull surface close to the fracture, largely composed of iron-oxides, -hydroxides and/or -sulfides, and to a minor extent sediment (samples ES-23-H1, -H2, -H3, -H10, -H11, -H13). The cut-out steel plate subsamples S1B (rusty steel from the fracture surface) and S3B (scraped rust from the steel) are also included in this group (Table 6a). Sample S1B represents an early stage of exposed steel corrosion at the fracture surface, while sample S3B consists of rust scraped off the cut-out steel plate.
>
> **Group 4** – Beam deposit samples. Samples collected from the surface of the beam resting on the seafloor (Fig. 3), showing a mixed clastic-metal signature (samples ES-23-H8, -H9).

Two main approaches were used: powder X-ray diffraction for sample mineralogy, and SEM-EDS for micrometer-scale correlating morphology and chemistry (a sample of the cut-out steel plate was also analyzed for reference purposes). Each sample is described following the same sequence of analyses, applying the following analytical steps:

1. **XRD spectrum and accompanying diagnostic peak list:**
   Each sample description starts with a figure showing the XRD spectrum and a table listing all diagnostic peaks and their potential mineralogical matches. The XRD bulk analysis identifies crystalline phases that make up a minimum of 5% of the sample. This method will not detect phases below this detection limit nor any non-crystalline (amorphous) phases.

2. **SEM images:**
   The XRD data are followed by SEM images documenting key morphological features of the sample. All images were taken using a backscattered electron (BSE) detector. The number of backscattering electrons increases with the atomic number of an element. This allows for differentiation between phases and constituents based on contrast variations (heavier elements appear brighter). In addition, EDS analyses were conducted to obtain element data for certain morphological features. A circled number and an arrow mark the position of the conducted chemical EDS analysis.

3. **EDS analyses:**
   - EDS spectrum analyses provide chemical composition on a point or limited surface area within a sample. A circled number in a SEM image indicates the location of a point analysis. The corresponding number is found in the associated element table.
   - EDS element data are presented in atomic percent (at%) that describes the proportion of each element based on the number of atoms, taking into account the differences in atomic mass. This representation provides information about the stoichiometry of a mineralogical phase.
   - EDS was also used to map the chemical composition of specific areas in the samples. EDS mapping creates a detailed, color-coded map that visualizes the distribution and concentration of elements within the analyzed area. The SEM images representing the maps are identified on the SEM plate and in the legend.
   - EDS analyses (both spectrum and map) confirmed the presence of some of the minerals determined by XRD but also revealed novel phases that the XRD could not identify (EDS does not directly indicate mineralogy, but mineralogy can be interpreted from the morphology and chemical composition).

GROUP 1 – REFERENCE SAMPLES

Reference steel

Diamond polished pieces of the cut-out steel plate, sample ES-23-SA (the A-series of steel plate samples, Fig.6). All investigated samples of the steel have a similar composition and microstructure. The polished steel has a crystalline mosaic microstructure, consisting of crystals with varying orientations (seen as light and dark areas within the steel). EDS analyses show that metallic Fe is the dominant element, with both light and dark crystals exhibiting similar spectra (Phase 1 and 2). Black inclusions of varying sizes and shapes are randomly distributed within the steel (Fig. 8B, C, D). Spherical to sub-spherical inclusions range from sub-micron sized to approximately 6 μm in diameter, while the angular inclusions typically are larger. EDS analyses show that these regions mainly consist of Mn-S, presumably sulfides (Fig.8, Phases 3, 5). Since these regions are small, the surrounding matrix of metallic Fe contributes to the EDS signal and should be considered a source of interference. One of the angular inclusions shows compositional zoning, with an outside rim of comparable composition to the globular inclusions and a core containing Si in addition to Mn and S (Fig 8, Phase 5 and 4, respectively). Another observed angular inclusion (Fig. 8D) exhibited a color and composition similar to the core of the angular particle shown in Fig. 8C, but with the addition of Al (Fig 8, Phase 6).

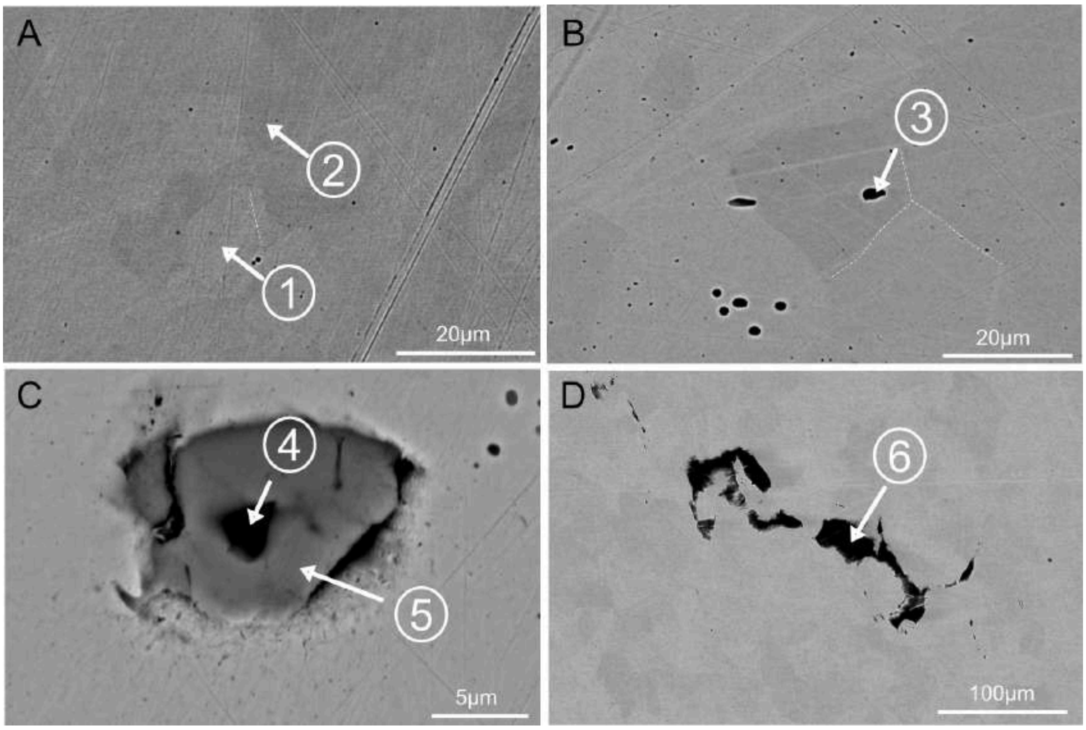

Phases (at%)	Fe	O	S	Mn	Si	Al
1	100					
2	100					
3	47		25	24		
4	4	39	15	21	15	
5	4		48	48		
6	9	51		10	17	10

Figure 8. SEM photomicrographs of diamond polished surfaces of the cut-out steel plate. Numbers indicate the location of the associated EDS spectra shown at the bottom of this figure. **(A)** Subsample 2A (see Fig. 2) showing the crystalline microstructure (mosaic) of the steel composed of individual crystals with different orientations, seen as light and dark mosaic crystals. **(B)** Subsample 4A (see Fig. 2) showing black globular inclusions of Mn sulfide within the crystalline mosaic microstructure of the steel. The observed sulfur-containing regions vary in size from sub-micron to approximately 6 μm in diameter, and are randomly distributed within the investigated steel plate **(C)** Subsample 2A (see Fig. 2) showing an angular, compositionally zoned, dark inclusion within the steel. The core of the inclusion contains Mn, S, and Fe as well as Si and O, while the rim only contains Mn, S, and Fe. **(D)** Subsample 2A (see Fig. 2) showing another example of an angular inclusion.

Non-fractured hull surface deposit

Sample ES-23-H12

Sample H12 consists of hull deposits collected away from the damaged steel, likely reflecting the condition of intact hull areas. Two main phases - were identified from the XRD pattern (Fig. 9): (1) quartz (IDD reference 00-033-1161), and (2) anorthite, a calcium-rich feldspar ($Ca_{0.89}$, $Na_{0.11}$)($Al_{1.89}Si_{0.11}$)Si_2O_8 (IDD reference 01-074-2539). Electron microscopy confirmed that the sample primarily consists of siliciclastic sediments (Fig. 10 and 11) with diatoms present within the siliciclastic framework (Fig. 10B). Sparsely distributed iron sulfides (FeS_2) were also detected, mainly disintegrated framboidal pyrite grains (Fig. 10C, D).

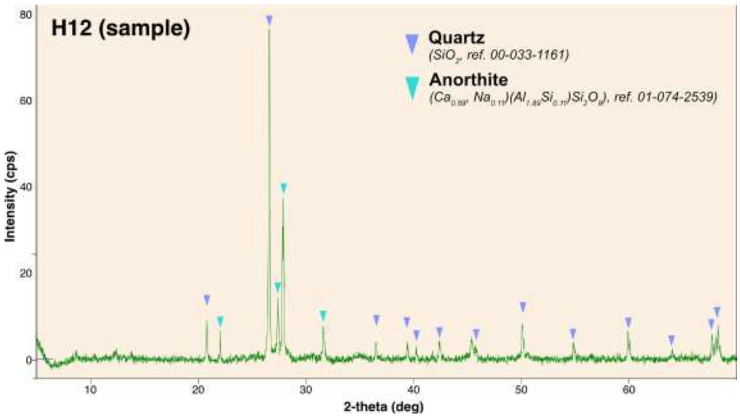

Pos.[°2θ]	Height (cts)	Rel. Int. [%]	Matched by	ICDD Ref
20.8561	335.34	12.87	Quartz	00-033-1161
22.0841	204.23	7.84	Anorthite	01-074-2539
26.6469	2604.86	100.00	Quartz	00-033-1161
27.4422	481.09	18.47	Anorthite	01-074-2539
27.9202	1137.97	43.69	Anorthite	01-074-2539
31.6668	263.82	10.13	Anorthite	01-074-2539
36.5368	162.83	6.25	Quartz	00-033-1161
39.4534	140.17	5.38	Quartz	00-033-1161
40.2681	108.91	4.18	Quartz	00-033-1161
42.4263	158.88	6.10	Quartz	00-033-1161
45.4050	178.49	6.85	Quartz	00-033-1161
50.1234	307.30	11.80	Quartz	00-033-1161
54.8646	133.99	5.14	Quartz	00-033-1161
59.9296	252.99	9.71	Quartz	00-033-1161
64.0274	70.13	2.69	Quartz	00-033-1161
67.7224	197.23	7.57	Quartz	00-033-1161
68.3020	256.06	9.83	Quartz	00-033-1161

Figure 9. X-ray diffractograms of Sample ES-23-H12 with diagnostic peaks and matching references in the ICDD PDF-4+ database. Two main phases were identified from the XRD pattern: (1) quartz (IDD reference 00-033-1161), and (2) anorthite ($Ca_{0.89}$, $Na_{0.11}$)($Al_{1.89}Si_{0.11}$)Si_2O_8 (IDD reference 01-074-2539).

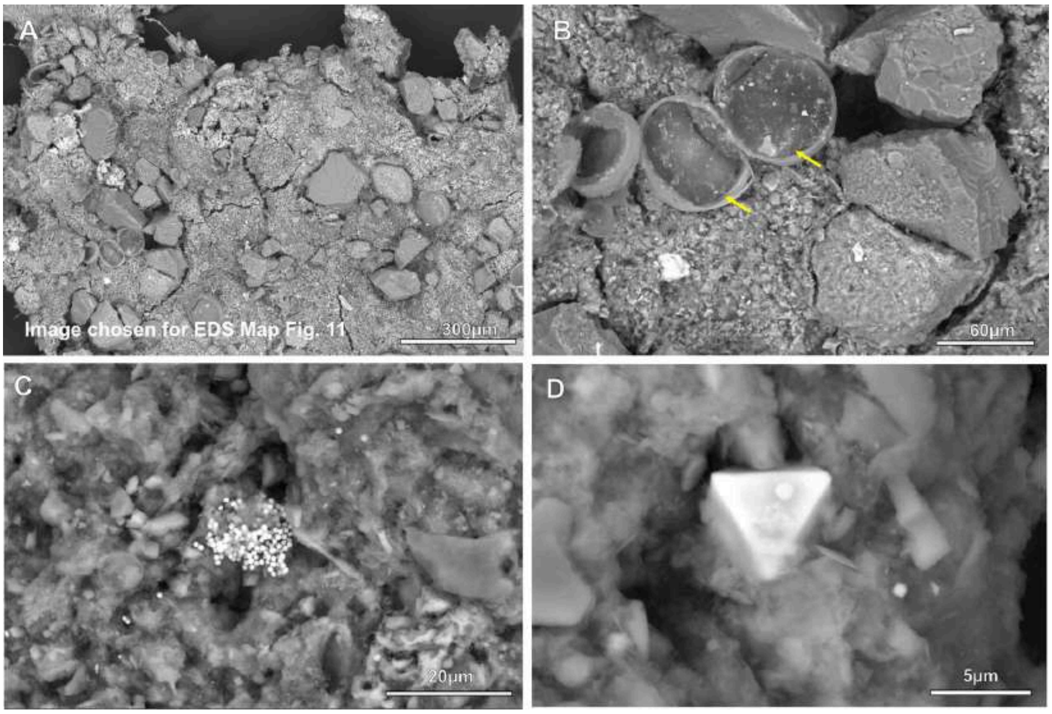

Figure 10. SEM photomicrographs of sample ES-23-H12. **(A)** Overview of the sample showing primarily siliciclastic particles. This image was selected for EDS mapping, see Fig. 11 **(B)** Diatoms embedded in the siliciclastic matrix. **(C)** Broken framboidal pyrite crystals. **(D)** Close-up of a pyrite crystal.

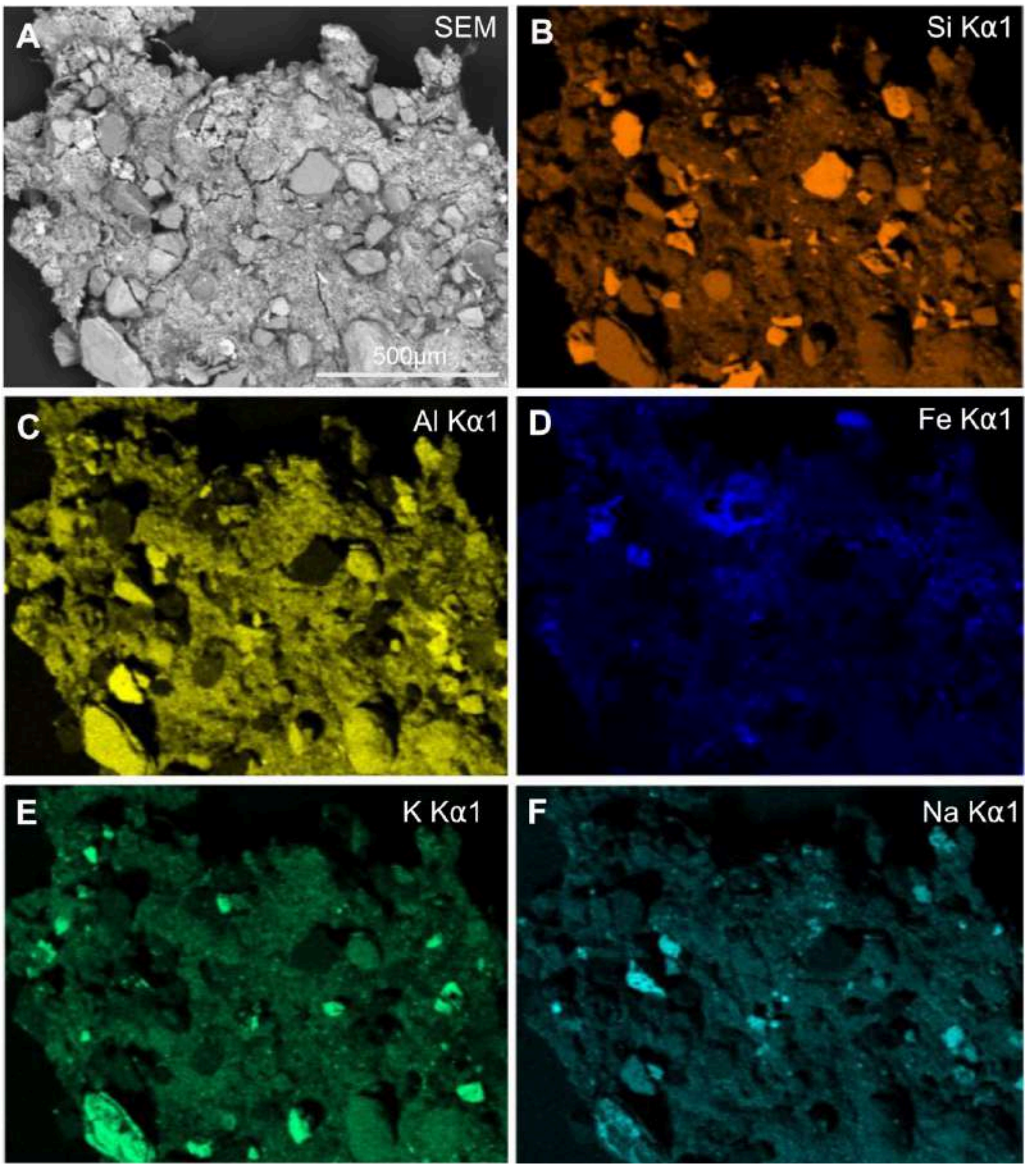

Figure 11. Elemental mapping of sample ES-23-H12 showing the chemical composition of a typical area in the sample. (B),(C),(E), and (F) shows evidence of Si, Al, K and Na, typical elements for quartz and various types of feldspars. (D) Zone enriched in iron where pyrite is present.

GROUP 2 – HULL DEPOSIT SAMPLES WITH A CLASTIC SEDIMENT SIGNATURE

Sample ES-23-H4

Sample ES-23-H4 was collected in the upper west section of the sampling zone. Three main phases were identified from the XRD pattern (Fig. 12): (1) quartz IDD reference 00-033-1161), (2) feldspars (calcium aluminum silicate phase, IDD reference 00-052-1344), and (3) Mg-bearing calcite (Fig. 12, IDD reference 00-043-0697). SEM-EDS analyses confirmed that the sample primarily comprises clastic sediment and that it also contains minor amounts of iron-bearing minerals that could not be detected using XRD. Elemental mapping of a typical sample area is shown in Figure 14. Particles range from mud to silt-sized clastic sediment, including quartz (Fig.13B; Phase 1), aluminosilicates, and a small amount of titanium oxides (Fig. 13B; Phase 2). Diatoms, a group of single-celled algae enclosed in siliceous cell walls, are common in between the siliciclastic particles.

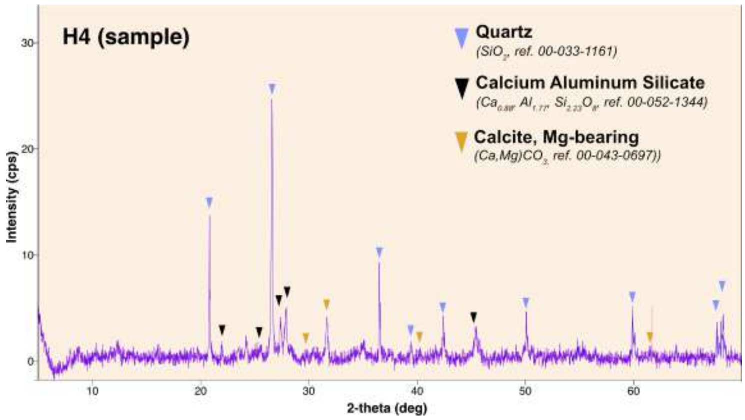

Pos.[°2θ]	Height (cts)	Rel. Int. [%]	Matched by	ICDD Ref
20.8760	451.29	42.05	Quartz	00-033-1161
22.0285	62.79	5.85	Calcium Aluminum Silicate	00-052-1344
23.5487	45.00	4.19	Mg-Bearing Calcite	00-013-0092
25.5768	54.33	5.06	Calcium Aluminum Silicate	00-052-1344
26.6468	1073.18	100.00	Quartz	00-033-1161
27.4250	165.38	15.41	Calcium Aluminum Silicate	00-052-1344
27.9700	211.74	19.73	Calcium Aluminum Silicate	00-052-1344
31.6874	181.63	16.92	Mg-Bearing Calcite	00-013-0092
36.5570	316.25	29.47	Quartz	*00-033-1161*
39.4523	79.70	7.43	Quartz	*00-033-1161*
42.4397	157.66	14.69	Quartz	*00-033-1161*
45.4511	146.15	13.62	Calcium Aluminum Silicate	00-052-1344
50.1244	185.69	17.30	Quartz	*00-033-1161*
59.9471	196.20	18.28	Quartz	*00-033-1161*
67.7328	162.98	15.19	Quartz	*00-033-1161*
68.2518	135.96	12.67	Quartz	*00-033-1161*

Figure 12. X-ray diffractogram of sample ES-23-H4 with diagnostic peaks and matching references in the ICDD PDF-4+ database. The sample is dominated by siliciclastic sediments and minor amounts of Mg-bearing carbonate.

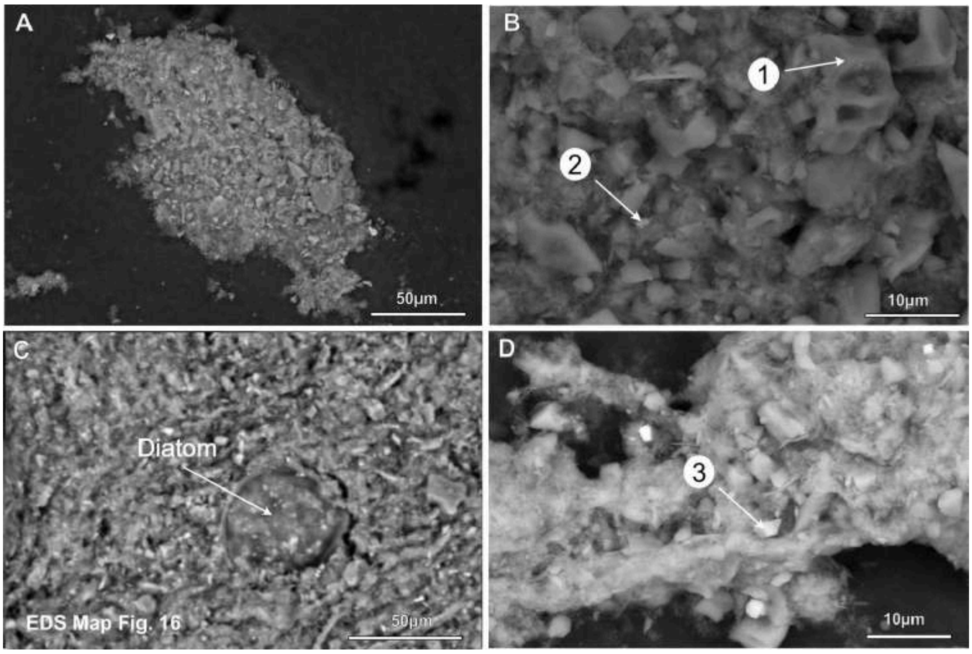

Phases (at%)	O	Fe	Si	Ca	K	Al	Ti
1	66		32				
2	61	1	17	4	2	7	4
3	60	3	16	6		11	

Figure 13. SEM photomicrographs of sample ES-23-H4. Numbers indicate the location of the associated EDS spectra, which are shown at the bottom of this figure. **(A)** Aggregates that consist of a mixture of clastic sediment. **(B)** Close-up of (A) showing quartz (Phase 1) and aluminosilicates possible mixed with TiO_2 (Phase 2). **(C)** Diatoms embedded in a siliciclastic matrix (Fig. 14; element mapping). **(D)** Aluminosilicate (Phase 3) within an aggregate composed of a mixture of clastic sediment.

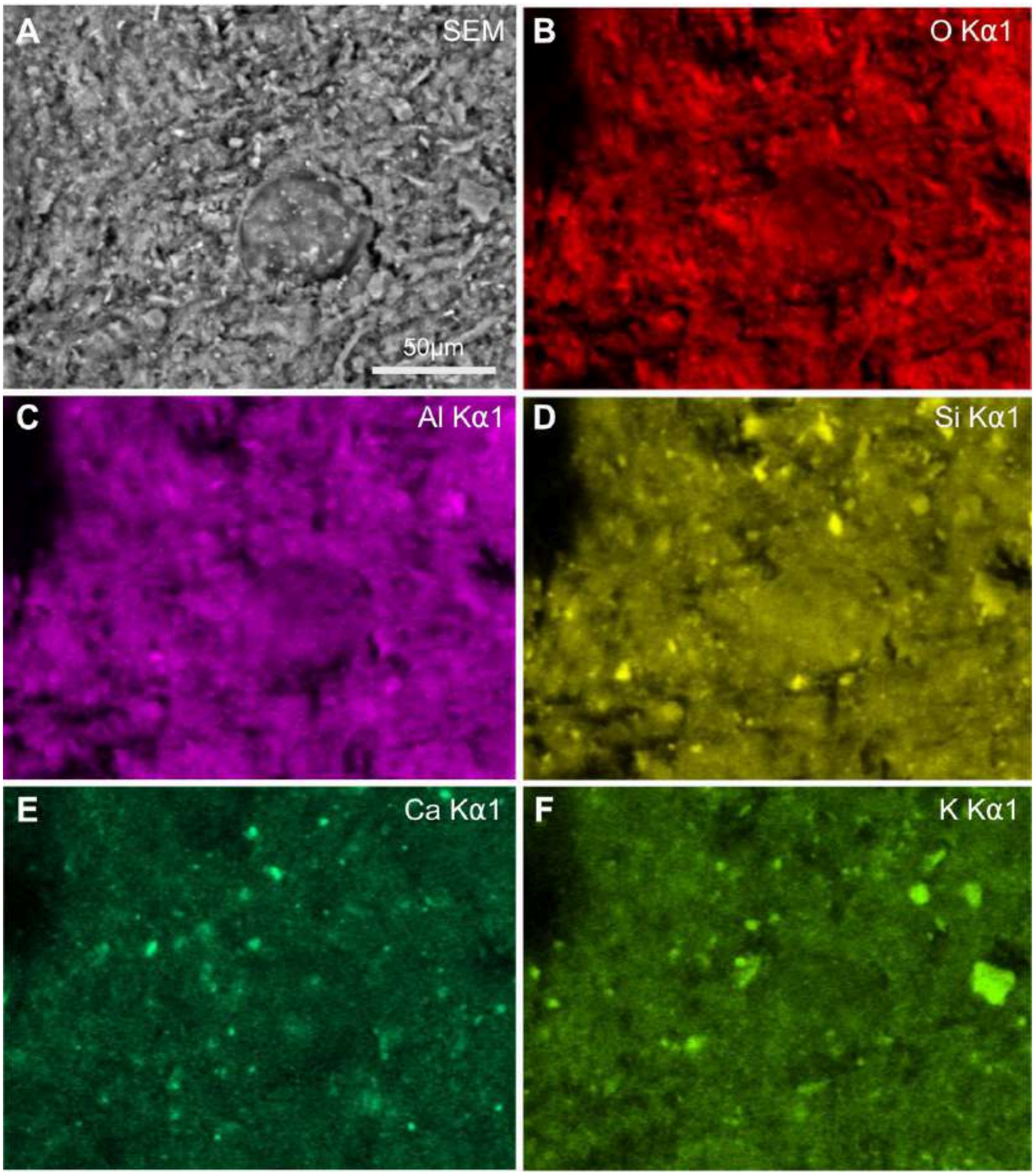

Figure. 14. EDS mapping of ES-23-H4 showing that the sample is primarily composed of silicates.

Sample ES-23-H5

Sample ES-23-H5 was collected in the lower-east area of the sampling zone. Three main phases were identified from the XRD pattern (Fig. 15): (1) quartz (IDD reference 00-033-1161), (2) feldspars (as the calcium aluminum silicate phase, IDD reference 00-052-1344), and (3) Mg-bearing calcite (IDD reference 00-043-0697). SEM-EDS analyses confirmed the presence of silicate minerals and also detected various types of diatoms, collectively comprising the bulk of the sample (Fig: 16E and EDS map in Figure 17). The sample also contains a fair number of iron-rich particles with smooth surfaces, angular edges, and breakages (Fig. 16A, Fig. 19) as well as framboidal pyrite (Fig. 16C,D). Framboidal morphology refers to the arrangement of pyrite crystals, densely packed into spherical aggregates (Fig. 16C). The framboids in sample ES-23-H5 are frequently fragmented and the constituent pyrite granules are scattered throughout the sample (Fig. 16D). EDS mapping demonstrates the Fe-S composition.

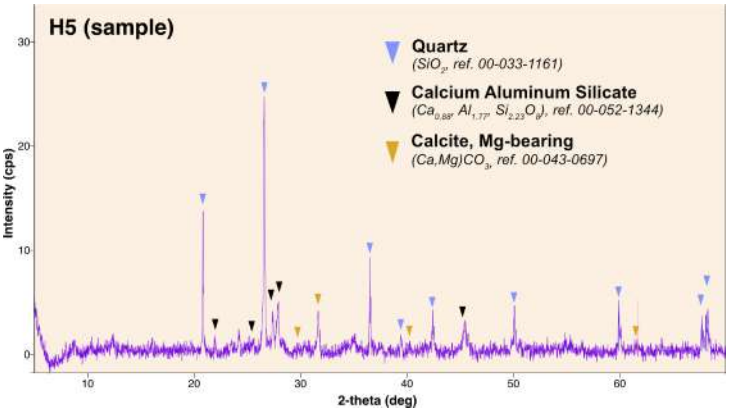

Pos.[°2θ]	Height (cts)	Rel. Int. [%]	Matched by	ICDD Ref
20.8071	647.87	18.79	Quartz	00-033-1161
21.9978	132.96	3.86	Calcium Aluminum Silicate	00-052-1344
25.5106	106.27	3.08	Calcium Aluminum Silicate	*00-033-1161*
26.6153	3448.50	100.00	Quartz	*00-033-1161*
27.0697	224.72	6.52	Calcium Aluminum Silicate	00-052-1344
27.3739	362.23	10.50	Calcium Aluminum Silicate	00-052-1344
27.9913	691.79	20.06	Calcium Aluminum Silicate	00-052-1344
30.4874	185.22	5.37	Quartz	*00-033-1161*
31.7229	84.25	2.44	Mg-Bearing Calcite	*00-013-0092*
36.5256	244.86	7.10	Quartz	*00-033-1161*
39.4257	190.04	5.51	Quartz	*00-033-1161*
40.2847	161.16	4.67	Mg-Bearing Calcite	*00-013-0092*
42.4391	188.35	5.46	Quartz	*00-033-1161*
50.1299	609.42	17.67	Quartz	*00-033-1161*
59.9187	377.23	10.94	Quartz	*00-033-1161*
67.7116	323.43	9.38	Quartz	*00-033-1161*
68.2313	302.92	8.78	Quartz	*00-033-1161*

Figure 15: X-ray diffractogram of sample ES-23-H5 with diagnostic peaks and matching references in the ICDD PDF-4+ database. The sample mostly comprises quartz, some plagioclases (calcium aluminium silicate) and traces of carbonates. Despite a fair number of iron-rich particles in the sample, no iron phase was detected in the XRD pattern.

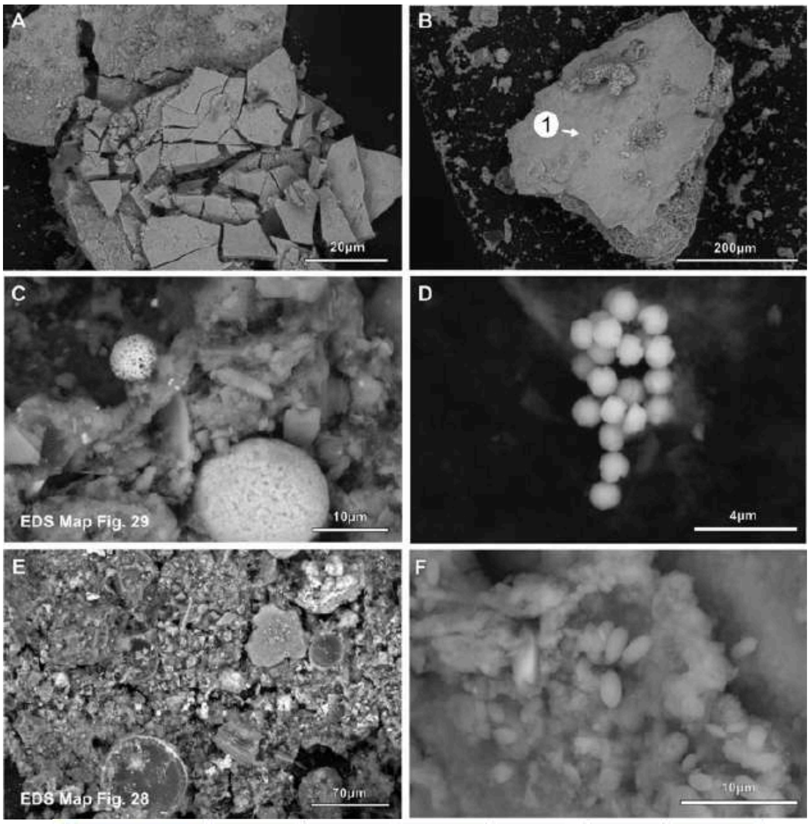

Phases (at%)	O	Fe	Na	Cl	Cr	S
1	48	25	11	7	4	2

Figure 16: SEM photomicrographs of sample ES-23-H5. **(A)** Particle of possibly altered steel. **(B)** Close-up of (A), with the location of the associated EDS spectrum shown at the bottom of this figure (Phase 1). Element data show that this is an iron-rich particle containing chromium and nickel, consistent with the composition of steel. The spectrum also showed siliciclastic material and halite (NaCl) in the background. **(C)** Framboidal pyrite and individual pyrite grains separated from the framboids (EDS mapping Fig. 21). **(D)** Dissociated pyrite particles. **(E)** Diatoms within siliciclastic sediment (EDS mapping Fig. 20). **(F)** Putative cells within siliciclastic sediment.

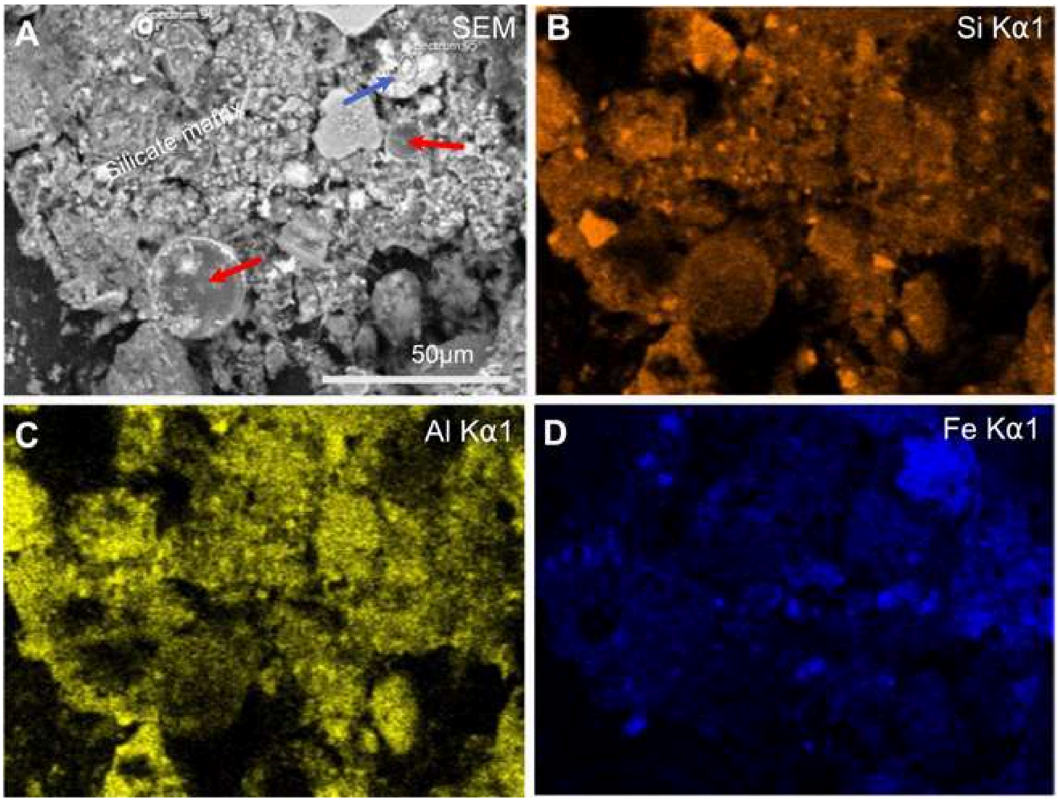

Figure 17: EDS mapping of sample ES-23-H5 showing a predominantly siliciclastic composition, with occasional diatoms and iron-rich particles.

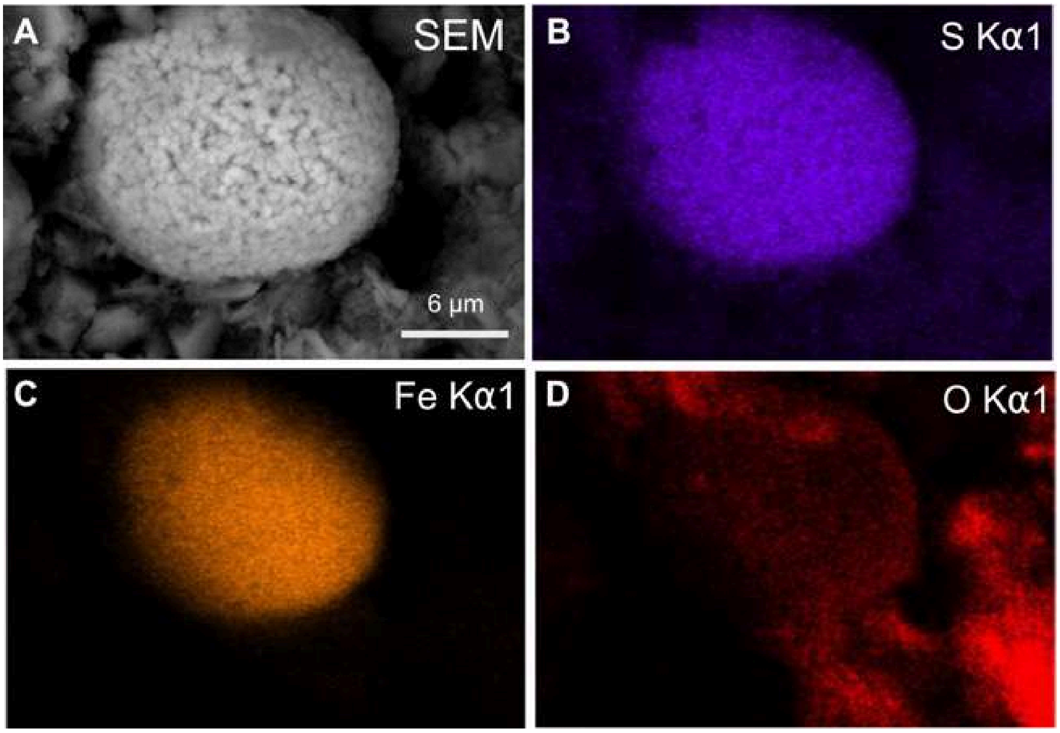

Figure 18: Mapping of framboidal pyrite (Fig. 16C) showing the presence of iron (Fe) and sulfur (S) and the absence of oxygen.

Sample ES-23-H6

Sample ES-23-H6 was collected from the lower-east region of the sampling zone (Fig. 2). This sample has a predominantly siliciclastic composition and also contains a significant amount of salt, mainly halite originating from the salt ocean water (IDD reference 00-005-0628). In addition to halite, three main phases were identified from the XRD pattern (Fig. 19): (1) quartz (IDD reference 00-033-1161), (2) feldspars (as the calcium aluminum silicate phase, IDD reference 00-052-1344) and (3) Mg-bearing calcite (IDD reference 00-043-0697). No iron phase was detected (Fig. 19), despite clearly present as encrusted filaments in the SEM-EDS analysis (Fig. 20, Phase 1). The filaments are randomly distributed throughout the siliciclastic sedimentary matrix.

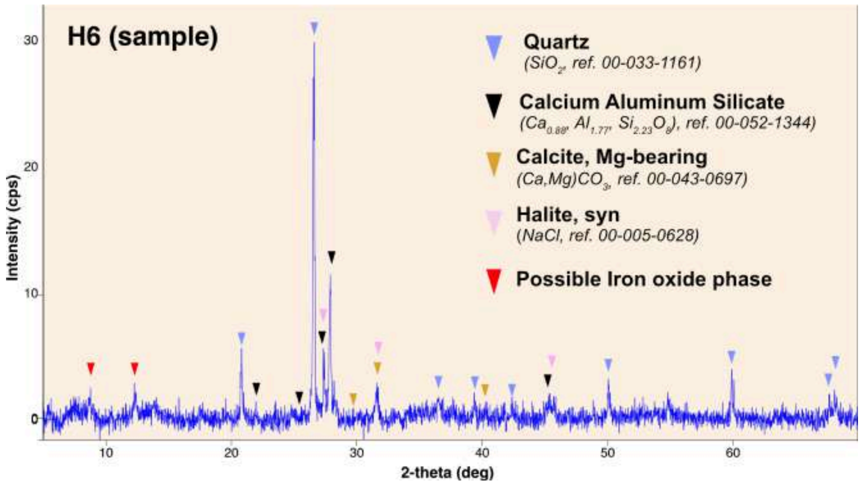

Pos.[°2θ]	Height (cts)	Rel. Int. [%]	Matched by	ICDD Ref
8.7313	72.32	6.97	Possible Iron Oxide	
12.3547	59.63	5.75	Possible Iron Oxide	
20.8237	179.46	17.30	Quartz	00-033-1161
26.6165	1037.07	100.00	Quartz	00-033-1161
27.4029	168.83	16.28	Calcium Aluminum Silicate Halite	00-052-1344 00-005-0628
27.9204	427.16	41.19	Calcium Aluminum Silicate	00-052-1344
31.6398	86.64	8.35	Mg-Bearing Calcite Halite	00-052-1344 00-005-0628
36.5098	59.91	5.78	Quartz	00-033-1161
39.4465	70.33	6.78	Quartz	00-033-1161
42.4491	41.44	4.00	Quartz	00-033-1161
45.5522	38.97	3.76	Quartz Halite	00-033-1161 00-005-0628
50.0872	108.55	10.47	Quartz	00-033-1161
59.9797	81.73	7.88	Quartz	00-033-1161
68.2286	40.58	3.91	Quartz	00-033-1161

Figure 19. X-ray diffractogram of sample ES-23-H6 with diagnostic peaks and matching references in the ICDD PDF-4+ database. The sample is dominated by siliciclastic sediments with traces of a Mg-bearing carbonate and an iron-bearing phase. Halite originating from the Baltic Sea water was also detected.

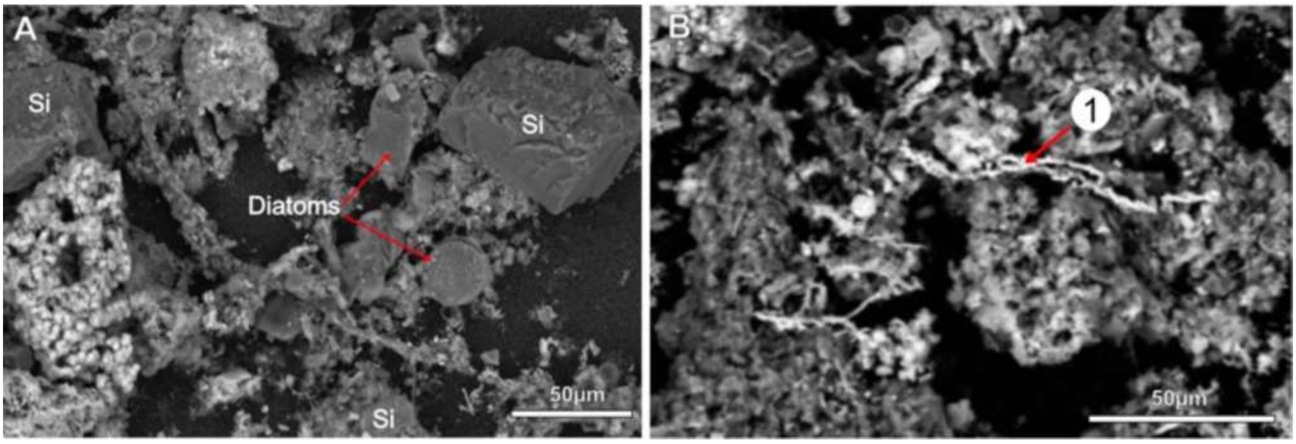

Figure 20. SEM photomicrographs of sample ES-23-H6. **(A)** Iron-encrusted filaments surrounded by siliciclastic particles (Si) and diatoms (red arrows). **(B)** Similar filamentous structures with the location of the EDS analysis (Phase 1).

Sample ES-23-H7

Sample ES-23-H7 was collected from the lower west region of the sampling zone. Four main phases were identified from the XRD pattern (Fig. 21): (1) quartz (IDD reference 00-033-1161), (2) feldspars (as the calcium aluminum silicate phase, IDD reference 00-052-1344), (3) Mg-bearing calcite (IDD reference 00-043-0697), and halite (IDD reference 00-005-0628). There was also an indication of an iron oxide phase, but the peak pattern did not allow identification. SEM analyses confirmed the presence of siliciclastic sediment (quartz and feldspars) and carbonate particles (Fig. 22B, D; Phase 2 and Phase 3). Occasional iron-encrusted filaments were also observed in between the sedimentary particles (Fig. 22F, Phase 4). These filaments were typically found in close proximity to diatoms (Fig. 22E). Stocky aggregates of calcium carbonate scales are abundant in the sample and EDS analyses indicate that they incorporate Mg and/or Fe (Fig. 22D, Phase 3). The sample also contains a few discrete baryte particles, a few µm in diameter (Fig. 22C, Phase 5) (baryte was below the detection limit for XRD). Occasional spherical particles of halite (Fig. 22A, Phase 1) were also observed within the sample.

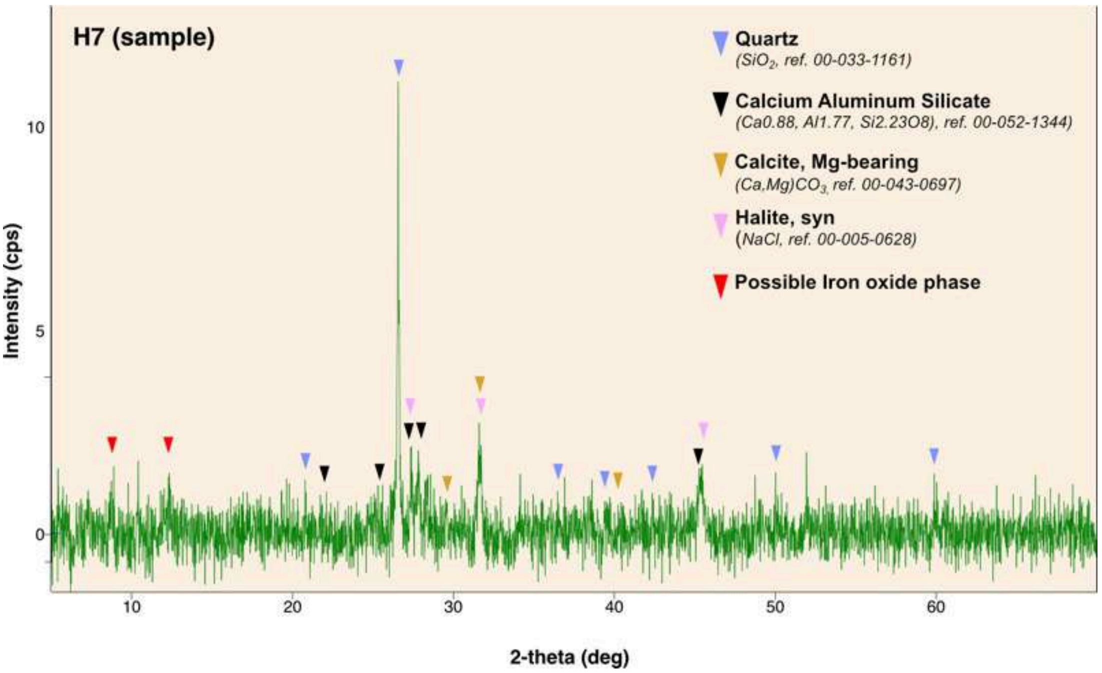

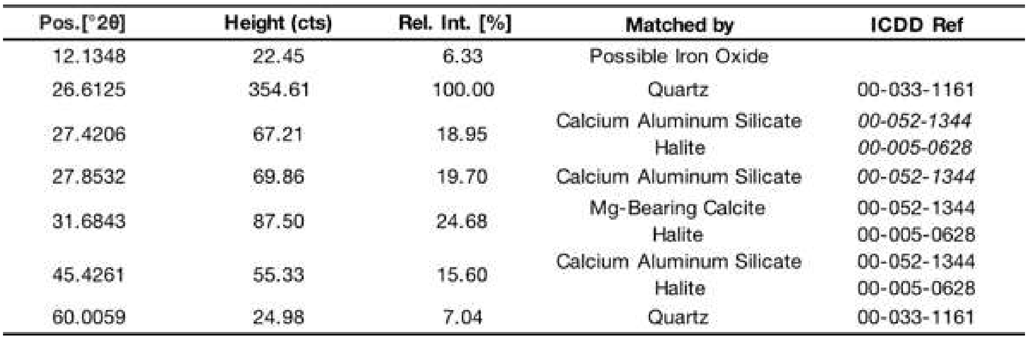

Pos.[°2θ]	Height (cts)	Rel. Int. [%]	Matched by	ICDD Ref
12.1348	22.45	6.33	Possible Iron Oxide	
26.6125	354.61	100.00	Quartz	00-033-1161
27.4206	67.21	18.95	Calcium Aluminum Silicate Halite	*00-052-1344* *00-005-0628*
27.8532	69.86	19.70	Calcium Aluminum Silicate	*00-052-1344*
31.6843	87.50	24.68	Mg-Bearing Calcite Halite	00-052-1344 00-005-0628
45.4261	55.33	15.60	Calcium Aluminum Silicate Halite	00-052-1344 00-005-0628
60.0059	24.98	7.04	Quartz	00-033-1161

Figure 21. X-ray diffractogram of sample ES-23-H7 with diagnostic peaks and matching references in the ICDD PDF-4+ database.

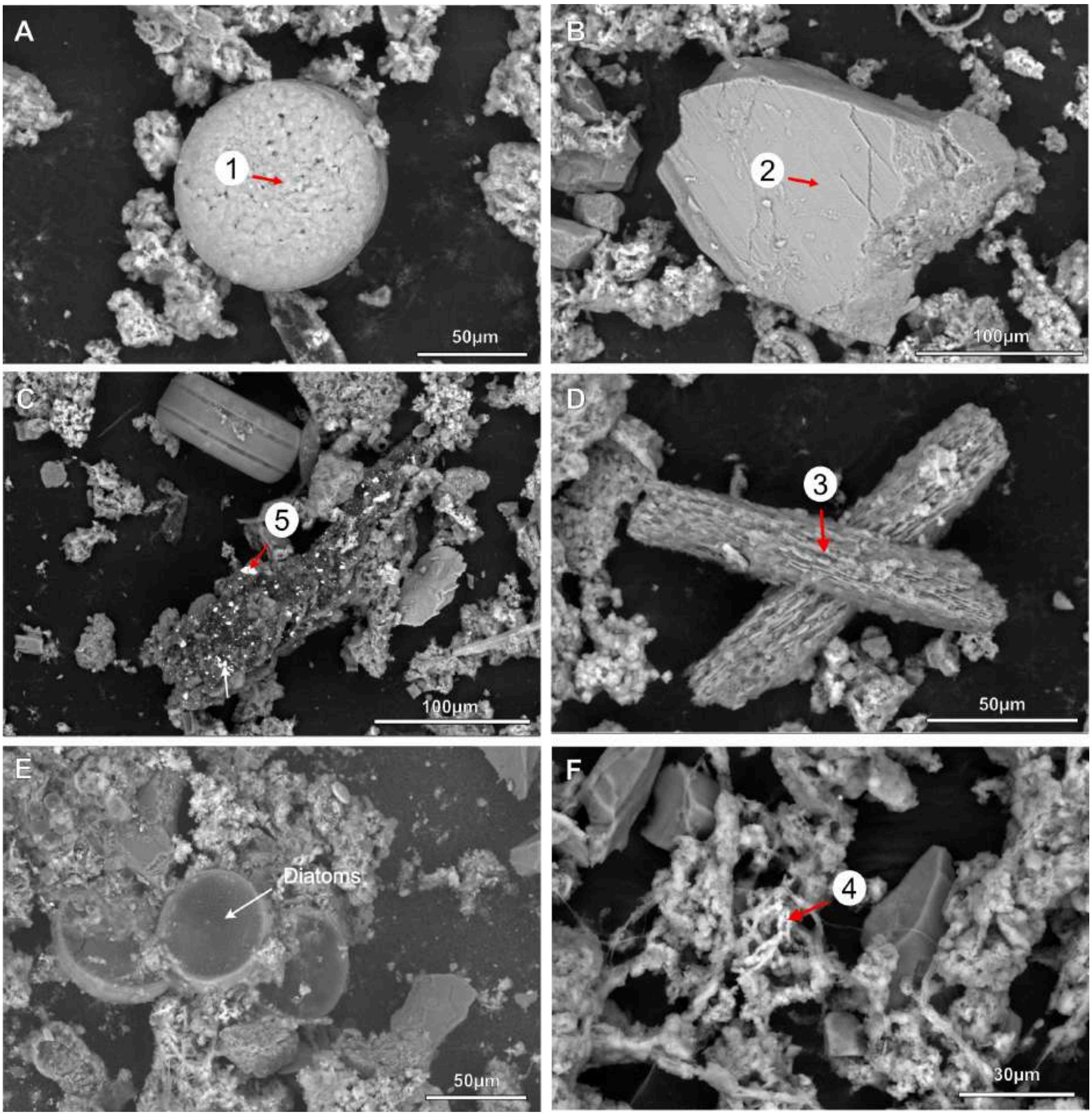

Phases (at%)	O	Fe	S	Si	Al	Ca	Mg	Na	Cl	Ba
1	62			1				16	21	
2	81	5		6	3	3	1	1		
3	85					12		1	1	
4	86	4	5	1				3	1	
5	89		5							5

Figure 22. SEM photomicrographs of sample ES-23-H7. Numbers indicate the location of the associated EDS spectra, which are shown at the bottom of this figure. **(A)** Spherule of salt (NaCl, halite) (Phase 1). **(B)** Ca-bearing aluminosilicate particle (plagioclase) (Phase 2) **(C)** Baryte particles (white) on the surface of an aggregate containing primarily siliciclastic sediment (Phase 5)**. (D)** Stocky aggregates of Mg-bearing calcium carbonate scales (Phase 3). **(E)** Sediment composed of diatoms, siliciclastic particles, and iron oxides. **(F)** Filaments encrusted by iron sulfur minerals with location of EDS analysis (Phase 4).

GROUP 3 – HULL DEPOSIT SAMPLES WITH A METAL SIGNATURE

Sample ES-23-H1

Sample ES-23-H1 was collected from the upper-east sampling zone, where the material deposited on the hull appeared disrupted (Fig. 2A,B). The sample did not yield an interpretable XRD pattern (Fig. 23). Morphology, chemistry, and to some extent, mineralogy were thus determined using SEM-EDS analyses (Fig. 24). The sample contains a substantial amount of calcium carbonates rich in iron and magnesium (Fig. 24A, B; Phase 2a and 2b). The majority of these crystals are porous with incomplete crystal faces (stepped and kinked phases; Fig. 24A red arrows; e.g., Van Driessche, 2007; Sancho Tomas, 2014). Rod-shaped iron sulfate microstructures are observed on the surfaces of these calcium carbonates (Fig. 24B) but also, in large part alone, forming networks (Fig. 24C, D; Phase 3). There are also groupings of similar rod-shaped microstructures, as seen in Figures 24 B,C, and D, but these are translucent and primarily composed of iron oxides, with only minor amounts of sulfur (Fig. 24E; Phase 4). Occasionally, angular baryte crystals (Fig. 24F; Phase 5) and prismatic gypsum crystals are observed. The sample also contains silicate minerals of varying composition but is typically rich in magnesium, iron, and calcium (Fig. 24A; Phase 1).

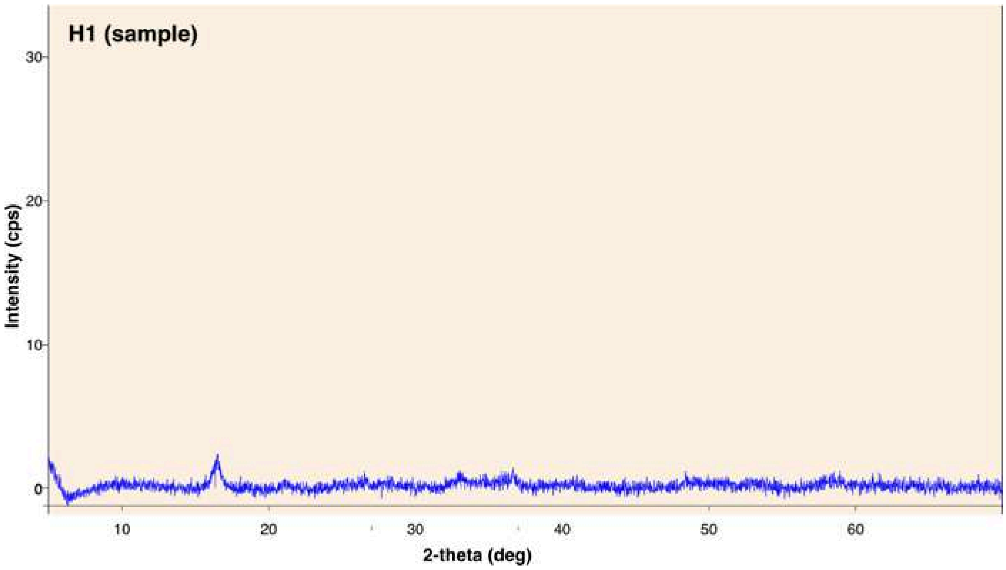

Figure 23. X-ray diffractogram of sample ES-23-H1. No distinct and interpretable XRD pattern was found.

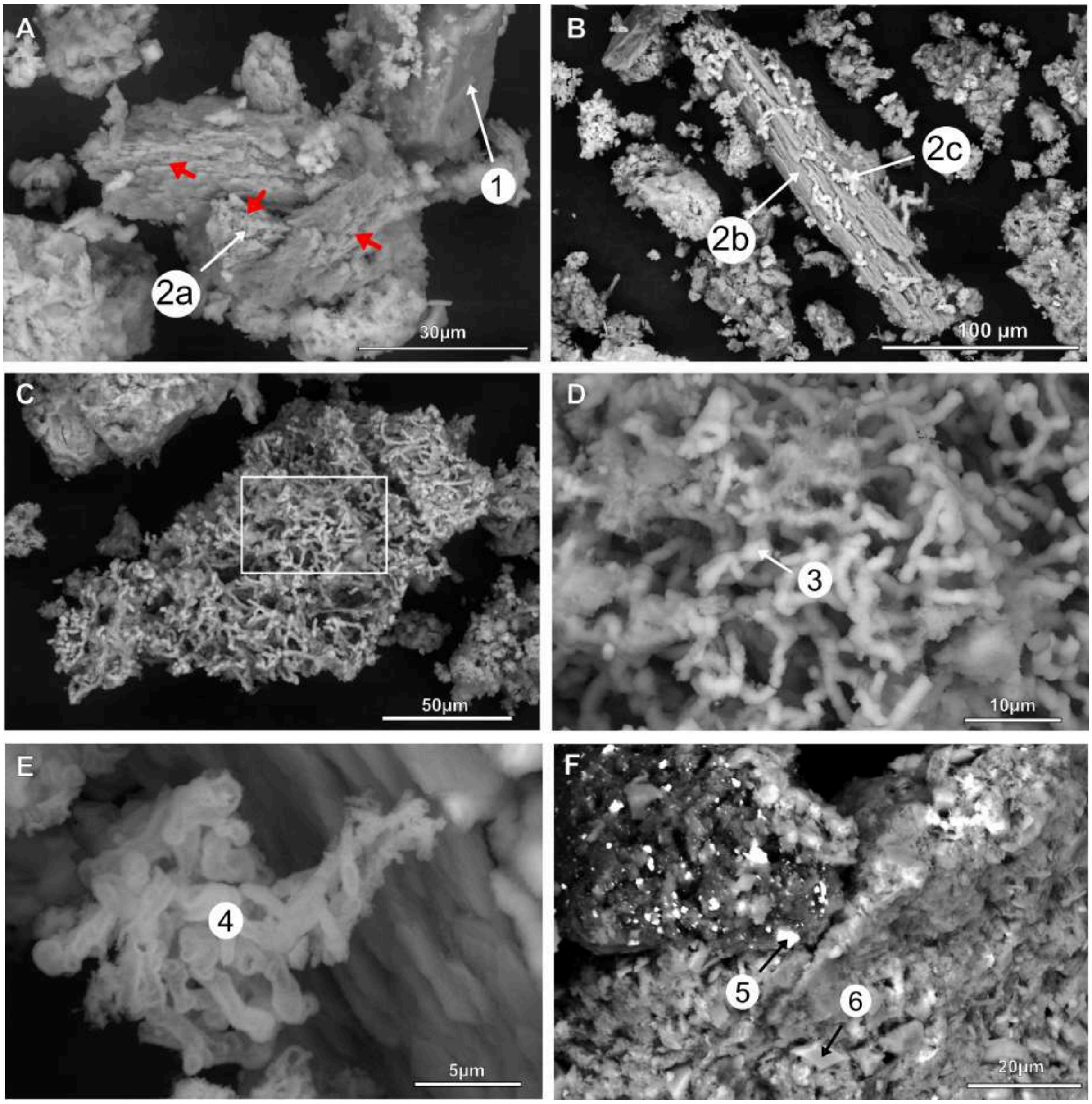

Phases (at%)	O	Fe	S	Si	Al	Ca	Mg	Na	Cl	Ba
1	59	5	1	15	4	3	10	1		
2a	52	5	2	2		33	3			
2b	52	3	1	1		35	5			
2c	62	16	12	2		2.3	3	2	1	
3	63	22	12	2						
4	55	28	2	5	2	3	2	1	1	
5	58	1	10	12	1		10			8
6	59		18			21				

Figure 24. SEM photomicrographs of sample ES-23-H1. Numbers indicate the location of the associated EDS spectra which are shown at the bottom of this figure. **(A)** Silicate mineral rich in magnesium, iron and calcium (Phase 1), and a calcium carbonate mineral rich in iron and magnesium (Phase 2a). Red arrows indicate incomplete faces (porosity, kinked, and stepped faces) in the carbonate particles. **B)** Another calcium carbonate particle rich in iron and magnesium (Phase 2b). The brighter material deposited on the carbonate surface are iron sulfates (Phase 2c). **(C)** Assemblage of rod-shaped sulfate particles, similar to the one observed in (B). **(D)** Close-up of (C) (Phase 3). **(E)** Assemblage of rod-shaped, slightly electronic transparent structures weakly encrusted in mainly iron oxides (Phase 4). **(F)** Concentration of angular baryte particles ranging from 1 to 5 µm in diameter (Phase 5). At the bottom of the picture, a prismatic euhedral gypsum crystal is visible (Phase 6).

Sample ES-23-H2

Sample ES-23-H2 was collected from the upper-east region of the sampling zone. Three main phases were identified from the XRD pattern (Fig. 25): (1) lepidocrocite (γ-FeO(OH)), (2) goethite (α-FeO(OH)), and (3) quartz (SiO_2). Lepidocrocite and goethite are iron oxide-hydroxide minerals that contain ferric iron (Fe^{3+}), i.e., the oxidized form of iron. These minerals are common components of rust. Lepidocrocite has a characteristic reddish hue and may form during subaqueous oxidation of iron-rich materials. The two iron oxides have the same chemical composition (similar EDS spectra). Lepidocrocite tends to form platy-bladed crystals (blades), whereas goethite shows a more prismatic morphology. The aggregates of intersecting blade-shaped crystals seen in Figure 26A,B are thus likely lepidocrocite, while the material occupying interstitial space between lepidocrocite blades is goethite (Fig. 26B,C,D; Phase 2). Goethite is also observed to encrust and cement together elongated thread-like structures, aggregating into clusters (Fig. 26C,D,F). Cell-like structures covered with iron are also observed in the sample (Figure 26E; Phase 3).

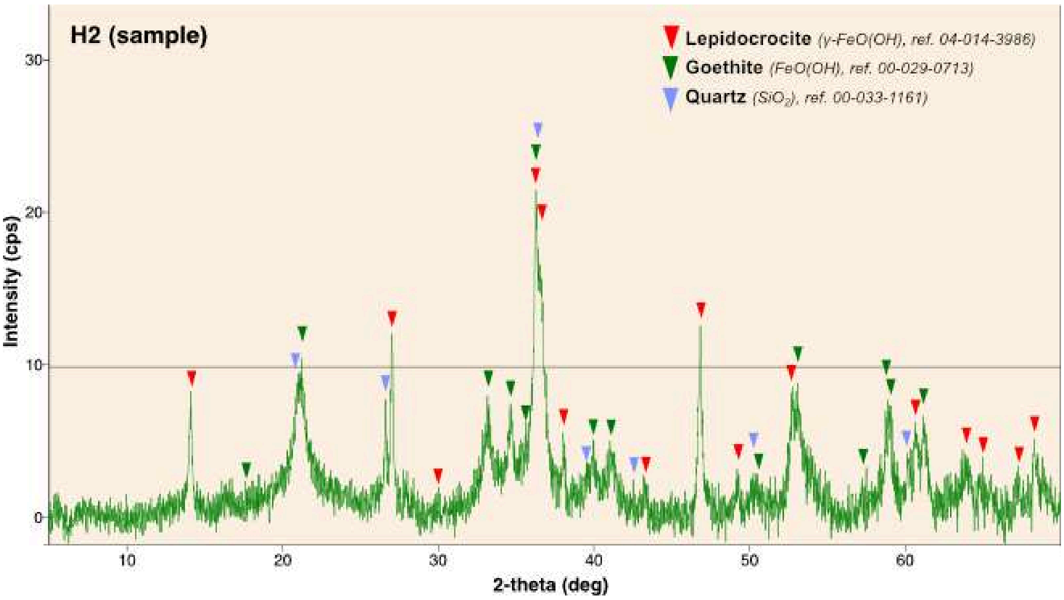

Pos.[°2θ]	Height (cts)	Rel. Int. [%]	Matched by	Reference
14.1152	241.30	32.22	Lepidocrosite	04-014-3986
21.2561	240.41	32.10	Goethite	00-029-0713
26.6564	240.48	32.11	Quartz	00-033-1161
27.0542	436.83	58.32	Lepidocrosite	04-014-3986
33.2474	225.00	30.04	Goethite	00-029-0713
34.6802	244.67	32.67	Goethite	00-029-0713
36.3029	748.99	100.00	Lepidocrosite, Goethite, Quartz	04-014-3986
36.7021	475.95	63.55	Lepidocrosite	04-014-3986
38.0675	164.02	21.90	Lepidocrosite	04-014-3986
40.0153	150.09	20.04	Goethite	00-029-0713
41.0791	131.94	17.62	Goethite	00-029-0713
46.8702	443.41	59.20	Lepidocrosite	04-014-3986
49.2794	91.06	12.16	Lepidocrosite	04-014-3986
50.3710	56.89	7.60	Quartz	00-033-1161
52.7859	278.14	37.14	Lepidocrosite	04-014-3986
59.0472	227.62	30.39	Goethite	00-029-0713
60.7301	185.02	24.70	Lepidocrosite	04-014-3986
61.2106	198.60	26.52	Goethite	00-029-0713
64.0228	90.92	12.14	Lepidocrosite	04-014-3986
65.3571	34.12	4.56	Lepidocrosite	04-014-3986
67.2911	56.97	7.61	Lepidocrosite	04-014-3986
68.3225	163.44	21.82	Lepidocrosite	04-014-3986

Figure 25. X-ray diffractogram of sample ES-23-H2 with diagnostic peaks and matching references in the ICDD PDF-4+ database. The sample comprises three main phases: Lepidocrocite, Goethite and Quartz.

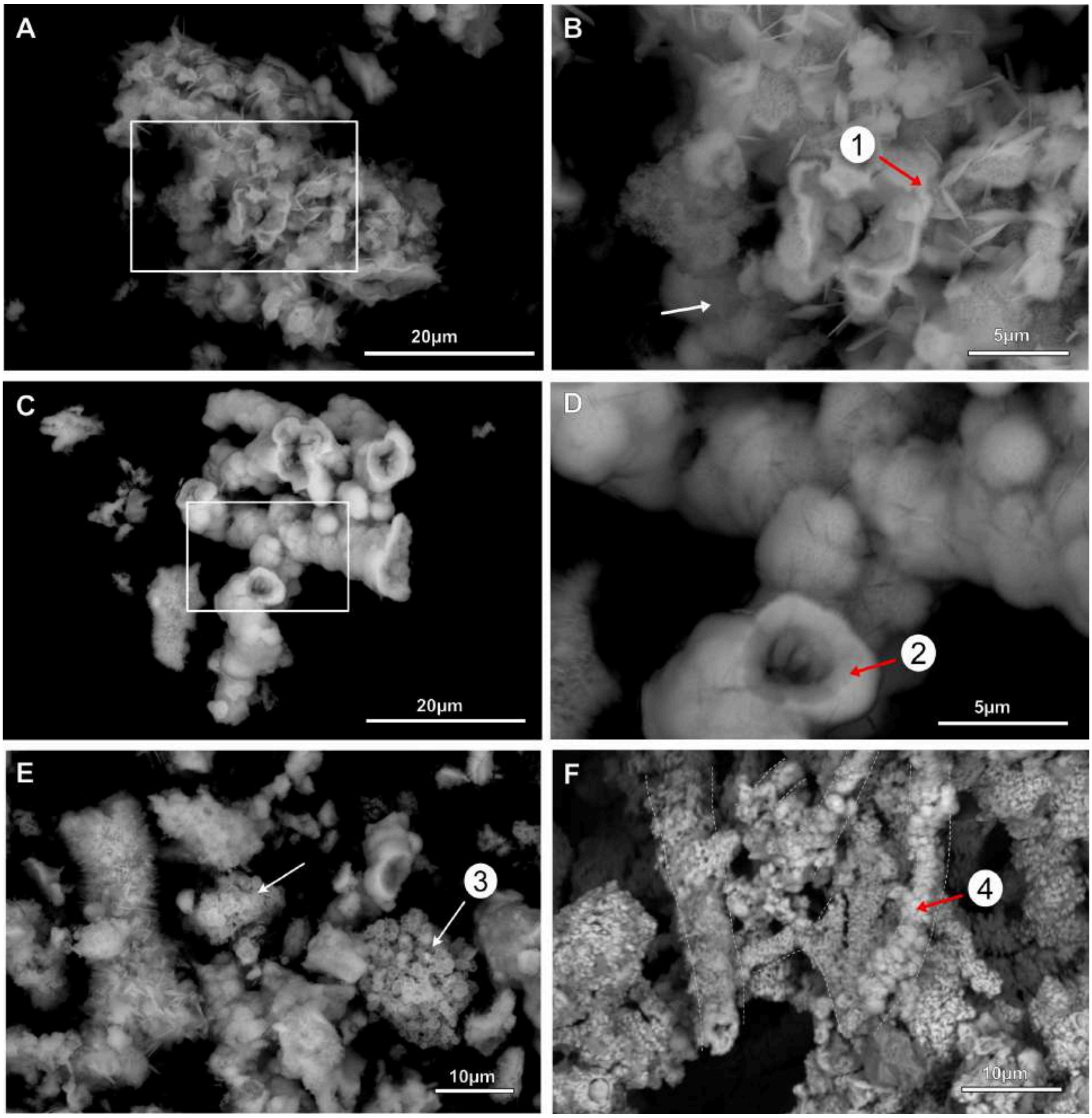

Phases (at%)	O	Si	S	Cl	Fe
1	52	2	1	1	42
2	52	3	1	1	42
3	52	2	1	1	44
4	65				35

Figure 26. SEM photomicrographs of sample ES-23-H2. Numbers indicate the location of the associated EDS spectra shown at the bottom of this figure. **(A)** Aggregates of intersecting blade-shaped crystals, likely lepidocrocite. **(B)** Close-up of (A). The white arrow points to Fe-oxides (likely goethite) occupying interstitial space between lepidocrocite blades. **(C)** Encrusted filament**. (D)** Close-up of (A). **(E)** Cell-like structures (white arrows). **(F)** Details of iron-encrusted filaments (white dotted lines outline the major ones).

Sample ES-23-H3

Sample ES-23-H3 was collected from the upper-east region of the sampling zone. Three main phases were identified from the XRD pattern (Fig. 27): (1) iron sulfate hydroxide hydrate ($Fe_3(SO4)_{0.5}(OH)_6$ $(H_2O)_{3.85}$, IDD reference 04.015-7875), (2) green rust ($Fe_2O_3 \bullet H_2O$, IDD reference 00-013-092), and (3) minor amounts of Mg-bearing calcite (IDD reference 00-013-0092). The iron sulfate hydroxide hydrate has a composition corresponding to a green rust-containing sulfate (GR-SO_4). The iron sulfate phase (GR-SO_4) and green rust ($Fe_2O_3 \bullet H_2O$) exhibit similar peak patterns. Nevertheless, the sample shows both phases, as evidenced by the consistent occurrence of double peaks at elevated 2-theta values, highlighting the phase shift between them (Fig. 28).

Microscopy analyses confirm the presence of iron-rich minerals containing varying amounts of sulfur (Figs. 29A,B; Phase 1). Larger particles mainly containing iron, oxygen and sulfur as well as traces of calcium are dispersed throughout the sample (Fig. 29C,D; Phase 3). Spherical iron sulfide particles (~5 µm in diameter) are also observed and often seen on the surface of other particles (Fig. 29C, D; Phase 2). These spherules have a wad-like texture and typically coalesce to form larger particles (Fig. 29D). Element mapping constrains the possible mineralogy by highlighting the correlation between sulfur (S) and iron (Fe) with a decrease in oxygen content, consistent with an iron sulfide mineral such as pyrite (Fig. 30). Nevertheless, the XRD analysis did not detect any pyrite or other FeS phase. This may be attributed to either the absence of a crystalline structure or an abundance below the XRD detection threshold of 5%. The sample also contains a substantial amount of calcium carbonates rich in iron and minor amounts of magnesium (Figure 29E, F; Phase 4).

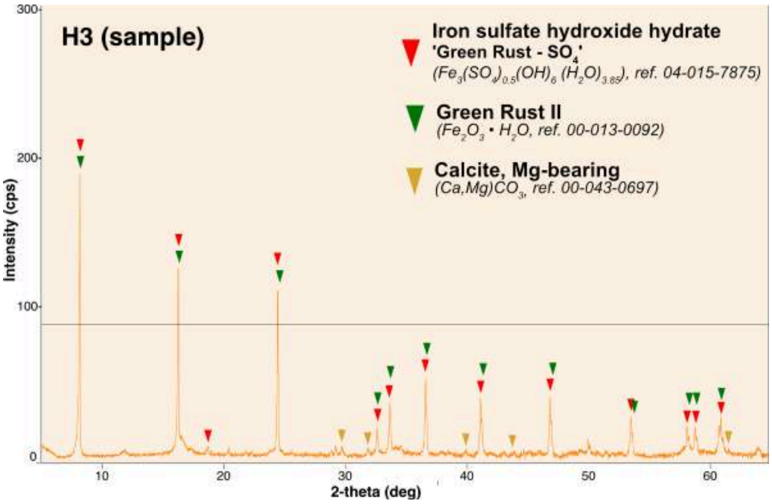

Pos.[°2θ]	Height (cts)	Rel. Int. [%]	Matched by	ICDD Ref
8.0743	6097.27	100.00	Iron sulfate hydroxide hydrate (GR-SO_4) Green Rust II	04-015-7875 00-013-0092
16.1789	4326.16	70.95	Iron sulfate hydroxide hydrate (GR-SO_4) Green Rust II	04-015-7875 00-013-0092
18.6207	210.89	3.46	Iron sulfate hydroxide hydrate	04-015-7875
24.3625	3688.59	60.50	Iron sulfate hydroxide hydrate	04-015-7875
29.6341	211.37	3.47	Mg-Bearing Calcite	00-013-0092
31.7658	174.60	2.86	Mg-Bearing Calcite	00-013-0092
32.5274	651.75	10.69	Iron sulfate hydroxide hydrate (GR-SO_4) Green Rust II	04-015-7875 00-013-0092
33.5666	1226.60	20.12	Iron sulfate hydroxide hydrate (GR-SO_4) Green Rust II	04-015-7875 00-013-0092
36.5031	1867.86	30.63	Iron sulfate hydroxide hydrate (GR-SO_4) Green Rust II	04-015-7875 00-013-0092
39.7776	83.05	1.36	Mg-Bearing Calcite	00-013-0092
41.0179	1340.02	21.98	Iron sulfate hydroxide hydrate Green Rust II	04-015-7875 00-013-0092
43.8049	78.68	1.29	Mg-Bearing Calcite	00-013-0092
46.7301	1460.61	23.96	Iron sulfate hydroxide hydrate Green Rust II	04-015-7875 00-013-0092
53.3664	911.14	14.94	Iron sulfate hydroxide hydrate (GR-SO_4) Green Rust II	04-015-7875 00-013-0092
57.9906	708.64	11.62	Iron sulfate hydroxide hydrate (GR-SO_4) Green Rust II	04-015-7875 00-013-0092
58.6408	634.23	10.40	Iron sulfate hydroxide hydrate (GR-SO_4) Green Rust II	04-015-7875 00-013-0092
60.7929	912.79	14.97	Iron sulfate hydroxide hydrate (GR-SO_4) Green Rust II	04-015-7875 00-013-0092

Figure 27. X-ray diffractogram of Sample ES-23-H3 with diagnostic peaks and matching references in the ICDD PDF-4+ database. The sample comprises an iron sulfate-bearing phase, green rust, and Mg-bearing calcite. Although peaks for iron sulfate and green rust phases are very close, dual peaks are clearly visible with higher 2-theta values.

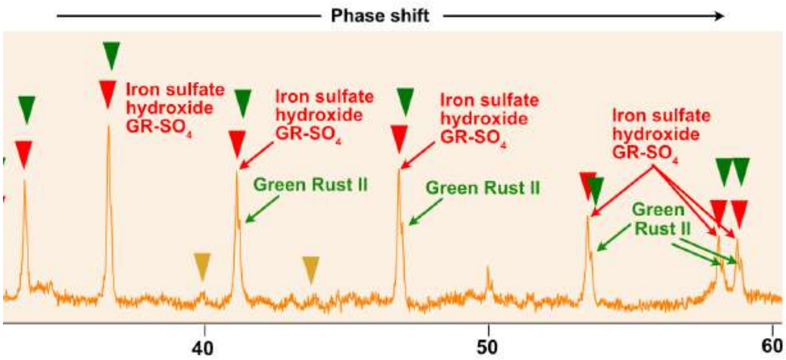

Figure 28. Details of the X-ray diffractogram of sample ES-23-H3 showing the phase shift between iron sulfate hydroxide and green rust, indicating the presence of both phases in the sample.

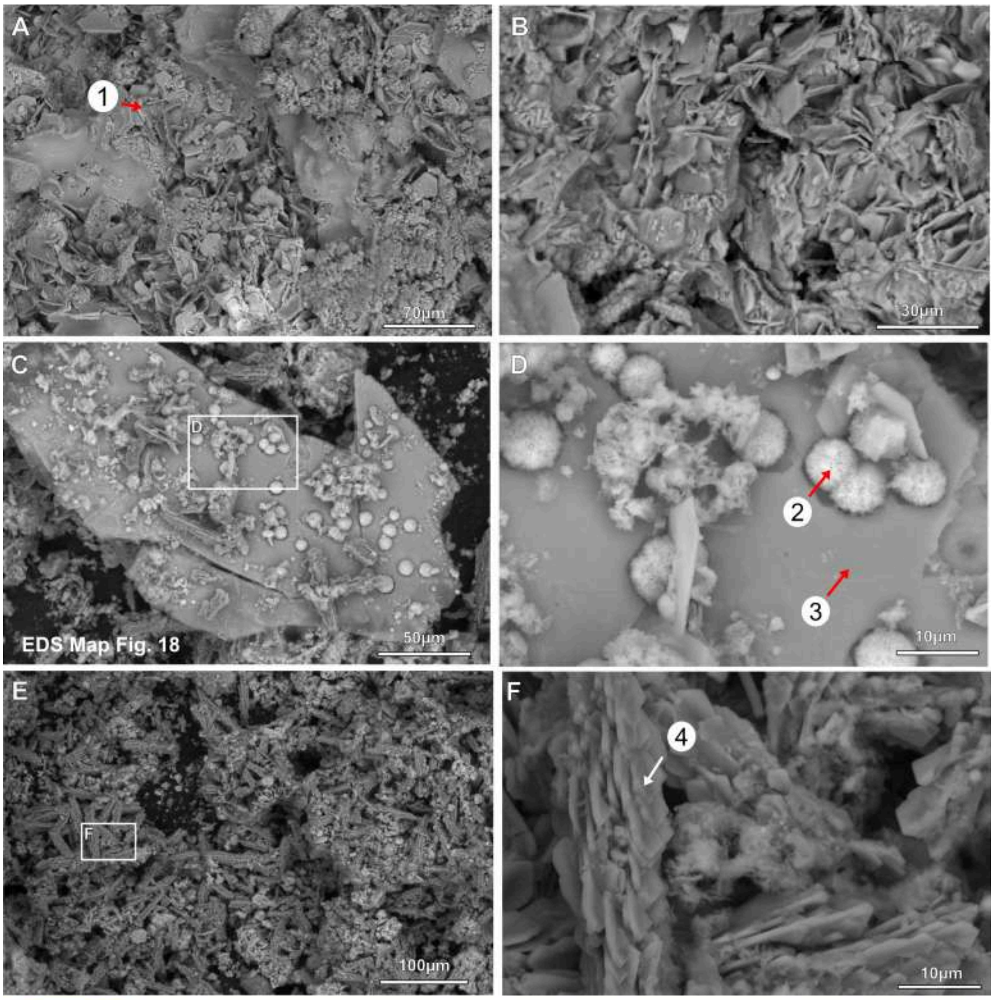

Phases (at%)	O	Na	Si	S	Cl	Ca	Fe
1	63			6			30
2	61	2	1	12	2	1	21
3	56	4	1	7	1	4	27
4	53		1	2	1	18	24

Figure 29. SEM photomicrographs of sample ES-23-H3. Numbers indicate the location of the associated EDS spectra shown at the bottom of this figure. **(A)** Blady iron-rich precipitates containing varying amounts of sulfur. **(B)**. Details of intersecting blade-shaped crystals. **(C)** Spherical particles consistent with an iron sulfide mineral such as pyrite (see elemental mapping in Fig. 30). **(D)**. Close-up of (C) (Phase 2). The underlying mineral consists mainly of iron, oxygen, and sulfur, and minor amounts of calcium. **(E)** Aggregates of calcium-iron carbonate scales, with minor amounts of magnesium. **F)** Close-up of (E).

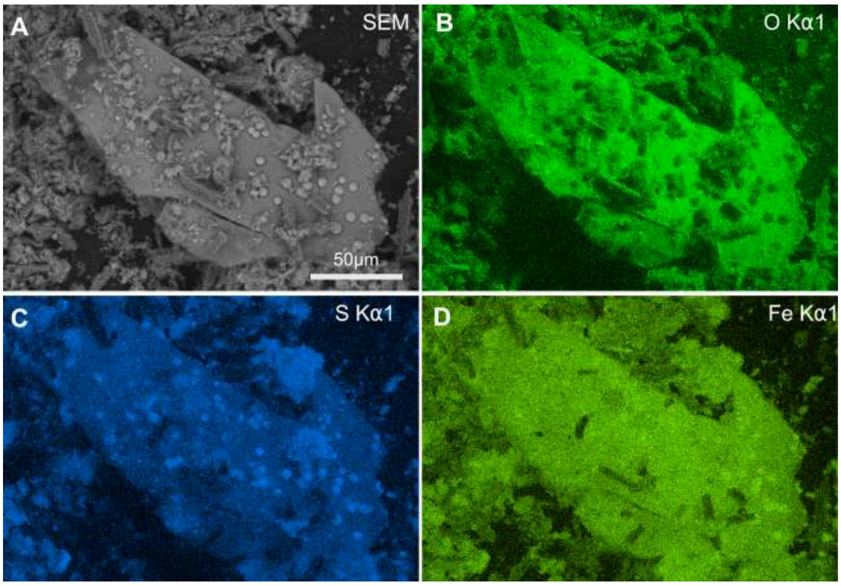

Figure 30. Elemental mapping of sample ES-23-H3 showing the correlation between sulfur (S) and iron (Fe) in the spherulites with a decrease in oxygen (O) content, which could be consistent with an iron sulfide mineral such as Pyrite.

Sample ES-23-H10

Sample ES-23-H10 was collected from the lower west region of the sampling zone. Three main phases were identified from the XRD pattern (Fig. 31): (1) iron sulfate hydroxide hydrate (IDD reference 04-015-7875) also called green rust containing sulfate (GR-SO_4) (2) low-Mg calcite (IDD reference 04-026-3167; $Ca_{0.871}$, $Mg_{0.129}$ CO_3), and (3) iron-sulfide (FeS, 04-067-0413).

SEM-EDS analyses showed that the sample is rich in subhedral to euhedral microsparitic carbonate crystals (grain size between 4 and 40 µm in diameter, Fig. 33B, C). Some of these carbonates are elongated with the longest dimension around 15 µm (Fig. 33B; Phase 3a), while others are equant with a diameter around 5 µm (Fig. 33C; Phase 3b). The elongated crystals consistently contain more iron and magnesium relative to calcium compared to the equant crystals. The carbonate crystals are embedded in a matrix mainly consisting of iron oxide and sulfur (Fig. 33A, Phase 1 and 2). The sample also contains many steel fragments having a pearlitic microstructure, a two-phased lamellar structure composed of alternating layers of ferrite and cementite, resulting in a characteristic zebra pattern (Fig. 33D, Phase 4). The steel fragments are embedded in a matrix that is enriched in sulfur and the boundary between the steel fragments and the surrounding matrix is often blurred (Fig. 33E, Phase 5 and 6). Progressive degradation stages of the pearlitic steel structure are observed in the sample (Fig. 32). There are also occasional subcubic particles (~µm) and diatoms in the sample (Fig. 33F).

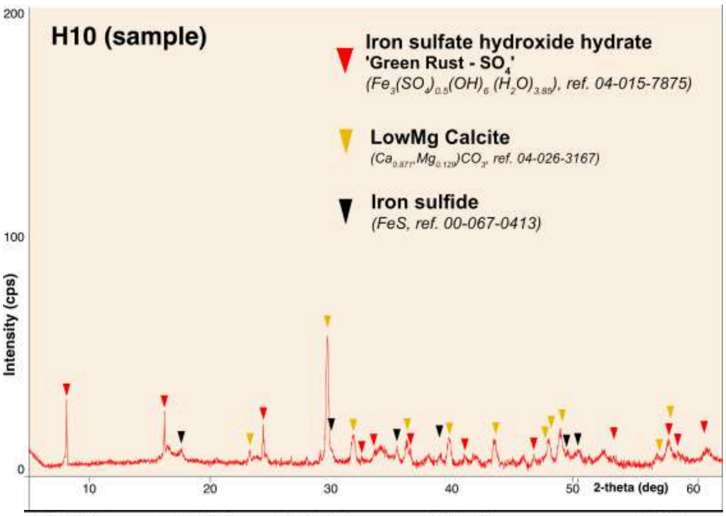

Pos.[°2θ]	Height (cts)	Rel. Int. [%]	Matched by	ICDD Ref
8.1240	915.35	42.78	Iron sulfate hydroxide (GR-SO_4)	04-015-7879
16.2246	733.00	34.26	Iron sulfate hydroxide (GR-SO_4)	*04-015-7879*
17.6383	193.72	9.05	Iron sulfide	00-067-0413
23.2974	206.70	9.66	Low-Mg Calcite	*04-026-3167*
24.4052	587.57	27.46	Iron sulfate hydroxide (GR-SO_4)	*04-015-7879*
26.7037	107.17	5.01	Low-Mg Calcite	*04-026-3167*
29.7091	2139.56	100.00	Low-Mg Calcite	*04-026-3167*
31.8716	470.78	22.00	Low-Mg Calcite	*04-026-3167*
33.5989	191.57	8.95	Iron sulfate hydroxide (GR-SO_4)	*04-015-7879*
35.4567	248.14	11.60	Iron sulfide	*00-067-0413*
36.3198	321.81	15.04	low-Mg Calcite	*04-026-3167*
36.5599	231.86	10.84	Iron sulfate hydroxide (GR-SO_4)	*04-015-7879*
39.0338	142.43	6.66	Iron sulfide	*00-067-0413*
39.7545	444.26	20.76	Low-Mg Calcite	*04-026-3167*
41.1045	130.02	6.08	Iron sulfate hydroxide (GR-SO_4)	*04-015-7879*
43.4539	390.76	18.26	Low-Mg Calcite	*04-026-3167*
46.7957	156.85	7.33	Iron sulfate hydroxide (GR-SO_4)	*04-015-7879*
47.9685	382.34	17.87	Low-Mg Calcite	*04-026-3167*
48.9110	525.85	24.58	Low-Mg Calcite	*04-026-3167*
50.5219	233.81	10.93	Iron sulfide	*00-067-0413*
56.9905	164.20	7.67	Low-Mg Calcite	*04-026-3167*
57.9190	409.96	19.16	Iron sulfate hydroxide (GR-SO_4)	*04-015-7879*
61.2500	227.05	10.61	Iron sulfate hydroxide (GR-SO_4)	*04-015-7879*

Figure 31. X-ray diffractogram of sample ES-23-H10 with diagnostic peaks and matching references in the ICDD PDF-4+ database, showing the presence of three main phases: iron-sulfate hydroxide hydrate, low-Mg calcite, and iron sulfide.

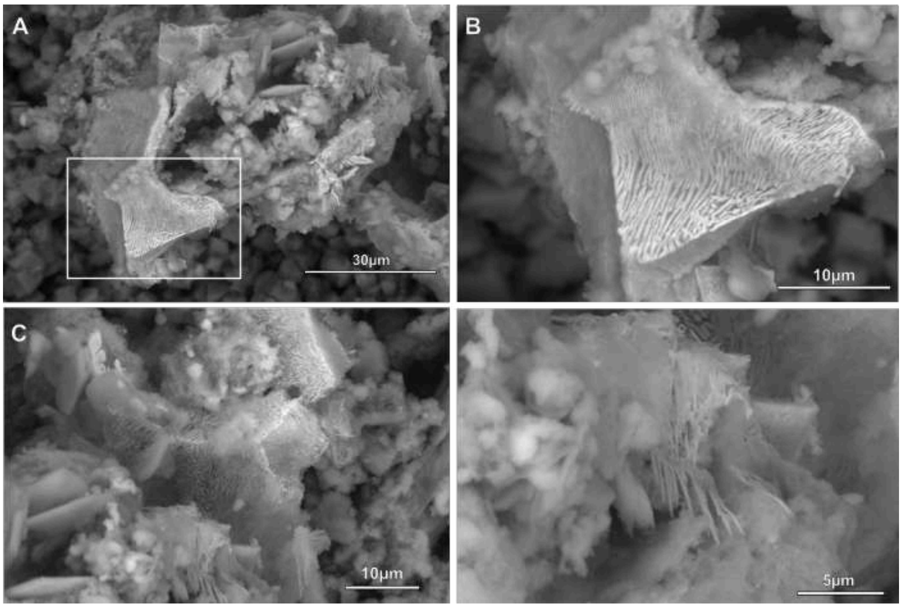

Figure 32. SEM photomicrographs of steel corrosion. Details of the pearlitic structure and its degradation with time.

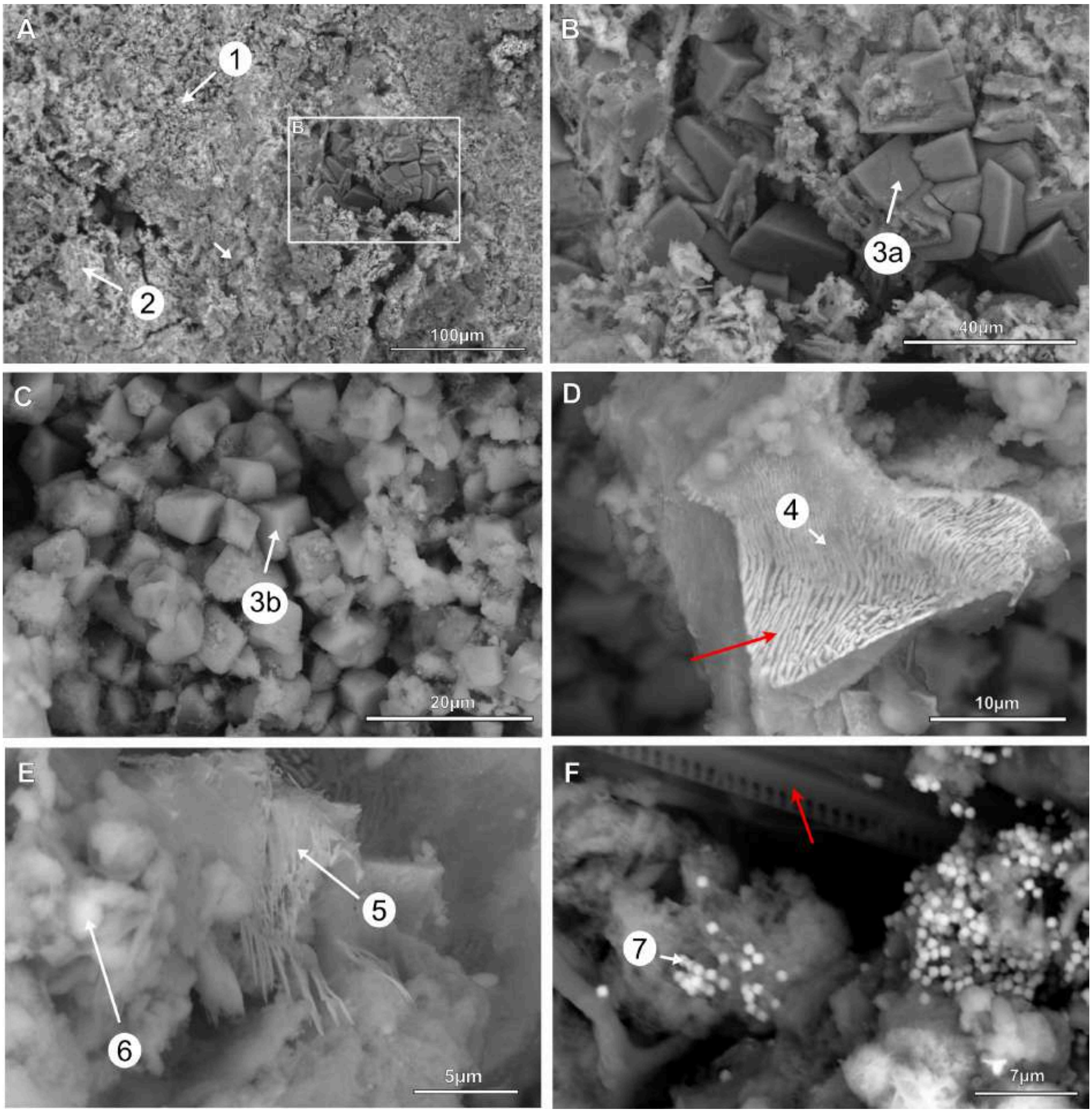

Phases (at%)	O	Mg	Si	S	Ca	Fe
1	58	3	2	7	3	25
2	61	2	2	10	2	23
3a	54	1	1	4	27	11
3b	53	1	2	3	32	8
4	54	1	1	3	3	36
5	54	1	1	4	2	33
6	61	2	3	11	2	18
7	52	1	1	2	35	7

Figure 33. SEM photomicrographs of sample ES-23-H10. Numbers indicate the location of the associated EDS spectra shown at the bottom of this figure. **(A)** Overview of the sample showing carbonate crystals (white box) embedded in a matrix mainly consisting of iron, oxide and sulfur (Phases 1 and 2). **(B)** Close-up of the white square in (A). Elongated calcium carbonate crystals incorporating iron and minor amounts of magnesium (Phase 3a). **(C)** Equant calcium carbonate crystals with rounded edges (Phase 3b) containing less iron and magnesium compared to the larger, elongated crystals (Phase 3a). **(D)** Steel fragment having a pearlitic microstructure composed of alternating layers of ferrite (dark) and cementite (bright) (indicated by a red arrow) (Phase 4). **(E)** Degraded steel fragments (Phase 5) embedded in a matrix enriched in sulfur (Phase 6). **(F)** Subcubic particles (~1µm) rich in iron and sulfur, consistent with iron sulfide minerals (e.g., pyrite) (Phase 7), alongside diatoms (red arrow).

Sample ES-23-H11

Sample ES-23-H11 was collected from the lower west region of the sampling zone. The XRD pattern indicates the presence of three main phases (Fig. 34): (1) quartz (IDD reference 00-033-1161), (2) feldspars (calcium aluminium silicate, IDD reference 00-052-1344), and (3) low-Mg calcite (IDD reference 04-026-3167).

Although the sample contains a substantial amount of clastic sediment (Fig. 35), SEM-EDS analyses revealed a substantial amount of iron-rich phases, coating filaments, as well as needle-like and granular iron-containing phases (refer to Fig. 35A, B, C). Iron-rich calcium carbonate rods are also observed (Fig. 35A, B). Iron-bearing phases were located in between the silicate grains (Fig. 35D, 36). The acicular and the grainy texture of the Fe-bearing phase was clearly recognized and differentiated within the sample (Fig. 35C).

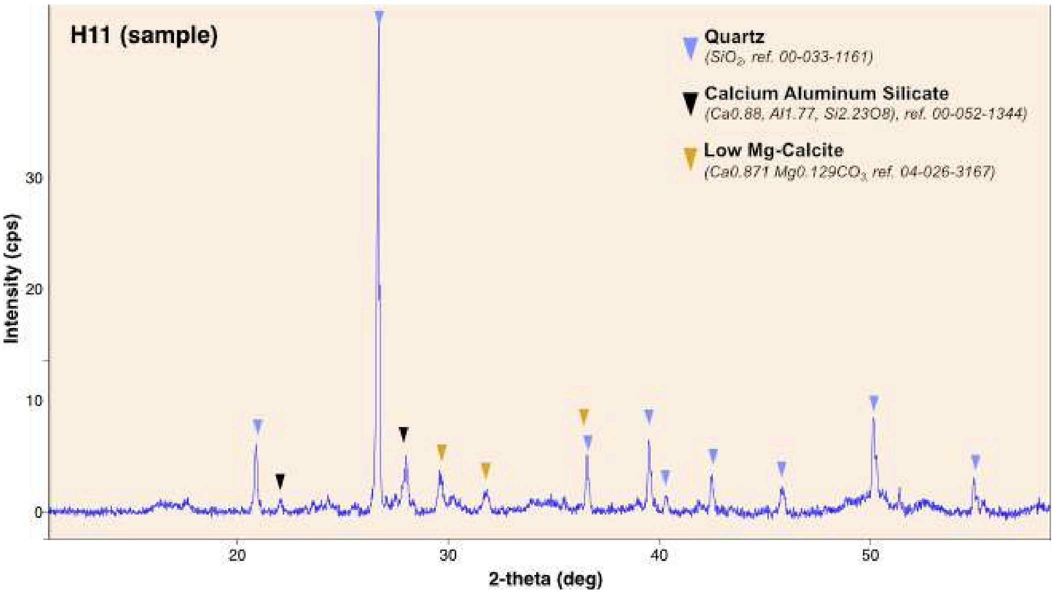

Pos.[°2θ]	Height (cts)	Rel. Int. [%]	Matched by	ICDD Ref
20.8525	599.80	13.94	Quartz	00-033-1161
22.0468	107.33	2.49	Calcium Aluminum Silicate	04-052-1344
26.6849	4302.30	100.00	Quartz	00-033-1161
28.0147	469.58	10.91	Calcium Aluminum Silicate	04-052-1344
29.6181	272.07	6.32	low-Mg Calcite	04-026-3167
31.8417	175.22	4.07	low-Mg Calcite	04-026-3167
36.5649	508.02	11.81	Quartz	00-033-1161
39.4984	667.69	15.52	Quartz	00-033-1161
40.3153	148.57	3.45	Quartz	00-033-1161
42.4716	342.88	7.97	Quartz	00-033-1161
45.7852	243.11	5.65	Quartz	00-033-1161
50.1112	860.34	20.00	Quartz	00-033-1161
54.9068	326.82	7.60	Quartz	00-033-1161

Figure 34. X-ray diffractogram of sample ES-23-11 with diagnostic peaks and matching references in the ICDD PDF-4+ database. The sample is dominated by siliciclastic sediments (quartz and feldspar minerals) with traces of low-Mg Calcite.

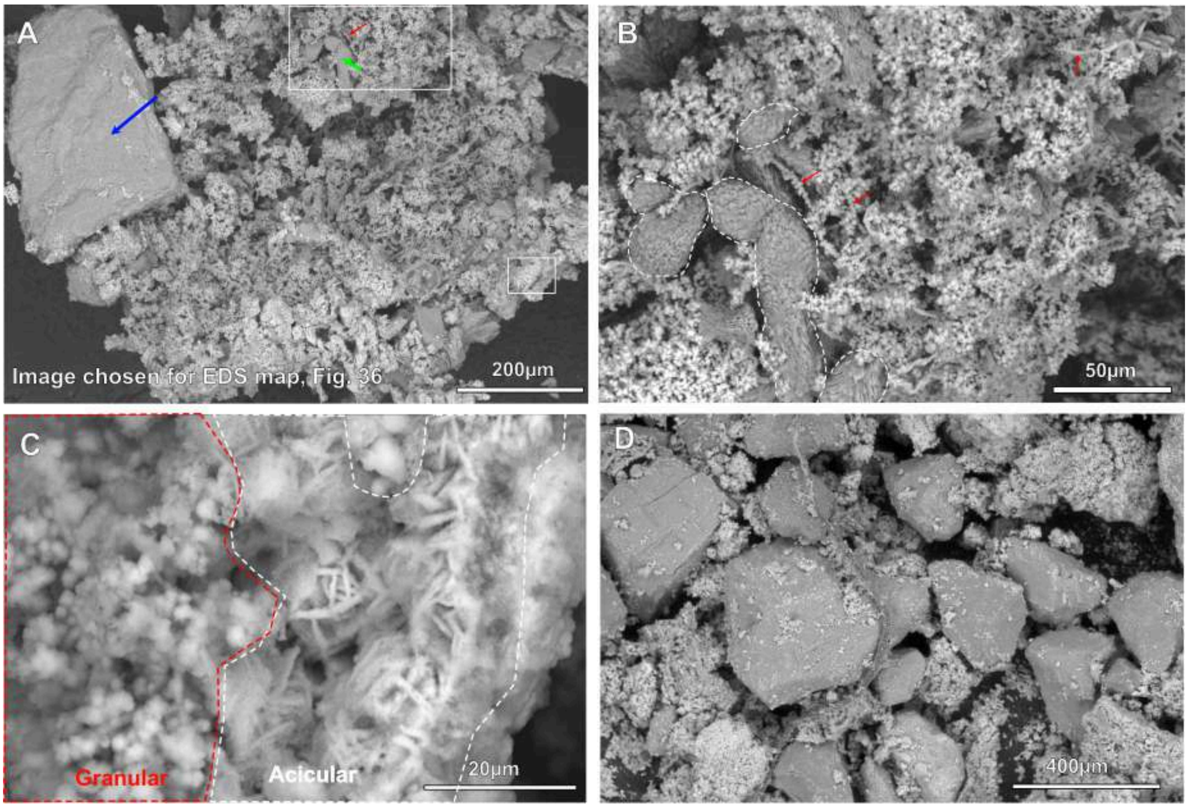

Figure 35. SEM photomicrographs of sample ES-23-H11. **(A)** Overview of the sample showing various microstructures representing the main bulk of the sample: siliciclastic particles (blue arrow), carbonate rods (green arrow), iron oxide encrusted filaments (red arrow), as well as platy and grainy iron-bearing phases (see elemental mapping in Fig. 36). **(B)** Close-up of (A) (upper right) showing rounded, rod-like morphology of the carbonates (white dashed lines) and encrusted filaments (red arrows). **(C)** details of (A) (lower right) showing the platy/acicular (white dash) and granular (red dash) texture of the Fe-S-bearing phase. **(D)** Siliciclastic sediments composing a large part of the sample.

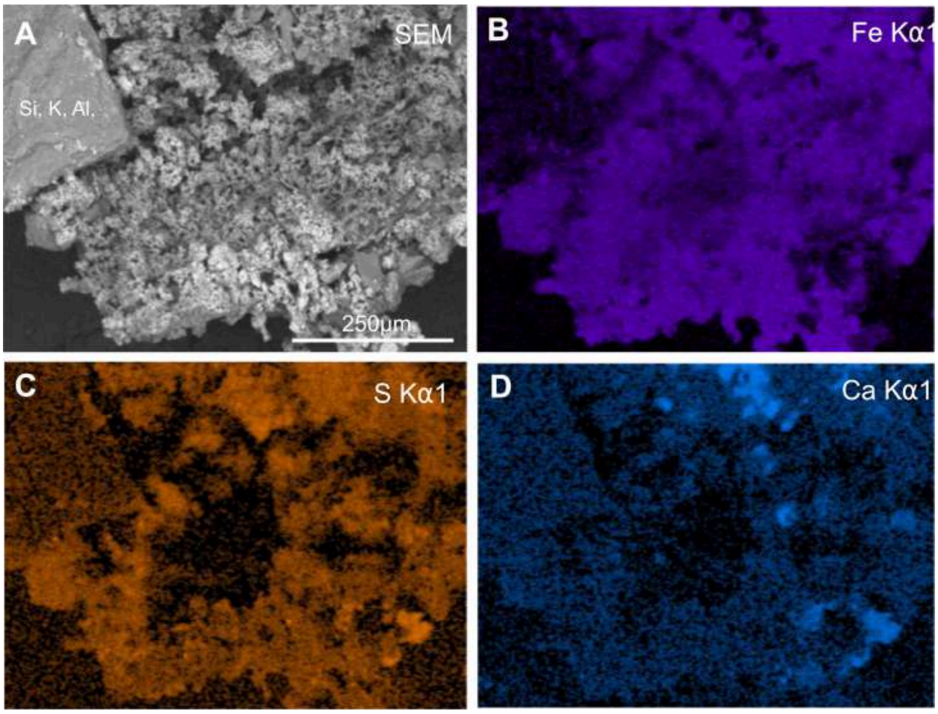

Figure 36. EDS mapping showing the chemical composition of certain phases described in Fig. 35A. **(A)** SEM image of the analyzed area. **(B)** Iron distribution in the sample area. **(C)** Sulfur distribution co-occurring with iron **(D)** Calcium distribution in the sample area, indicating that the rods observed in Fig. 35B are composed of calcium carbonate.

Sample ES-23-H13

Sample ES-23-H13 was scraped off the steel plate cut-out from the lower east area of the sampling zone. The sample was mounted in epoxy and polished to enable SEM observation of cross-sections. The XRD analysis identified two iron phases, similar to those identified in ES-23-H3 (Fig. 37): green rust I, (Fe_2O_3•H_2O, IDD reference 00-013-0092), and (2) iron sulfate hydroxide hydrate ($Fe^3(SO4)_{0.5}(OH)_6$ $(H_2O)_{3.85}$, IDD reference 04.015-7875), also called green rust containing sulfate (GR-SO_4).

SEM imaging confirmed the presence of iron in combination with sulfur and/or oxygen in various particle morphologies. The most frequently occurring particles are bladed sulfur-bearing iron oxides (Fig. 38B, D, F, and G; Phase 2a, 2b) and wad-like precipitates that mainly occupy interstitial space between other particles (Fig. 38B, D and G; Phase 3a, 3b). Wad-like precipitates are systematically more enriched in sulfur compared to the bladed crystals. The sample also contains steel fragments having a pearlitic microstructure (Fig. 38B, C, and F, Phase 1). Although iron sulfide minerals were not discernible in the X-ray diffraction analysis, they were detected as precipitates on silicate particles using the SEM-EDS method (Fig. 38H; Phase 5). The sample also contains a high-density particle composed of iron, cobalt, copper, and tin (Fig. 38E; Phase 4). This is likely a paint fragment from the vessel.

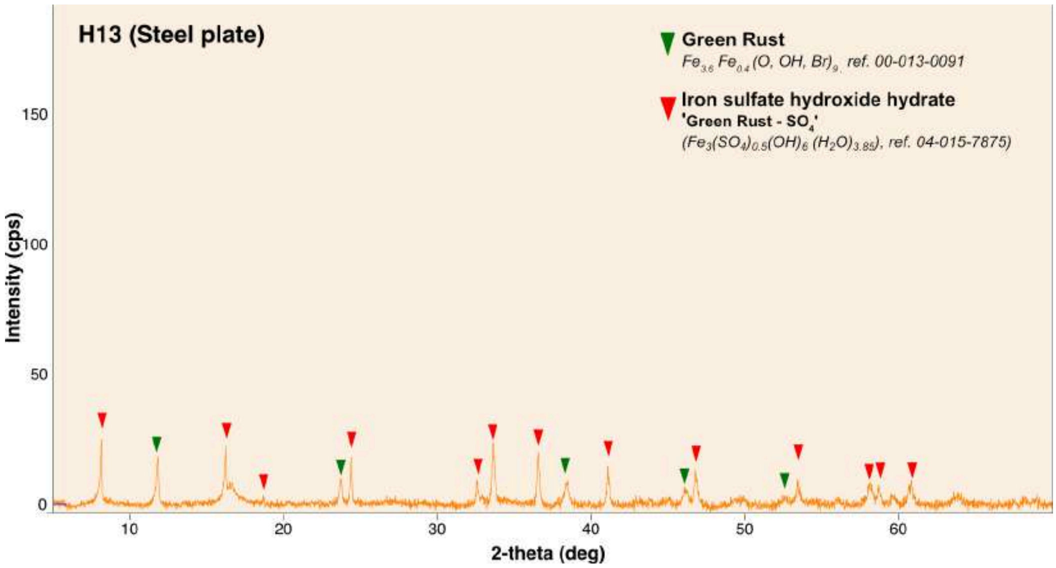

ES-23-H13

Pos.[°2θ]	Height (cts)	Rel. Int. [%]	Matched by	ICDD Ref
8.0778	832.75	90.43	Iron sulfate hydroxide hydrate (GR-SO_4)	04-015-7875
11.7934	697.82	75.78	Green Rust	00-013-0091
16.1822	779.57	84.65	Iron sulfate hydroxide hydrate (GR-SO_4)	04-015-7875
18.6068	92.81	10.08	Iron sulfate hydroxide hydrate (GR-SO_4)	04-015-7875
23.6799	352.80	38.31	Green Rust	00-013-0091
24.3572	612.24	66.48	Iron sulfate hydroxide hydrate (GR-SO_4)	04-015-7875
32.5222	345.49	37.52	Iron sulfate hydroxide hydrate (GR-SO_4)	04-015-7875
33.5637	920.90	100.00	Iron sulfate hydroxide hydrate (GR-SO_4)	04-015-7875
36.5184	800.47	86.92	Iron sulfate hydroxide hydrate (GR-SO_4)	04-015-7875
38.3988	360.99	39.20	Green Rust	00-013-0091
41.0391	513.43	55.75	Iron sulfate hydroxide hydrate (GR-SO_4)	04-015-7875
46.0973	234.00	25.41	Green Rust	00-013-0091
46.7477	524.74	56.98	Iron sulfate hydroxide hydrate (GR-SO_4)	04-015-7875
52.4884	121.58	13.20	Green Rust	00-013-0091
53.3844	337.34	36.63	Iron sulfate hydroxide hydrate (GR-SO_4)	04-015-7875
58.0303	358.92	38.97	Iron sulfate hydroxide hydrate (GR-SO_4)	04-015-7875
58.6372	319.60	34.71	Iron sulfate hydroxide hydrate (GR-SO_4)	04-015-7875
60.7971	382.02	41.48	Iron sulfate hydroxide hydrate (GR-SO_4)	04-015-7875

Figure 37. X-ray diffractogram of sample ES-23-H13 with diagnostic peaks and matching references in the ICDD PDF-4+ database.

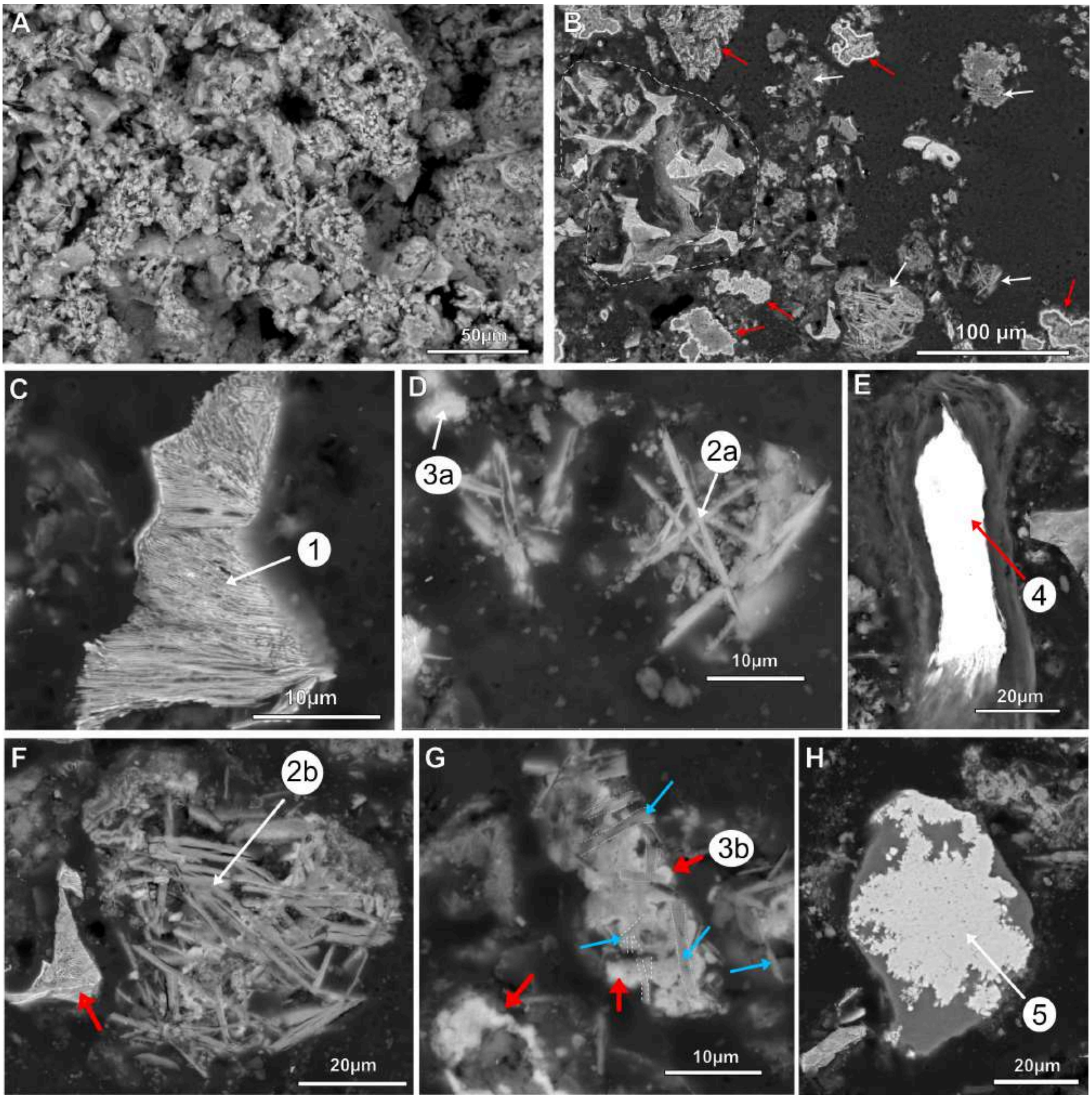

Phases (at%)	O	Na	Si	S	Cl	Mn	Fe	Co	Cu	Ni	Sn
1	17		1	3	1	1	76	1		1	
2a	62			5	1		32				
2b	62	2		6			30				
3a	50		1	14			33				
3b	48		2	15			35				
4							79	11	8		1
5				66			34				

Figure 38. SEM photomicrographs of sample ES-23-H13. Numbers indicate the location of the associated EDS spectra which are shown in the table at the bottom of the figure. **(A)** Sample overview. **(B)** Cross section showing iron-rich particles. Dashed white circles highlight a zone with steel fragments. White arrows point to bladed crystals. Red arrows point to wad-like precipitates. **(C)** Close-up of a steel fragment having a pearlitic microstructure (1). **(D)** Bladed sulfur-bearing iron-oxides (2a) and more sulfur-enriched wad-like precipitates (3a). **(E)** Cross-section of a highly electron-reflective particle, potentially a paint fragment (4). **F)** Cross-section through randomly distributed bladed crystals (2b). The red arrow points to a steel fragment showing pearlitic structure. **(G)** Cross-section showing wad-like precipitates (red arrows, (3b)) occupying interstitial space between bladed crystals (blue arrows). EDS spectrum shows the wad-like texture. **(H)** Cross-section of iron sulfides that have precipitated on a silicate particle. SEM images from parts (B) to (H) were captured on diamond-polished sections of epoxy-embedded samples (5).

Group 4 – Beam deposit samples

Sample ES-23-H8

Sample ES-23-H8 was retrieved from the beam resting on the seafloor (beam side furthest away from the shipwreck) (Fig. 3). Five main phases were identified from the XRD pattern (Fig. 39): (1) green rust I (Fe_2O_3•H_2O, IDD reference 00-013-0092), (2) iron sulfate hydroxide hydrate ($Fe_3(SO_4)_{0.5}(OH)_6$ $(H_2O)_{3.85}$, IDD reference 04-015-7875), (3) quartz (SiO_2, IDD reference 00-033-1161, (4) Mg-bearing calcite $(Ca,Mg)CO_3$, IDD reference 00-043-0697), and (5) halite (NaCl, IDD reference 00-005-0628).

SEM-EDS confirms that the sample consists of iron-rich material mixed with siliciclastic sediment, The iron-rich particles include a platy phase mainly consisting of iron, oxygen and sulfur (Figs. 40A,B; Phase 2), framboidal pyrite (Fig. 40C, Phase 3), and encrusted filaments (Fig. 40D). EDS analysis of a larger area containing platy particles confirms the predominance of iron and oxygen and to a lesser extent sulfur. Trace elements such as copper (Cu), nickel (Ni), and manganese (Mn) are also present. Occasionally there are cavities formed on the surface of the platy iron-oxide-sulfur crystals. (Fig. 40B).

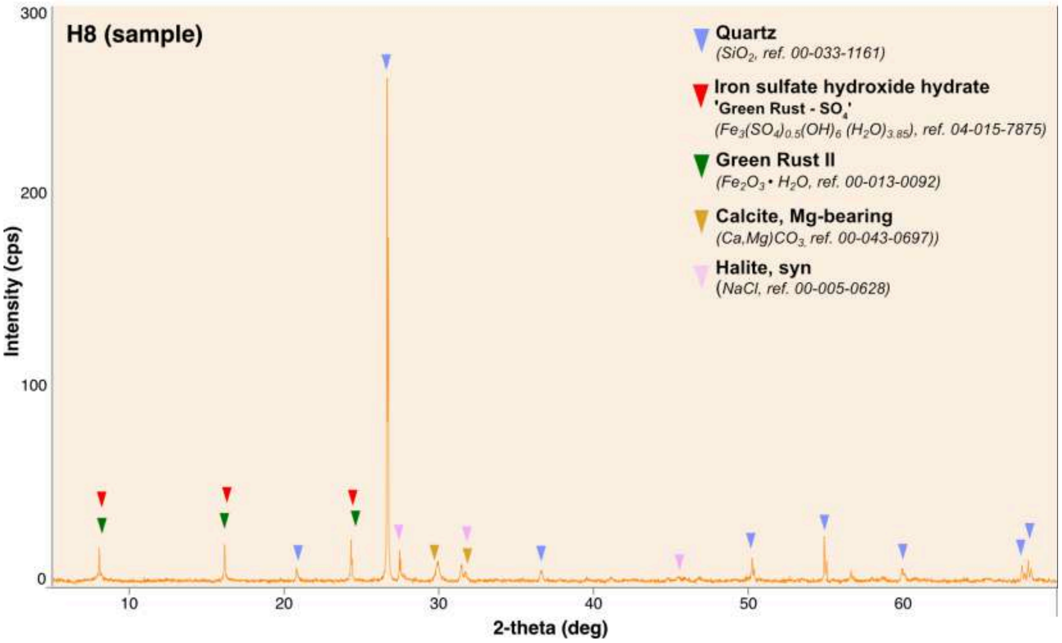

Pos.[°2θ]	Height (cts)	Rel. Int. [%]	Matched by	ICDD Ref
7.9923	484.72	7.52	Iron sulfate hydroxide (GR-SO_4) Green Rust II	04-015-7875 00-013-0092
16.0985	644.10	10.00	Iron sulfate hydroxide (GR-SO_4) Green Rust II	04-015-7875 00-013-0092
20.7503	225.08	3.49	Quartz	00-033-1161
24.2896	572.62	8.89	Iron sulfate hydroxide (GR-SO_4) Green Rust II	04-015-7875 00-013-0092
26.6249	6443.84	100.00	Quartz	00-033-1161
27.4195	400.51	6.22	Halite	00-005-0628
29.9009	378.40	5.87	Mg-bearing Calcite	00-013-0092
31.4261	307.40	4.77	Mg-bearing Calcite Halite	00-013-0092 00-005-0628
36.5325	164.12	2.55	Quartz	00-033-1161
45.4080	72.67	1.13	Halite	00-005-0628
50.1638	409.63	6.36	Quartz	00-033-1161
59.9692	215.48	3.34	Quartz	00-033-1161
67.7225	274.40	4.26	Quartz	00-033-1161
68.1926	146.52	2.27	Quartz	00-033-1161

Figure 39. X-ray diffractogram of sample ES-23-H8 with diagnostic peaks and matching references in the ICDD PDF-4+ database.

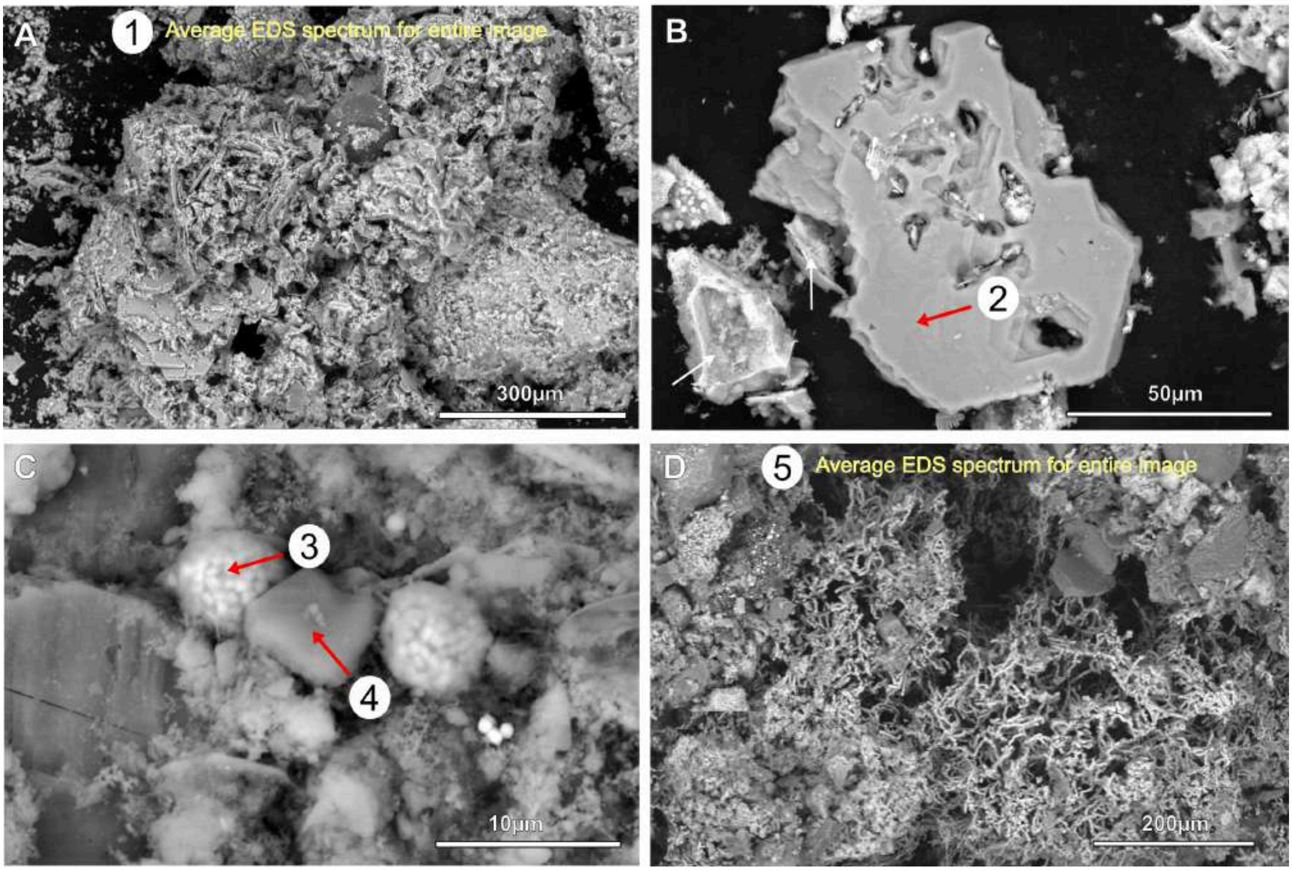

Phases (at%)	C	O	Na	Mg	Al	Si	S	K	Fe
1	28	65					1		5
2	27	65					1		6
3		66	1	1	2	4	14	1	12
4		61	1	1	10	17	1	3	6
5		66	1	1	2	7	8	1	13

Figure 40. SEM photomicrographs of sample ES-23-H8. Numbers indicate the location of the associated EDS spectra shown at the bottom of this figure. **(A)** Overview of sample area. The EDS analysis (number 1) represents the average of the entire image, mainly consisting of iron and oxide and to a lesser extent also sulfur. The carbon peak is mainly derived from the carbon stub upon which the sample was mounted and should therefore be disregarded in this spectrum. The analysis also shows traces of other elements linked to silicates (Si, Al, Ca), metals (Cu, Ni and Mn), as well as P. **(B)** Cavities formed on the surface of a platy iron-oxide-sulfur particle (Phase 2). Altered pearlite (white arrows) **(C)** Silicate particles (Phase 4) with framboidal pyrite (Phase 3). **(D)** Filaments encrusted by a Fe-S-bearing phase. The EDS analysis 5 represents the average of the entire image. Si is related to silicate particles embedded in the Fe-S-rich filamentous structures.

Sample ES-23-H9

Sample ES-23-H9 was recovered from the beam resting on the seafloor (beam side closest to the shipwreck) (Fig. 3). Four phases were identified from the XRD pattern (Fig. 41): (1) quartz (SiO_2, IDD reference 00-033-1161, (2) feldspar (as the calcium aluminum silicate phase, IDD reference 00-052-1344), (3) Mg-bearing calcite (Ca, Mg)CO_3, IDD reference 00-043-0697), and (4) halite (NaCl, IDD reference 00-005-0628). Although there are weak peaks suggesting the presence of an iron oxide, the XRD pattern precludes the clear determination of a specific phase.

SEM-EDS analyses show that the sample contains siliciclastic sediments, primarily composed of quartz and feldspar (Fig. 42B; Phase 2), sulfur-bearing iron oxides and corroded steel fragments having a pearlitic microstructure (Fig. 42D). Pearlite is a two-phased lamellar structure composed of alternating layers of ferrite (dark) and cementite (white), resulting in a characteristic zebra pattern (Figs. 42D). The sample also contains platy iron-oxides (with a small amount of sulfur), that are distributed throughout the sample (Fig. 42A,B,E). Small quantities of framboidal pyrite were also observed (Fig. 42F).

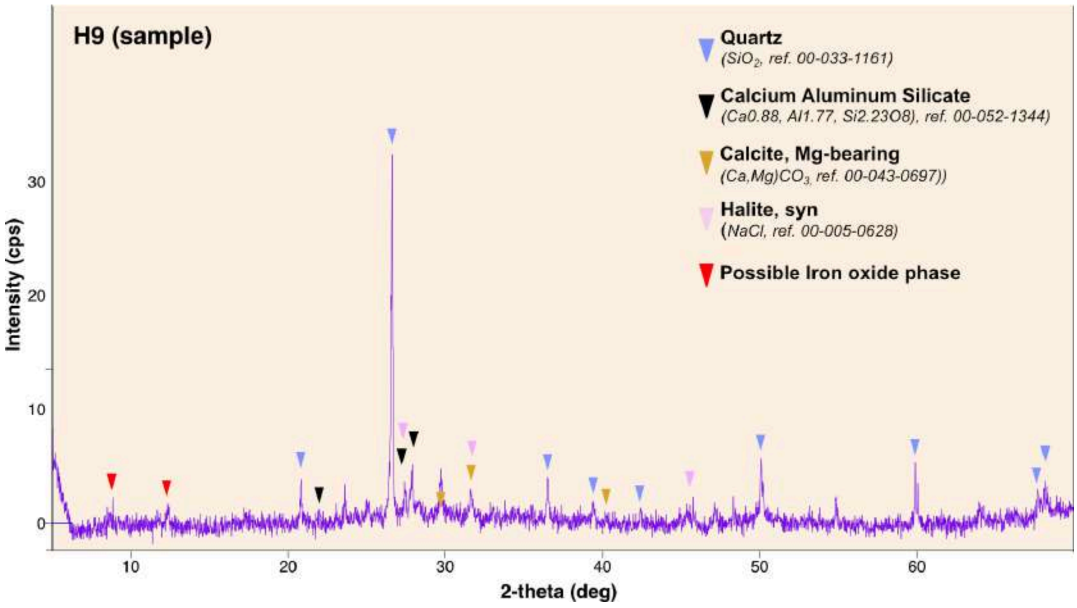

Pos.[°2θ]	Height (cts)	Rel. Int. [%]	Matched by	ICDD Ref
8.8638	41.75	3.36	Possible Iron oxides	
12.4074	56.77	4.57	Possible Iron oxides	
20.8579	127.07	10.23	Quartz	*00-033-1161*
26.6551	1242.08	100.00	Quartz	00-033-1161
27.4892	84.69	6.82	Calcium Aluminum Silicate Halite	00-052-1344 00-005-0628
27.9491	146.59	11.80	Calcium Aluminum Silicate	*00-052-1344*
29.7539	138.63	11.16	Mg-bearing Calcite	*00-013-0092*
31.7059	81.20	6.54	Halite Mg-bearing Calcite	*00-005-0628* *00-013-0092*
36.5588	141.32	11.38	Quartz	*00-033-1161*
39.4353	65.21	5.25	Quartz	*00-033-1161*
42.4510	63.62	5.12	Quartz	*00-033-1161*
45.6497	42.09	3.39	Halite	*00-005-0628*
50.1643	178.69	14.39	Quartz	*00-033-1161*
59.9409	197.36	15.89	Quartz	*00-033-1161*
67.7527	64.81	5.22	Quartz	*00-033-1161*

Figure 41. X-ray diffractogram of sample ES-23-H9 with diagnostic peaks and matching references in the ICDD PDF-4+ database.

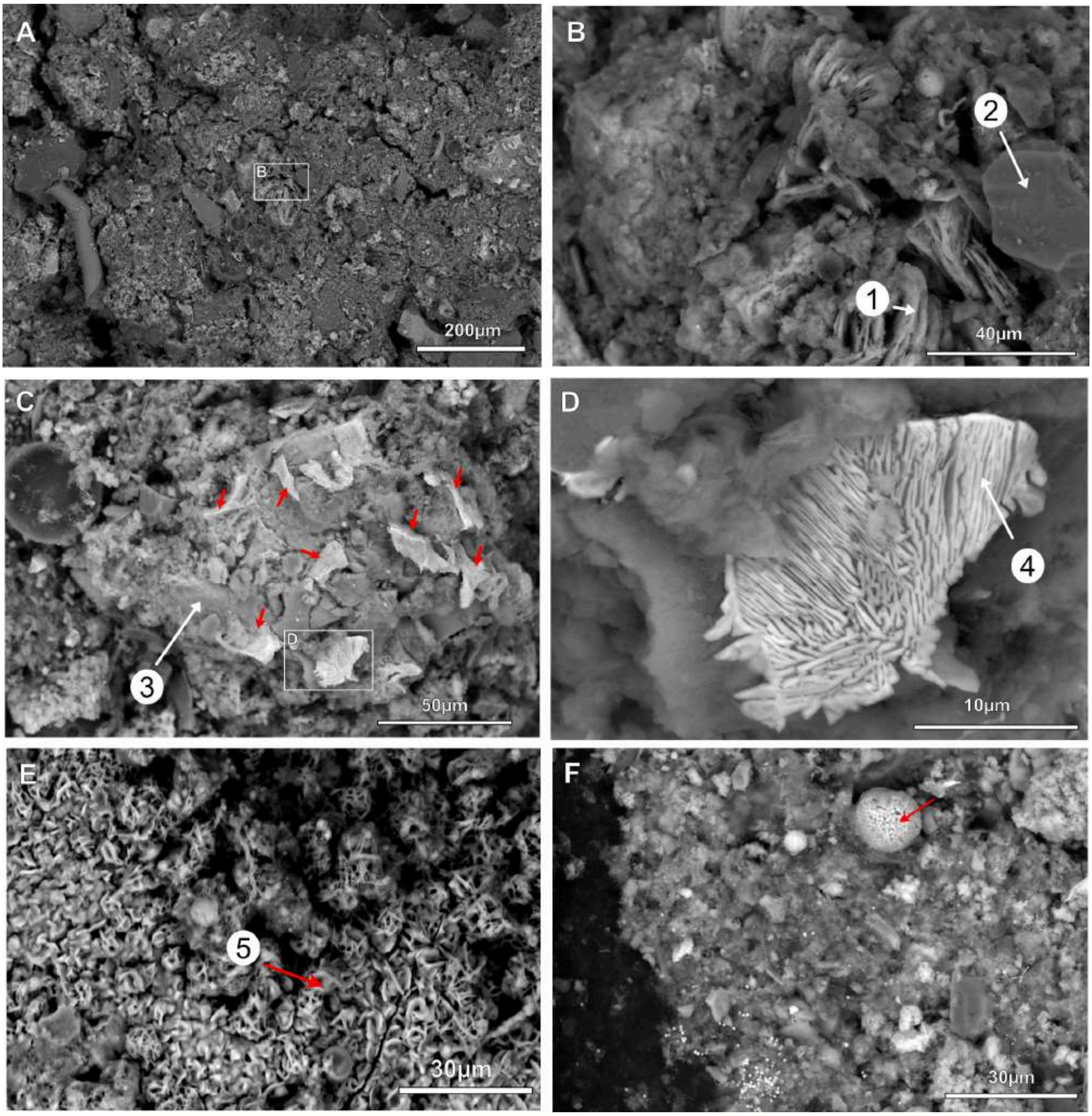

Phases (at%)	C	O	Na	Mg	Al	Si	S	Cl	Ca	Fe
1	14	61	1	1	1	3	2	1		15
2	10	66			1	20				2
3	17	61	1	1	1	4	1	1	1	11
4	16	60	1	1	1	3	1			17
5		58					2			20

Figure 42. SEM photomicrographs of sample ES-23-H9. Numbers indicate the location of the associated EDS spectra shown at the bottom of this figure. **(A)** Overview showing a mixture of silicates and iron-bearing sediments. **(B)** Detail of (A) The number 1 shows platy iron oxides with minor amounts of sulfur (the silica (Si) signal is likely coming from the surrounding matrix) and number 2 a euhedral quartz grain. **(C)** Section of the sample containing many steel fragments (brighter contrast, red arrows) embedded in an iron-oxide matrix (lower contrast) (Phase 3). The silica signal indicates the proximity of siliciclastic particles and a diatom is visible in the upper left corner. **D)** Detail of (C). Steel fragment, which has a pearlitic texture (phase 4). **(E)** Platy mineral containing iron (Fe) and oxygen (O) and traces of sulfur (S) (Phase 5). **(F)** Silicate sediment mixed with iron oxides and framboidal pyrite red arrow, identified with EDS mapping, not shown).

MICROBIAL COMMUNITY DIVERSITY

ALPHA DIVERSITY (WITHIN SAMPLE GROUPS)

Alpha diversity, which is a measure of species richness and evenness within a community, was quantified using the total number of Amplicon Sequence Variants (ASV – sequences differing from each other by a single nucleotide) and the Shannon diversity index (a statistical treatment in which a greater number indicates a more diverse and complex community). Here, communities are defined as sample groups having similar characteristics (reference sample, sediment signature, metal signature and steel beam deposits).

For the 16S rRNA V4 gene sequences, indicative of bacterial and archaeal diversity, results showed that the number of ASV across the samples varied substantially (samples ranging from 190 to 1344 observed ASV). Here, the number of ASV is used as an indirect proxy for number of species. Correspondingly, the Shannon diversity index ranged from 3.49 to 9, indicating not just a varied community composition among the different samples but also a considerable fluctuation in the evenness distribution of taxa across samples. Despite these diversity metrics, statistical analysis using the Kruskal-Wallis test did not reveal significant differences across sample groups ($p > 0.05$), likely due to the limited sample size with 1-6 samples per group, thus reducing the statistical power of the test.

Concerning the 18S rRNA V4 gene sequences, which target the eukaryotes, a more limited range of ASV (240 to 513) was observed compared to the 16S rRNA gene sequences. This is consistent with the generally lower diversity and abundance of eukaryotes compared to prokaryotes in these environments. Despite fewer ASV, the Shannon diversity index for the 18S rRNA gene sequences exhibited a narrower but consistently high range (4.15-6.38), reflecting a community that, while less rich in unique taxa, maintains an even distribution among existing eukaryotic species.

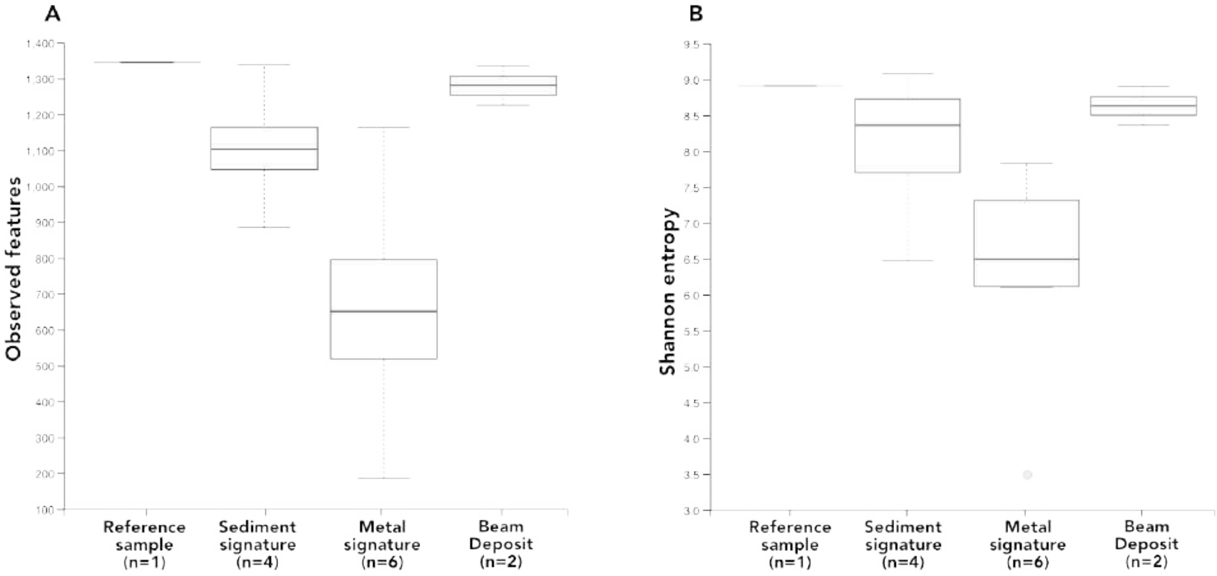

Figure 43. Boxplots showing bacterial and archaeal alpha diversity across groups based on sample characteristics: reference area, sediment signature, metal signature, and steel beam deposits. **(A)** Estimated richness calculated using an abundance-based coverage estimate (ACE) of observed ASV. **(B)** Shannon diversity of the hull samples on MS *Estonia*. The horizontal lines inside the boxes represent the median values, and the lower and upper ends of the boxes represent the first and third quartiles, respectively. Whiskers represent sample values outside the 50% mid-range. Squares outside the whiskers represent sample values > 1.5 times the height of the box.

The sediment samples were typically more species-rich compared to the metal group samples (group 3, Fig. 43A and 44A). The sediment sample group also had the highest Shannon diversity indicating a relatively even distribution of species. The comparatively low Shannon measure in the metal-rich samples (group 3) reflects the dominance of a smaller number of species (Fig. 43B and 44B). Both the sediment-rich samples and the metal-rich samples in group 3 showed the same diversity characteristics for both the prokaryotic and eukaryotic communities. In contrast, the beam samples had diverse and complex prokaryotic populations, but considerably fewer eukaryotic species (Fig. 43 and 44). The prokaryotic communities in the beam samples appear to have a sediment signature, i.e. high species richness and an even distribution of species. In contrast, the eukaryotic communities in these samples appear to have a metal signature, i.e. low species richness and few dominating species.

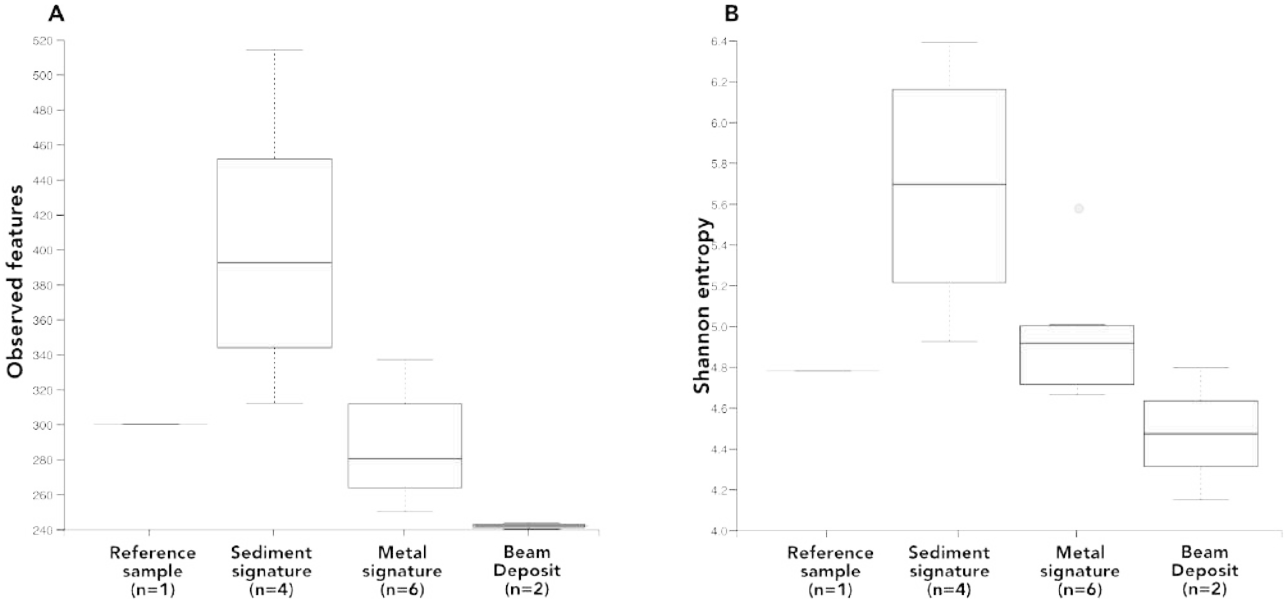

Figure 44: Box plots showing eukaryotic alpha diversity across groups based on sample characteristics: metal signature, sediment signature, steel from the beam and sample from reference area. (A) Estimated richness calculated using an abundance-based coverage estimate (ACE) of observed ASV. (B) Shannon diversity of the hull samples on MS *Estonia.* The horizontal lines inside the boxes represent the median values, and the lower and upper ends of the boxes represent the first and third quartiles, respectively. Whiskers represent sample values outside the 50% mid-range. Squares outside the whiskers represent sample values > 1.5 times the height of the box.

BETA DIVERSITY (BETWEEN SAMPLE GROUPS)

Beta diversity refers to the variation in species composition between different ecological communities, in the case of this investigation specifically, the change in diversity between groups from different sample characteristics (metal or sediment signature, samples from the beam). On a Principal coordinates Analysis (PcoA) plot, the overall spread of the data points provides an indication of the variability within and between the sample groups. Clusters of points suggest groups of samples with similar community structures, whereas dispersed points suggest higher diversity within a group. The proximity between points of different colors implies that the microbial communities from these specific locations share similarities. The typically scattered distribution of points suggests that there is substantial variability in microbial community composition within the same location, for both prokaryotic and eukaryotic communities. The absence of clearly distinct clusters suggests rather subtle variations between groups based on characteristics and/or that the variation in community composition between samples is not explained by sample characteristics. A low sample size can also prevent clear clustering. Given the high alpha-diversity for both 16S and 18S samples, the microbial communities might contain complex dynamics and interactions that result in a scattered distribution.

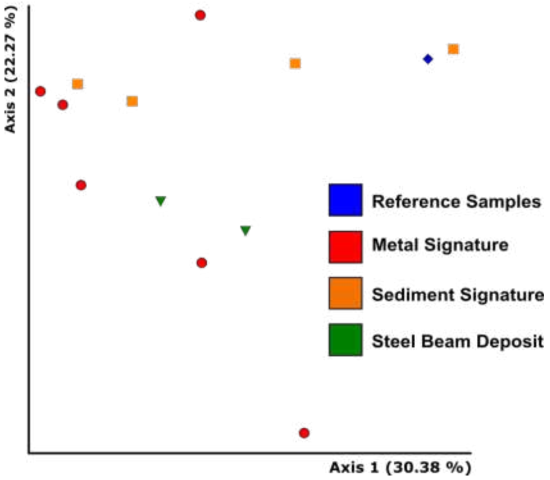

Figure 45. Principal components plot of bacterial and archaeal beta diversity (difference between sample groups: reference area, sediment signature, metal signature and beam deposits). Each point represents a sample in one of the four sample groups and weighted based on the abundance of taxa within the sample.

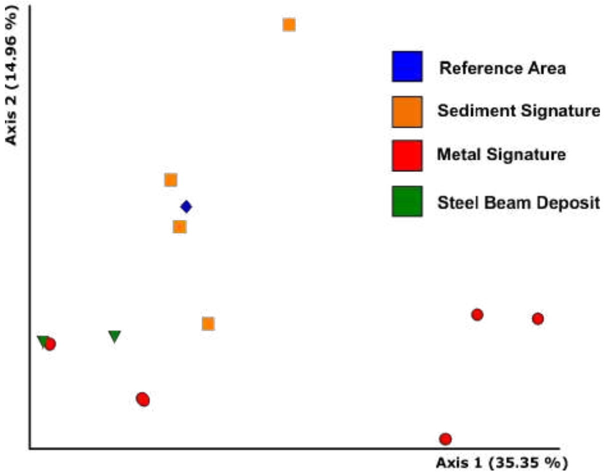

Figure 46. Principal components plot of eukaryotic beta diversity (difference between sample groups: reference area, sediment signature, metal signature and beam deposits). Each point represents a sample taken from one of the four sample groups weighted based on the abundance of taxa within the sample.

TAXONOMIC PROFILING OF PROKARYOTIC COMMUNITIES

Bacterial and archaeal communities were dominated by three major phyla: Proteobacteria, Desulfobacterota, and Campylobacterota (Fig. 47). Proteobacteria were mainly represented by members of the *Thiobacillus* genus, which contains species known for their role in the sulfur cycle. Some of these are chemolithoautotrophic sulfur oxidizers, using both organic and inorganic sulfur compounds such as sulfide, elemental sulfur, thiosulfate, sulfite, dimethyl sulfide, methanethiol, and ethanethiol as electron donors for metabolic energy requirements. They are typically found in environments where sulfur compounds are abundant, such as marine habitats (Hutt et al, 2017). Xanthomonadaceae are known for plant-pathogenic interactions, but have also been associated with deep-sea sediments (Fan et al., 2014) and deep-sea invertebrates (Romanenko et al., 2008). Some species reduce nitrite (Finkmann et al., 2000). Thiomicrospiraceae are predominantly found in marine environments and are known for their sulfur-oxidizing capabilities at low oxygen and/or anoxic concentrations (Timmer-ten Hoorn, 1975), sometimes in a symbiotic relationship with invertebrates (Osvatic et al., 2023). The second most represented phylum was Desulfobacterota, which primarily consists of anaerobic sulfate reducers (Murphy et al., 2021). *Desulfoconvexum*, *Desulfotalea*, *Desulfomicrobium*, and *Desulfopila* are sulfate reducers common in the marine environment, including cold sediments (Könneke et al., 2013). The most abundant taxa in sample H13 (a sample scraped from the cut-out metal piece) was *Desulfoconvexum*, a psychrophile, a group of strictly anaerobic sulfate-reducing bacteria (Kuever, 2014). The other most abundant Desulfobacterota - *Desulfonatronum* - are known for their preference for high salinity, anoxic and alkaline conditions (Zakharyuk et al., 2015), notably soda lakes, and grow by inorganic fermentation of sulfur compounds. However, some species have been isolated at moderate (i.e., seawater) salinity (Sorokin et al., 2011; Zakharyuk et al., 2015) and seawater pH values (Perez-Bernal et al., 2017). The third most abundant phylum, Campylobacterota, represented by the *Sulfurimonas* and *Sulfurovum* genera, are primarily known for their sulfur-oxidizing capabilities, like the Proteobacteria *Thiomicrospiracea family* and *Thiobacillus genus*. Many are chemolithoautotrophs that couple their metabolic redox reactions to carbon fixation for biomass production, allowing them to thrive in environments with limited organic nutrients (Han and Perner, 2015; Li et al., 2023).

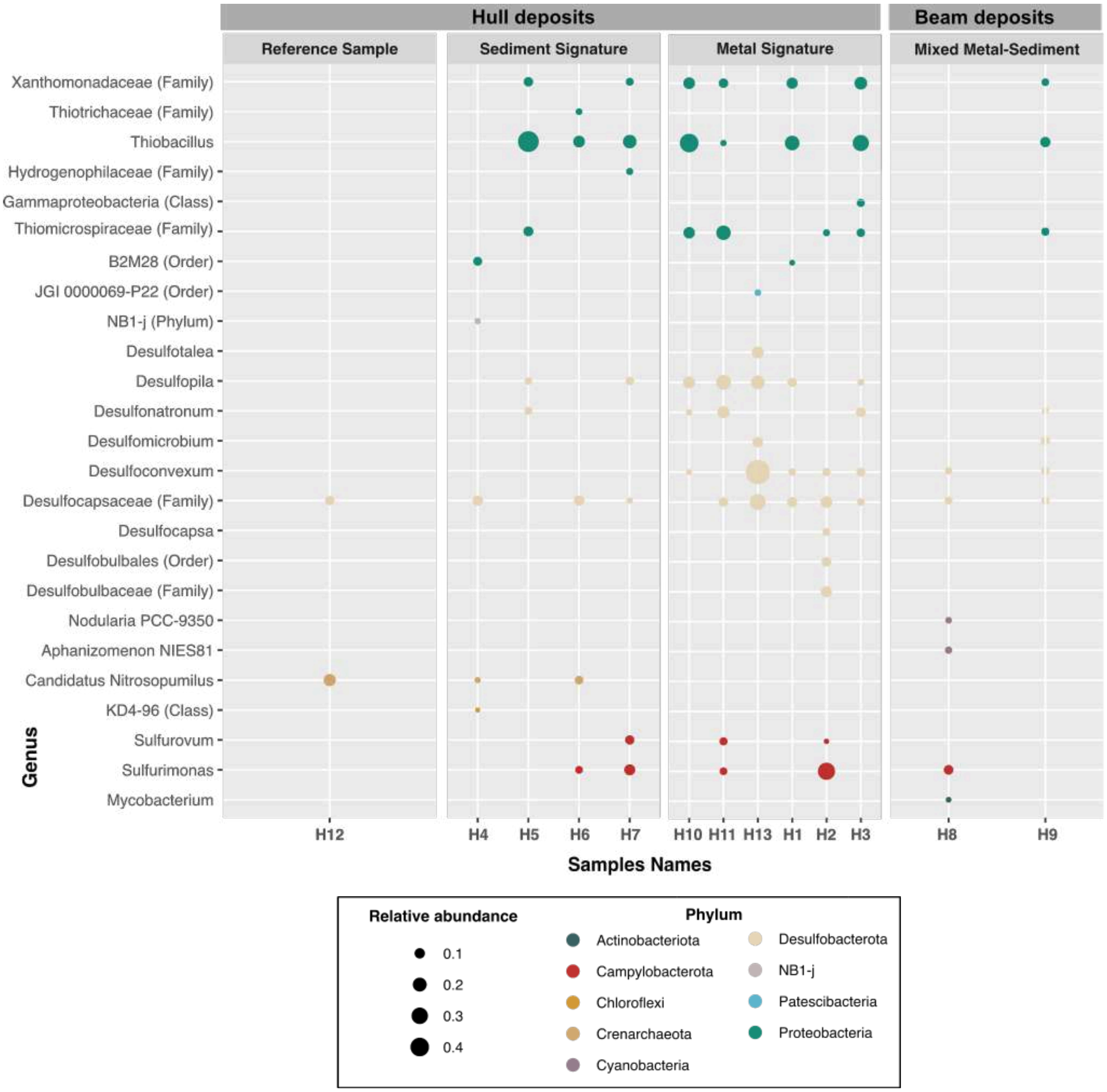

Figure 47: Microbial community composition based on 16S rRNA gene analyses. Taxonomic assignment is made at genus level or higher (in the latter case the taxonomic level is written in parenthesis). The size of the bubbles represents the relative abundances (%) of each taxonomic group. Only groups that represent more than 3% of the overall community is shown in this figure. Samples are grouped into their respective sample characteristics: metal signature, sediment signature, steel from the beam and sample from reference area.

TAXONOMIC PROFILING OF EUKARYOTIC COMMUNITIES

Eukaryotic communities are mainly represented by protists and metazoans. Among the protists, Dinoflagellates are a wide group of bloom-forming organisms in the marine environment that include the Peridiniales, a lineage that consists of mainly photosynthetic and heterotrophic species. Representatives from peridiniales mainly occur in the lower sampling area close to the sea bottom, and are known to thrive in the Baltic Sea (Paul et al., 2023). G*yrodinium* species are 'naked' (unarmored) dinoflagellates (Jang et al., 2019), often associated with red or yellow tides that feed on diatoms (such as *Chaetoceros debilis*) and frequently observed for decades in the Baltic Sea (Lindahl and Hernrot 1983; Suikkanen et al., 2011). Some metazoan, such as roundworms, e.g., *Halomonhystera* and *Desmolaimus*, are abundant in samples H2 and H4, respectively. These nematodes are commonly found parasitic organisms in grey seals ad harbor porpoises in the Baltic Sea (Gabel et al., 2021). Members of the *Halomonhystera* are tolerant to high concentrations of iron (Soltwedel et al., 2023). The *Chromadorita* genus, abundant in the reference area, are free-living nematodes and, members of this order (Chromadorina) have been linked to artificial substrates such as ship hulls (Ledu, 2020).

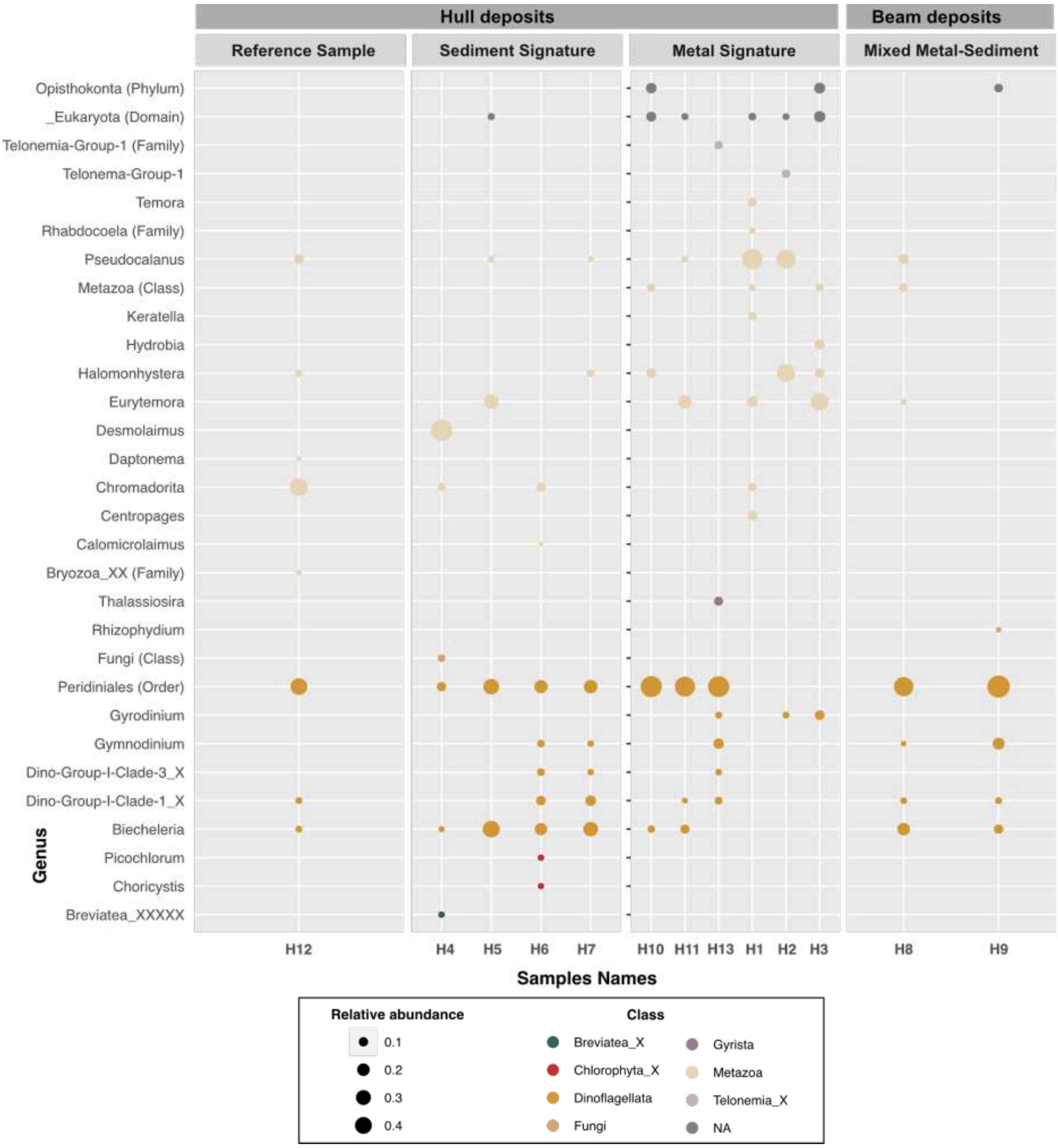

Figure 48. Eukaryotic community composition based on 18S rRNA gene analyses. Taxonomic assignment is made at genus level or higher (in the latter case the taxonomic level is written in parenthesis). The size of the bubbles represents the relative abundances (%) of each taxonomic group. Only groups that represent more than 3% of the overall community is shown in this figure. Samples are grouped into their respective sample characteristics: metal signature, sediment signature, steel from the beam and sample from reference area.

DATA SUMMARY AND INTERPRETATION

SOURCES OF SAMPLE COMPONENTS

The objective of the conducted analyses was to identify the sources of the components found in the analyzed material. This study has found that these components can be attributed to three known sources: the steel hull and its corrosion products, chemical components contained in the Baltic Sea water, and the particles supplied from the surrounding bedrock and sediments. The samples were divided into four groups, each reflecting the source that most significantly influences their composition. While other sources may also impact them, their effect is comparatively minor. **Group 1** includes reference samples, which are used as a baseline for comparison with other samples. **Group 2** samples contain mostly sediment that are transported from the surroundings. **Group 3** samples are mainly composed of iron-rich phases that form *in situ* and incorporate chemical elements from the steel hull and Baltic Sea water. These samples also include fragments of steel (pearlite) and traces of what likely is the hull coating (paint). **Group 4** samples originate from the beam resting on the seafloor and contain interspersed metals and sediments. Siliciclastic sediments are included in most samples, likely due to initial contact with the adjacent sea bottom bedrock and sediment, and subsequent dynamics that have resuspended and brought sediment into contact with the ship hull. Samples from both the sediment and metal groups contained substantial amounts of carbonates and occasional particles of gypsum and halite.

The map illustrated in Figure 49 provides an overview of the findings in this study. It shows the four sample groups and their spatial relationship with the fracture zone. The following text provides a brief summary of the main features of each group.

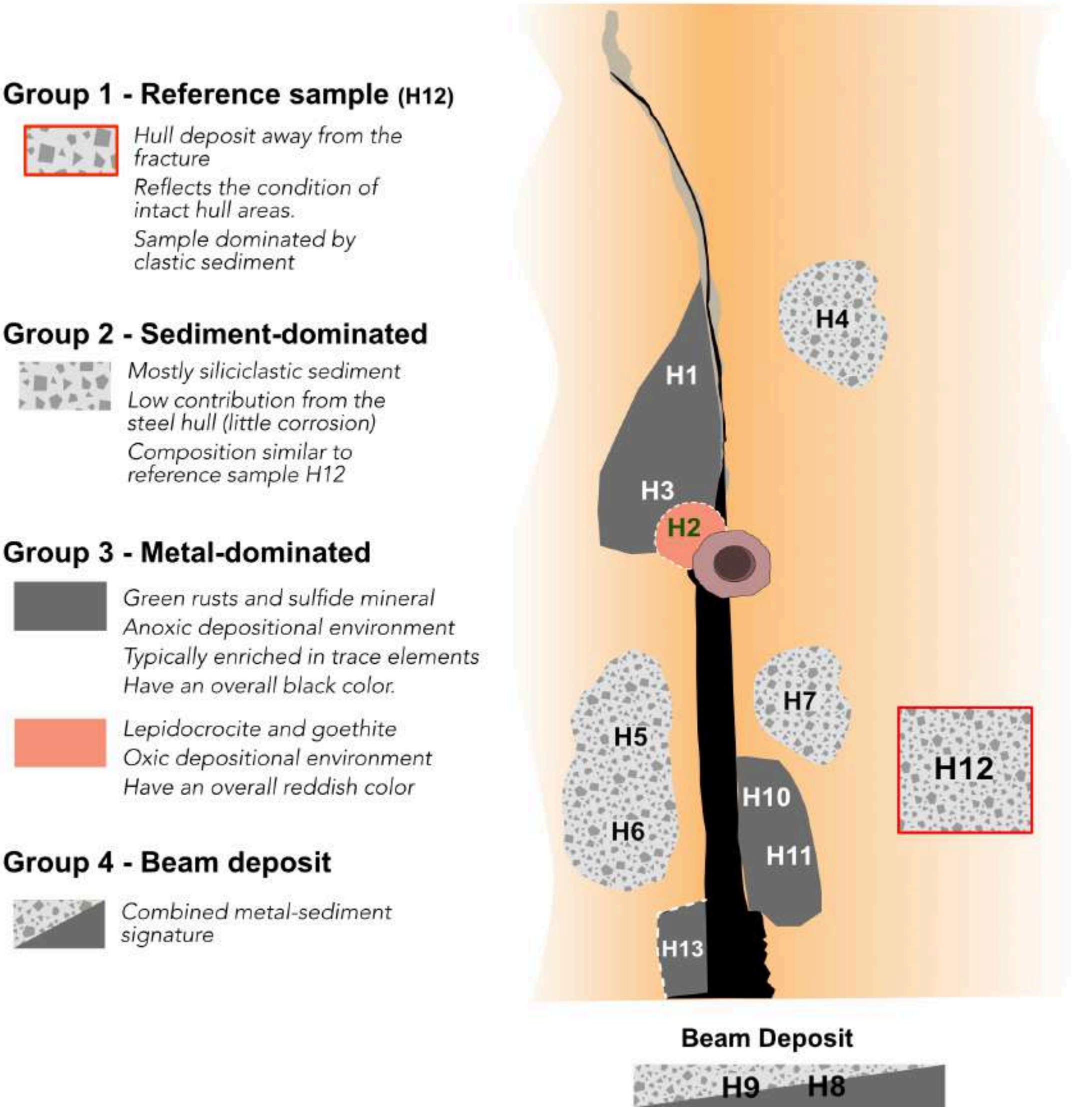

Figure 49. Map of sample groups having similar characteristics See text for details.

REFERENCE SAMPLES (GROUP 1)

STEEL FROM THE HULL

The steel hull is the source of iron as well as trace elements (Mn, Ni, Co, Cu, Cr) found in the samples. The numerous manganese sulfide (MnS) inclusions observed in the steel samples (Fig. 8) are likely impurities resulting from the addition of manganese (Mn) and sulfur (S) during steel production. Manganese is commonly added to a steel melt to remove oxygen, which can make the steel brittle (Cai et al., 2016). Sulfur is added to improve machinability, delaying grain growth and facilitating the formation of intragranular ferrite (Lu et al., 2018). The combination of Mn and S would lead to the formation of MnS impurities within the steel.

NON-FRACTURED HULL SURFACE DEPOSITS

Sample ES-23-12, away from the damaged steel, likely reflects the condition of intact hull areas. It predominantly consists of clastic particles such as quartz and aluminosilicates. Corrosion products such as green rust (GR) and carbonates were not observed, which can probably be attributed to the protective layer of paint on the steel surface. Sparsely distributed framboidal pyrite (FeS_2) was detected (Fig. 10C, D). Although framboids can be synthesized abiotically in the laboratory (Ohfuji and Rickard, 2005), the origin of the sulfur in modern marine framboids is essentially biogenic through the activity of sulfate-reducing bacteria (SRB) (Sawlowicz, 2000). The sample has a high organic carbon content, likely from organisms residing on the hull. Molecular analysis shows a low SRB abundance and no sulfide-oxidizing bacteria, suggesting a restricted sulfur cycle.

SEDIMENT-DOMINATED SAMPLES (GROUP 2)

The samples belonging to Group 2 consist primarily of siliciclastic sediment and only sporadic iron-bearing minerals. The low iron concentration in these samples suggests that the contribution from the steel hull is minimal. Siliciclastic sediments came initially from contact with the adjacent bedrock and sediment of the sea bottom. Over three decades, subsequent sedimentary dynamics such as strong bottom currents, gravity flows, and variation in thermohaline circulation, may have resuspended sediment, bringing it into contact with the ship hull. The composition of these samples is similar to sample H12, which was collected away from the damaged steel and likely reflects the condition of the intact hull. The siliciclastic materials are also associated with various diatoms, a group of single-celled algae enclosed in siliceous cell walls. Although diatoms generally perform photosynthesis, some can live in the absence of light (Armstrong et al., 2000) or even stay dormant for long periods of time in a light-depleted environment, switching to anaerobic respiration (Merz et al., 2021). Some diatoms may already be dead and transported as sediment to the site. Sample H7 and H6 also contain a few discrete baryte particles, a common mineral in Baltic Sea sediment (e.g., Bernard and Van Grieken, 1989). Riverine input of continental weathering material transports dissolved barium into the Baltic Sea. Plankton or other organisms incorporate Ba into their biomass, and when these organisms die, the Ba is released and can react with sulfate to form barite. In turn, SRB are capable of remobilizing barite during their respiration (Karnachuk et al., 2002)

METAL-DOMINATED HULL SAMPLES (GROUP 3) AND BEAM DEPOSITS (GROUP 4)

MS *Estonia* is a steel-hulled ship, and the metal-dominated samples (Group 3 and 4) mainly reflect the steel composition and its corrosion products, as well as ions from the Baltic Sea water, e.g., sulfate (SO_4^{2-}), sulfides (HS^-), carbonates (CO_3^{2-}), calcium (Ca^{2+}), and magnesium (Mg^{2+}). The contribution of seawater to the corroded steel's composition is evident in sample S3B, which was obtained by scraping oxidized rust from a steel plate in the lab. This rust sample shows minimal sediment contribution (using Al as a non-seawater/non-hull marker) and high levels of Na, K, Mg, and Ca (see Fig. 6a), similar to Baltic Sea water. This indicates seawater salts' influence, probably due to air drying.

Iron-rich phases formed in place are abundant in all the samples. The high iron concentrations coincide with elevated sulfur levels. Although the initial steel composition lacks sulfur (table 6a), its subsequent degradation results in the incorporation of various amounts of sulfur from the Baltic Sea water into the newly formed iron phases. These iron-rich phases include iron-oxides (lepidocrocite, goethite), layered iron hydroxides (green rust), and iron-sulfides (FeS_2 and FeS). The three types of green rusts detected by XRD in this study - Green Rust (GR), Green rust I (GRI), and Green Rust-SO_4 (GR-SO_4; Iron sulfate hydroxide hydrate) - reflect variation in Fe^{2+} and Fe^{3+} incorporation within the hydroxide layers and the presence of water or other ions (e.g., SO_4^{2-}) in between these layers. Green rust represents an early-stage (intermediate) corrosion product indicative of environments with restricted oxygen availability. In contrast, the formation of lepidocrocite (γ-FeOOH) and goethite (α-FeOOH) occurs in oxygen-rich conditions, as these iron(III) oxides need a higher oxidation state of iron, signifying a more advanced stage of corrosion (see below 'Assessment of processes'). Many metal-dominated samples show the presence of iron-enriched calcium carbonates. These carbonate deposits are a secondary product of the rusting process, commonly linked with the corrosion of steel in marine environments (see Annex I). Sample S1B offers an insight into the early steel corrosion process, closely resembling the pristine steel sample (S2B), yet showing selective iron removal and slight trace element enrichment due to corrosion (refer to 'Trace Element Enrichment' section). Sample H8 and H9, which are beam deposits, have a combined metal and sediment signature with a similar diffraction pattern as the sediment-rich samples H6 and H7, but with the presence of Fe-bearing phases.

Two of the metal-dominated samples (H10 and H13) and both beam deposits (H8 and H9) contain steel fragments having a pearlitic microstructure (a two-phased lamellar structure composed of alternating layers of ferrite and cementite). Since these fragments were found in both hull deposits and beam precipitates (H8 and H9), it is likely that both the hull of MS *Estonia* and the beam are constructed of a similar steel type. In sample H13, micrometer-sized particles of what is likely paint were detected.

TRACE ELEMENT ENRICHMENT

The samples that were investigated contain a range of trace elements (Table. 6a and 6b), such as Mn, Ni, Co, Cu, Cr, Ga, V, and As. These elements predominantly originate from the steel hull. During the MS *Estonia* corrosion process, iron may be selectively leached due to its higher reactivity and susceptibility to oxidation when exposed to water and oxygen, leaving behind these trace elements enriched in rust. This selective process is exacerbated by corrosive agents like the Baltic Sea saltwater and sulfides produced by sulfate-reducing bacteria. Moreover, the elevated trace element levels, particularly evident in samples S3B, H13, and H3, may also attributed to the incorporation of hull paint residues, which is likely a significant secondary source of trace elements, due to its high pigment content. For instance, sample H13 contains paint particles highly enriched with Co, Cu, and Sn (Fig. 38E, Phase 4). Furthermore, the identified microbial communities within the corrosion layers on the MS *Estonia* hull can sequester substantial quantities of positively charged elements, including trace elements, within their extracellular organic matrices (see Annex I). These factors collectively contribute to the observed heterogeneity in trace element distribution across the MS *Estonia* samples.

ASSESSMENT OF PROCESSES AND FORMATION

This section provides a summary of the natural processes assessed to have contributed to the material deposition on the hull of the MS *Estonia* shipwreck, in association to the front hole on the starboard side. Details are provided in ***Annex 1***.

Green rust (GR) is a dominant phase in the MS *Estonia* corrosion product. It is recognized in the literature as an important transitional phase in the corrosion process, where it forms an unstable mixture of ferrous and ferric hydroxides (Gomes et al., 2009). Given that the MS *Estonia* has been submerged in seawater for three decades, the dark corrosion products suggest that the environmental conditions have not permitted the formation of iron phases with a higher degree of oxidation, with the corrosion layer mainly comprising Green Rust and iron sulfides and iron-rich calcium carbonates. The text below explains the formation of those phases in the context of the MS *Estonia*.

CORROSION PRODUCT LAYER

The MS *Estonia* was constructed using coated steel for corrosion protection. The damage inflicted to the hull at the fractured area tore up and removed this coating, leaving the unprotected steel exposed to the seawater for almost 30 years. Figure 50 is a cartoon of the corrosion products that form when steel is exposed to seawater for a prolonged period of time is exposed to seawater for a prolonged period of time (details see annex I). Corrosion is a natural process involving the gradual destruction of the original steel surface by complex biological and physicochemical processes that convert metallic iron into iron oxides, hydroxides, and/or sulfides (Melchers, 2006).

A corrosion product layer (CPL; Refait et al., 2020) develops at the surface of the seawater-exposed steel in as little as a few months, forming three principal strata that vary in composition as a function of the absence or presence of oxygen (oxic vs. anoxic; Fig. 50): (1) a biofouling zone composed of macroscopic encrusting eukaryotes, shells, and sediment (oxic environment), (2) an outer stratum mainly composed of orange-brown Fe(III)-oxyhydroxides (lepidocrocite and goethite; Sample H2), and (3) a black inner stratum directly in contact with the steel and typically composed of Fe^{2+}-rich or a mixture of Fe^{2+} and Fe^{3+} corrosion products (e.g., green rust (GR) and iron sulfides).

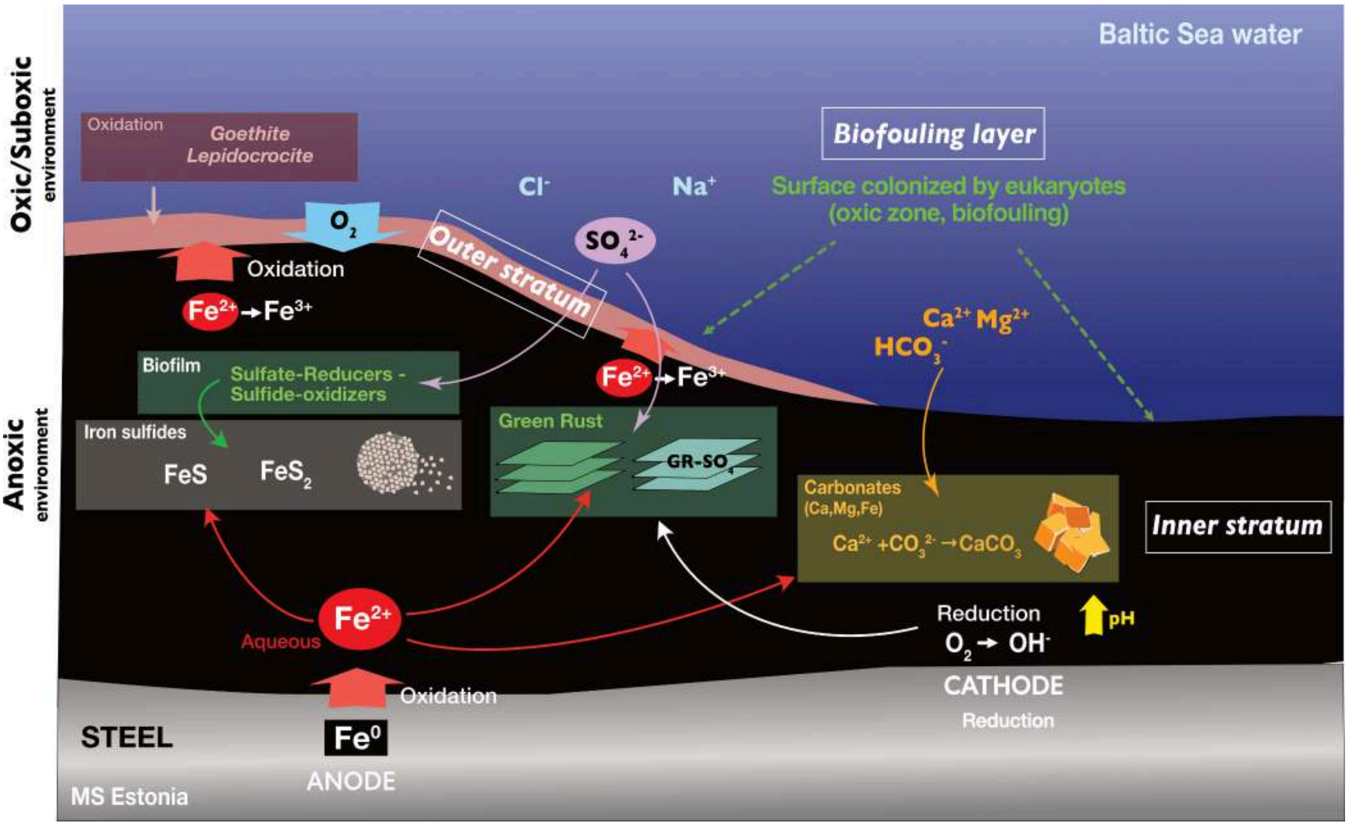

Fig. 50. **Corrosion of steel in Baltic Sea water -MS *Estonia* Model.** This model represents a dynamic interplay of chemical and biological processes contributing to the corrosion system (for an extended version of this model which details chemical reactions, see Annex I)

Sample groups 3 and 4 that have a metal signature, primarily consist of corrosion products such as GR and sulfide that form in the inner, oxygen-limited stratum. Only one of these samples (H2) shows more oxidized phases consistent with the outer oxic layer (Fe^{3+} hydroxides). In marine environments, the black inner stratum tends to increase in thickness with time (over years) compared to the outer, more oxidized layer. This creates an anoxic environment (without oxygen) in which anaerobe microorganisms (living without oxygen) thrive (see below). Oxygen cannot reach the inner part of the CPL because organisms living in the biofouling layer and in the orange-brown outer layer are consuming it (Refait et al., 2020). The production of iron hydroxides at the steel surface is explained by the steel-water couple, functioning like a battery, with the metallic iron (Fe^0) being oxidized into Fe^{2+} at the anode side, O$_2$, and H$_2$O being reduced to OH$^-$ at the cathode side (Eq. 1 and 2; Fig. 50). Fe^{2+} and OH$^-$ can combine to a solid Fe(II)-hydroxide phase forming one of the first corrosion products of the inner layer (Eq. 3).

$$\text{(oxidation) } Fe^0_{(s)} \rightarrow Fe^{2+}_{(aq)} + 2e^- \qquad (1)$$

$$\text{(reduction) } \tfrac{1}{2}O_{2(g)} + H_2O_{(l)} + 2e^- \rightarrow 2OH^-_{(aq)} \qquad (2)$$

$$Fe^{2+}_{(aq)} + 2OH^-_{(aq)} \rightarrow Fe(OH)_{2(s)} \qquad (3)$$

This inner, anoxic black layer allows anaerobic bacteria (independent of O$_2$) to thrive (e.g., sulfate-reducing bacteria). These microbial communities are organized into biofilms, and complex geomicrobiological interactions take place within the inner and outer strata, leading to the formation of new phases such as sulfide minerals, e.g., pyrite (see below and annex I). These communities are embedded in extracellular polymeric substances (EPS), which act as diffusion barriers that allow for a wide range of metabolic activities to coexist (Dupraz et al., 2009; Visscher and Stolz, 2005; Megonigal et al., 2003). The protective effect of EPS combined with highly diverse metabolisms strongly improves the tolerance of those communities to environmental stressors, explaining that we find microbial mats and biofilms in extreme environments (Gallagher et al., 2011), rust being one of them.

Only sample H_2 contains fully oxidized phases of iron corrosion, such as goethite α-FeOOH and lepidocrocite γ-FeOOH, which can form from the oxidation of Fe^{2+} within GR. GR is a known transition phase toward more oxic minerals (Gomes et al., 2009). In anoxic bottom seawater, the outer layer may not form, and the whole corrosion layer thus remains black. In the case of MS *Estonia*, the oxygen level in the environment surrounding the investigated hull area has fluctuated with time, leading to overall dysoxic conditions, which could enhance the development of the black anoxic inner layer.

FORMATION OF CORROSION PRODUCTS

Green Rust (GR)

Corrosion products depend largely on environmental conditions and the type of microbial community present. In the MS *Estonia* system, the metal signature samples (H1, H2, H3, H10, H11, H13) are dominated by the presence of intermediate corrosion products forming layered, double iron hydroxide minerals Green Rust (GR; see Annex I). GR comprises mostly Fe^{2+} cations and hydroxide anions but can include Fe^{3+} and also incorporate compounds found in the surroundings (e.g., sulfates, chlorines, or carbonates from seawater). The composition of green rust (GR) and thus its diagnostic XRD pattern can vary significantly as a function of the ions (SO_4^{2-}, $CO_3^{2-,}$) trapped in between layers and the degree of Fe^{3+} incorporation within the iron-hydroxide layer. In the investigated samples, X-ray diffraction (XRD) studies revealed the existence of an iron sulfate hydroxide hydrate phase. Despite not being designated as GR(SO4) in the ICDD PDF-4+ database, the empirical formula corresponds to that of GR(SO4).

Carbonates

Calcium carbonates are present, even abundant, in many of the examined samples. The production of hydroxide ions (OH^-) on the cathode side increases local pH. Marine water is naturally rich in bicarbonate (HCO_3^-) and calcium (Ca^{2+}). In the presence of OH^-, bicarbonate forms carbonate ions (CO_3^-) that will combine with calcium and precipitate calcium carbonate ($CaCO_3$) (Möller et al., 2006). During this precipitation process, iron (Fe^{2+}) and magnesium (Mg^{2+}), present in seawater, can be incorporated into the calcium carbonates. This may explain the widespread distribution of iron-rich carbonates in the observed corrosion deposits.

Iron sulfides

Many of the samples contain iron sulfides, typically as framboidal pyrite (FeS_2). Framboidal pyrites can be synthesized in the laboratory without the presence of microbes (Ohfuji and Rickard, 2005). However, in marine environments, the source of the sulfides is predominantly biogenic, produced by sulfate-reducing bacteria. These anaerobe organisms respire sulfate instead of oxygen, releasing sulfides. Iron (Fe^{2+}) is derived from steel corrosion (eq. 1). This indicates a microbiological origin of iron sulfide deposits observed in these samples (Sawlowicz, 2000). Within the less oxygenated inner layers, anaerobic microbes thrive, especially sulfur cycle organisms as sulfate is present in large amount in seawater. Sulfate-reducing bacteria (SRB) convert sulfate to sulfide, which in turn reacts chemically with Fe^{2+} to form iron sulfides (FeS, FeS_2 - pyrite). Sulfate reducing activity can be supported by H_2 produced during water reduction (Annex I). This reaction releases OH^- ions, increasing pH that further favors precipitation of carbonate minerals (Dupraz et al., 2009). Some dissolved sulfides may diffuse through the inner layer and can be recycled by sulfide-oxidizing bacteria (e.g., *Thiomicrospira*) that depend on nitrate or low concentrations of oxygen for this, converting this sulfide into sulfate (SO_4^{2-}), “elemental” sulfur (S^0) completing the sulfur cycle.

Fe(III) hydroxides (lepidocrocite, goethite)

Fe(II)-phases (GR, iron sulfides) situated at the surface of this inner layer and in contact with the surrounding oxygenated water may be further oxidized into Fe(III)-phases that form the orange outer layer (e.g. lepidocrocite and goethite), observed in sample ES-23-H2.

CONCLUSIONS

- The objective of the investigation was to identify the sources of the components found in the analyzed material. The sampling included 11 samples from locations close to the hull fracture, 2 from a beam resting on the seafloor, and 3 samples from the steel hull. The samples were analyzed for element content (ICP-MS, GC-IRMS), mineralogy and particle morphology (XRD, SEM-EDS), and microbial community composition (DNA extraction, rRNA gene sequencing).
- The report concludes that the material deposits associated with the front hole on the starboard side of the MS *Estonia* are the result of natural processes, such as biofouling, sediment accumulation, and marine corrosion of exposed steel.
- All detected and identified components in the samples can be traced back to the following known sources:
    - The steel hull, its corrosion products, and paint pigments.
    - The siliciclastic sediment surrounding the shipwreck, on the sea floor as well as suspended in the sea water.
    - The Baltic Sea water containing dissolved elements.
    - Microorganisms colonizing the hull and its corrosion products.
- The contribution of each of these sources to the analyzed samples was evaluated, resulting in their classification into four groups based on the dominant contributing sources:
    - Group 1 includes reference samples: 'Pristine' uncorroded polished steel (sample S2B) and a hull surface deposit sample taken away from the fracture (sample ES-23-H12), which represents the intact hull surface for comparison.
    - Group 2 contains hull deposits predominantly consisting of clastic sediment supplied from the surrounding bedrock and sediments (samples ES-23-H4,- H5,- H6,- H7). These samples have a similar composition to the reference non-fractured hull surface sample ES-23-H12.
    - Group 3 contains hull deposits mainly composed of iron-rich phases, formed in situ and associated with corrosion processes. (samples ES-23-H1, -H2, -H3, -H10, -H11, -H13, S1B, S3B).
    - Group 4 contains surface deposits collected from a beam resting on the sea floor, having a combined sedimentary and metal signature. (samples ES-23-H8, -H9).
- A rational interpretation is that the damage inflicted to the hull at the fractured area caused substantial tearing of the steel. The anti-corrosion coating on the hull was compromised, leading to direct exposure of the steel to corrosive seawater.conditions
- The MS *Estonia* corrosion products form three principal layers that vary in composition, mainly as a function of the absence or presence of oxygen. The observed corrosion products are mainly composed of black Fe(II)- rich or a mixture of Fe(II) and Fe(III) minerals (i.e., various types of green rust (GR) and iron sulfides) developing in an oxygen-depleted environment.
- The widespread presence of iron-containing carbonates in the samples is a known byproduct of the corrosion process that often occurs in marine environments.
- Sample S3B (oxidized rust scraped from the steel plate in the laboratory) presents elevated levels of Na, K, Mg, and Ca, which do not originate from the sediment itself and are probably attributable to the evaporation of Baltic Sea water (drying artifact during sample processing .
- Microbial communities, particularly those involved in the sulfur cycle, play a significant role in the MS *Estonia* corrosion processes. They affect the rate and nature of rust through their metabolic processes in both oxygen-rich and oxygen-depleted environments.
- Metal-rich samples are significantly enriched in trace elements (Ni, Co, Cu, Cr, Ga, V, and As), primarily traced back to the original steel hull. The observed variations in the concentrations of these elements across the samples are largely due to the selective leaching of iron during the corrosion process (possibly further facilitated by microbes, e.g., sulfate-reducing bacteria).
- Paint fragments (pigments) incorporated in the corrosion products are likely a significant contributor of trace elements.

REFERENCES

Armstrong, E., Rogerson, A., Leftley, JW. (2000). Utilisation of seaweed carbon by three surface-associated heterotrophic protists, Stereomyxa ramose, Nitzschia alba and Labyrinthula sp. *Aquatic Microbial Ecology* 21, 49-57.

Babraham Bioinformatics - FastQC A Quality Control tool for High Throughput Sequence Data. Retrieved from: https://www.bioinformatics.babraham.ac.uk/projects/fastqc/ (accessed January, 2024).

Bernard, P.C. and Van Grieken, R.E. (1989). Geochemistry of Suspended Matter from the Baltic Sea. 1. Results of Individual Particle Characterization by Automated Electron Microprobe. *Marine Chemistry,* 26 (1989) 155-177.

Boden, R. (2017). Editorial: 115 years of sulfur microbiology. *FEMS microbiology letters* 364, fnx043.

Bolyen, E., Rideout, J.R., Dillon, M.R., Bokulich, N.A., Abnet, C.C., Al-Ghalith, G.A., Alexander, H., Alm, E.J., Arumugam, M., Asnicar, F. (2019). Reproducible, interactive, scalable and extensible microbiome data science using QIIME 2. *Nature biotechnology* 37, 852–857.

Braissant O., Decho A.W., Dupraz C., Glunk C., Przekop K.M., Visscher P.T. (2007). Exopolymeric substances of sulfate-reducing bacteria: interactions with calcium at alkaline pH and implication for formation of carbonate minerals. *Geobiology* 5:401–11

Callahan, B.J., McMurdie, P.J., Rosen, M.J., Han, A.W., Johnson, A.J.A., and Holmes, S.P. (2016). DADA2: High-resolution sample inference from Illumina amplicon data. Nat Methods 13, 581–583.

Cai, X., Bao, Y., Lin, L., and Gu., C. (2016). Effect of Al Content on the Evolution of Non-Metallic Inclusions in Si–Mn Deoxidized Steel.*Ssteel research int*., 87, 1168-1178.

Dupraz, C., Visscher, P.T. (2005). Microbial lithification in marine stromatolites and hypersaline mats. *Trends in Microbiology* 13, 429-438.

Dupraz C., Reid R.P., Braissant O., Decho A.W., Norman R.S., and Visscher P.T. (2009). Processes of carbonate precipitation in modern microbial mats. *Earth-Sci. Rev.* 96, 141–62

Estonian Safety Investigation Bureau. (2023). Intermediate report of the preliminary assessment of MV Estonia. Tallinn. Retrieved from: https://www.havkom.se/assets/reports/Intermediate-Report-MV-ESTONIA-Jan-2023.pdf (accessed January, 2024).

Fan, X., Yu, T., Li, Z., and Zhang, X.H. (2014). Luteimonas abyssi sp. nov., isolated from deep-sea sediment. *International Journal of Systematic and Evolutionary Microbiology* 64, 668–674.

Fehr, A., Andersson, P.S., Hålenius, U., Gustafsson, O., and Mörth, C.-M. (2010). Iron enrichments and Fe isotopic compositions of surface sediments from the Gotland Deep, Baltic Sea. *Chemical Geology*, 277, 310-322

Finkmann, W., Altendorf, K., Stackebrandt, E., and Lipski, A. (2000). Characterization of N_2O-producing Xanthomonas-like isolates from biofilters as Stenotrophomonas nitritireducens sp. nov., Luteimonas mephitis gen. nov., sp. nov. and Pseudoxanthomonas broegbernensis gen. nov., sp. nov. *International Journal of Systematic and Evolutionary Microbiology* 50, 273–282.

Gallagher, K.L., C. Dupraz, O. Braissant, R.S. Norman, A.W. Decho, P.T. Visscher. (2011). Mineralization of sedimentary biofilms: Modern mechanistic insights. *In: Biofilms: Formation, Development and Properties. W.C. Bailey (ed). NOVA Publishers, New York, NY*, pp. 227-258

Gomes, J., Cocke, D., Moreno, H., Tran, D., Mahmud, A., Das, K., and Guttula, M. (2009). Green rust: its electrochemical generation, characterization, and implications. *EPD Congress 2009, TMS (The Minerals, Metals & Materials Society), 211-218.*

Guillou, L., Bachar, D., Audic, S., Bass, D., Berney, C., Bittner, L., Boutte, C., Burgaud, G., de Vargas, C., Decelle, J. (2013). The Protist Ribosomal Reference database (PR2): a catalog of unicellular eukaryote small sub-unit rRNA sequences with curated taxonomy. *Nucleic Acids Research* 41, D597-604.

Han, Y., and Perner, M. (2015). The globally widespread genus Sulfurimonas: versatile energy metabolisms and adaptations to redox clines. *Frontiers in microbiology* 6, 989.

Hutt, L.P., Huntemann, M., Clum, A., Pillay, M., Palaniappan, K., Varghese, N., Mikhailova, N., Stamatis, D., Reddy, T., Daum, C. (2017). Permanent draft genome of Thiobacillus thioparus DSM 505T, an obligately chemolithoautotrophic member of the Betaproteobacteria. Standards in Genomic Sciences 12, 10. 10.1186/s40793-017-0229-3.

Izadi, M., Yazdiyan, A., Shahrabi, T., Hoseinieh, S.M., and Shahrabi, H.(2019) Influence of Temperature Variation on the Formation and Corrosion Protective Performance of Calcium Carbonate Deposits in Artificial Seawater. *JMEPEG,* 28, 4221–4233

Jakobsson, M., Stranne, C., Fornander, R., O'Regan, M., Wagner, A. and the *EL21-Estonia* Shipboard Party (2021). Report of the MS *Estonia* shipwreck site survey with RV *Electra. Meddelanden från Stockholms universitets institution för geologiska vetenskaper* No 383. Pp. 96.

Jang, S.H., Jeong, H.J., Lee, M.J., Kim, J.H., and You, J.H. (2019). Gyrodinium jinhaense n. sp., a New Heterotrophic Unarmored Dinoflagellate from the Coastal Waters of Korea. *Journal of Eukaryotic Microbiology* 66, 821–835.

Karnachuk, O.V., Kurochkina, S.Y., and Tuovinen, O.H. (2002). Growth of sulfate-reducing bacteria with solid-phase electron acceptors. *Appl. Microbiol. and Biot*., 58, 482-486.

Kim, M.-S., Kim, T.-H., Sun, Y., Jae-Min, J., and Park, J.K. (2017). A novel synthesis of an Fe^{3+}/Fe^{2+} layered double hydroxide ('green rust') via controlled electron transfer with a conducting polymer. *Dalton Trans*., 46, 7656

Kip, N. and van Veen (2015). The dual role of microbes in corrosion. The ISME Journal, 9, 542-551.

Könneke, M., Kuever, J., Galushko, A., and Jørgensen, B.B. (2013). Desulfoconvexum algidum gen. nov., sp. nov., a psychrophilic sulfate-reducing bacterium isolated from a permanently cold marine sediment. *International Journal of Systematic and Evolutionary Microbiology* 63, 959–964.

Kuever, J. (2014). The Family *Desulfobacteraceae.* In: *The Prokaryotes*, eds. Rosenberg, E., DeLong, E.F., Lory, S., Stackebrandt, E., Thompson, F. Springer, Berlin, Heidelberg, p. 45-73.

Lekbach, Y., Liu, T., Li, Y. Moradi, M., Dou, W., Xu, D., Smith, J.A., and Lovley, D.R. (2021). Chapter Five - Microbial corrosion of metals: The corrosion microbiome. Advances in Microbial Physiology. 78, 317-390.

Li, Y., Wang, S., Ji, B., Yuan, Q., Wei, S., Lai, Q., Wu, K., Jiang, L., and Shao, Z. (2023). Sulfurovum mangrovi sp. nov., an obligately chemolithoautotrophic, hydrogen-oxidizing bacterium isolated from coastal marine sediments. International Journal of Systematic and Evolutionary Microbiology 73, 006142.

Lindahl, O. and Hernrot, L. (1983) Phyto-Zooplankton Community in Coastal Waters of Western Sweden - An Ecosystem Off Balance? Mar. Ecol. Prog. Ser., 10, 119-126.

Lu, J., Cheng, G., Chen, L., Xiong, G., And Wang, L. (2018). Distribution and Morphology of MnS Inclusions in Resulfurized Non-Quenched and Tempered Steel with Zr Addition. *ISIJI International*, Vol. 58, No. 7, pp. 1307–1315

Martin, M. (2011). Cutadapt removes adapter sequences from high-throughput sequencing reads. EMBnet.journal 17, 1 (2011), 10–12. Retrieved from:

http://journal.embnet.org/index.php/embnetjournal/article/view/200 (accessed January, 2024).

Megonigal, J.P., Hines, M.E, and Visscher, P.T., 2003. Anaerobic metabolism and production of trace gases. In: Holland, H.D., Turekian, K.K. (Eds.), Treatise on Geochemistry 8. Elsevier, pp. 317-424.

Melchers, R.E. (2006). The marine corrosion of structural steels in brackish and fresh waters. Structure and Infrastructure Engineering, Vol. 2, No. 1, 53 – 61

Merz, E., Dick, G.J., de Beer, D., Grim, S., Hübener, T., Littmann, S., Olsen, K., Stuart, D., Lavik, G. et al. (2021). Nitrate respiration and diel migration patterns of diatoms are linked in sediments underneath a microbial mat. *Environmental Microbiology* 23, 1422-1435.

Möller, H. Boshoff, E.T., , and Froneman H., 2006. The corrosion behaviour of a low carbon steel in natural and syntheti seawaters *Journal of The South African Institute of Mining and Metallurgy* volume 106. 585-592.

Murphy, C.L., Biggerstaff, J., Eichhorn, A., Ewing, E., Shahan, R., Soriano, D., Stewart, S., VanMol, K., Walker, R., Walters, P. (2021). Genomic characterization of three novel Desulfobacterota classes expand the metabolic and phylogenetic diversity of the phylum. *Environmental Microbiology* 23, 4326–4343.

Ocean Discovery AB (2022). Photogrammetry documentation of Estonia. Retrieved from: https://estonia.havkom.se/en/ship/section/Back115 (accessed October 2023).

Ohfuji. H. anD. Rickard (2005) Experimental synthesis of framboids – a review. *Earth-Science Reviews*, 71:147-170

Osvatic, J.T., Yuen, B., Kunert, M., Wilkins, L., Hausmann, B., Girguis, P., Lundin, K., Taylor, J., Jospin, G., and Petersen, J.M. (2023). Gene loss and symbiont switching during adaptation to the deep sea in a globally distributed symbiosis. *The ISME Journal* 17, 453–466.

Wasmund, N., Tuimala, J., Suikkanen, S., Vandepitte, L., And Kraberg, A. (2011). Long-term trends in phytoplankton composition in the western and central Baltic Sea. *Journ. of Mar. Systems,* 87, 145-159.

Perez-Bernal, M.F., Souza Brito, E.M., 1,2, Bartoli, M., Aubé, J., FardeauM.-L., Rodriguez, G.C., Ollivier, B., Guyoneau, R., and Hirschler-Réa, A. (2017). *Intern. Journ. Syst. And Evol. Microb., 67, 4999-5005.*

Pineau, S., Sabot, R., Quillet, L., Jeannin, M., Caplat, C., Dupont-Morral, I., Refait, P. (2008) Formation of the Fe(II–III) hydroxysulphate green rust during marine corrosion of steel associated to molecular detection of dissimilatory sulphite-reductase. *Corrosion Science*, 50, 1099–1111.

Quast, C., Pruesse, E., Yilmaz, P., Gerken, J., Schweer, T., Yarza, P., Peplies, J., and Glöckner, F.O. (2013). The SILVA ribosomal RNA gene database project: improved data processing and web-based tools. *Nucleic Acids Research* 41, D590-596.

Refait, P., Grolleau, A.-M., Jeannin, M., Rémazeilles, C. and Sabot, R. (2020). Corrosion of Carbon Steel in Marine Environments: Role of the Corrosion Product Layer. *MDPI, Corros. Mater. Degrad.,* 1, 198–218

Romanenko, L.A., Uchino, M., Tanaka, N., Frolova, G.M., Slinkina, N.N., and Mikhailov, V.V. (2008). Occurrence and antagonistic potential of Stenotrophomonas strains isolated from deep-sea invertebrates. *Archives of microbiology* 189, 337–344.

Sancho Tomas M. (2014). Calcium Carbonate bio-precipitation in gelling environments via counter-diffusion. PhD Thesis. Laboratorio de Estudios Cristalográficos, Instituto Andaluz de Ciencias de la Tierra, CSIC-UGR. Dipartimento di Chimica «Giacomo Ciamician», Università di Bologna. Pp. 165.

Sawlowicz, Z. (2000): Framboids: from their origin to application. *Minerlogic Transactions 88*, 1–80

Seemann, T. (2024). Barrnap. Retrieved from: https://github.com/tseemann/barrnap (accessed January, 2024).

Sorokin D. Y., Tourova T. P., Kolganova T. V., Detkova E. N., Galinski E. A. and Muyzer G. (2011). Culturable diversity of lithotrophic haloalkaliphilic sulfate-reducing bacteria in soda lakes and the description of *Desulfonatronum thioautotrophicum* sp. nov., *Desulfonatronum thiosulfatophilum* sp. nov., *Desulfonatronovibrio thiodismutans* sp. nov., and *Desulfonatronovibrio magnus* sp. nov. *Extremophiles* 15:391-401

Straub, D., Blackwell, N., Langarica-Fuentes, A., Peltzer, A., Nahnsen, S., and Kleindienst, S. (2020). Interpretations of Environmental Microbial Community Studies Are Biased by the Selected 16S rRNA (Gene) Amplicon Sequencing Pipeline. *Frontiers in Microbiology* 11.

Suikkanen, S., Hakanen, P., Spilling, K., Kremp, A. (2011). Allelopathic effects of Baltic Sea spring bloom dinoflagellates on co-occurring phytoplankton. *MEPS* 439, 45-55.

Tanja Magoč and Steven L. Salzberg. (2011). FLASH: Fast Length Adjustment of Short Reads to Improve Genome Assemblies. *Bioinformatics* 27, 21 (September 2011), 2957–2963.

Timmer-ten Hoor, A. (1975). A new type of thiosulphate- oxidizing, nitrate reducing microorganism: Thiomi- crospira denitrificans sp.nov. *Neth. J. Sea Res*. 9:344– 350.

Van Driessche, A.E.S. (2007). In situ observation of protein crystal growth by advanced optical techniques. Laboratorio de Estudios Cristalograficos. Tesis Doctoral, Instituto Andaluz de Ciencias de al Tierra CSIC – Universidad de Granada. Pp. 275.

Videla, A. and Herrera, L.K. (2009). Understanding microbial inhibition of corrosion. A comprehensive overview International Biodeterioration & Biodegradation, 63, 896-900.

Visscher P.T. and Stolz J.F. (2005). Microbial mats as bioreactors: populations, processes, and products. *Palaeogeogr. Palaeoclimatol. Palaeoecol.* 219, 87–100

Wentworth, C.K. (1922). A scale of grade and class terms for clastic sediments. *The Journal of Geology*, 30, 377-392.

Wickham, H., Averick, M., Bryan, J., Chang, W., McGowan, L.D., François, R., Grolemund, G., Hayes, A., Henry, L., Hester, J. (2019). Welcome to the Tidyverse. *Journal of Open Source Software* 4, 1686.

Williams, A.G.B. and Scherer, M.M. (2001). Kinetics of Cr(VI) Reduction by Carbonate Green Rust. Environ. Sci. Technol., 35, 3488-3494 .

World Material. Retrieved from: https://www.theworldmaterial.com/type-304-grade-stainless-steel (accessed on January 19, 2024).

Zakharyuk, A.G., Kozyreva, L.P., Khijniak, T.V., Namsaraev, B.B., and Shcherbakova, V.A. (2015). Desulfonatronum zhilinae sp. nov., a novel haloalkaliphilic sulfate-reducing bacterium from soda Lake Alginskoe, Trans-Baikal Region, Russia. *Extremophiles* 19, 673–680.

APPENDIX

ANNEX I – SYNTHESIS MODEL OF THE MS *ESTONIA* CORROSION PRODUCT

This section aims to assess the microbiological and chemical processes that resulted in the deposition of material on the hull of the MS *Estonia* shipwreck around the front hole on the starboard side.

CORROSION MODEL AND CORROSION PRODUCT LAYER

The MS *Estonia* was built using coated steel that was protected from corrosion. The damage inflicted to the hull at the fractured area torn up and removed this coating, exposing unprotected steel to the seawater for almost 30 years. The conceptual model presented in Figures 1 explains how the different corrosion products that form when steel is exposed to seawater for a prolonged period of time. Corrosion is a natural process involving complex interactions between biological and physicochemical processes that convert a refined metal into a more chemically stable form, such as oxide, hydroxide, or sulfide (Melchers, 2006). The gradual destruction of the original steel surface by biological and chemical reactions produces a corrosion product layer (CPL), that is complex in structure and composition. Sampling by suction or scraping does not preserve the 3-dimensional structure and organization of the CPL, (as all products are mixed during sampling). However, all components present in the investigated samples are associated with the CPL, and their formation is explained in detail below.

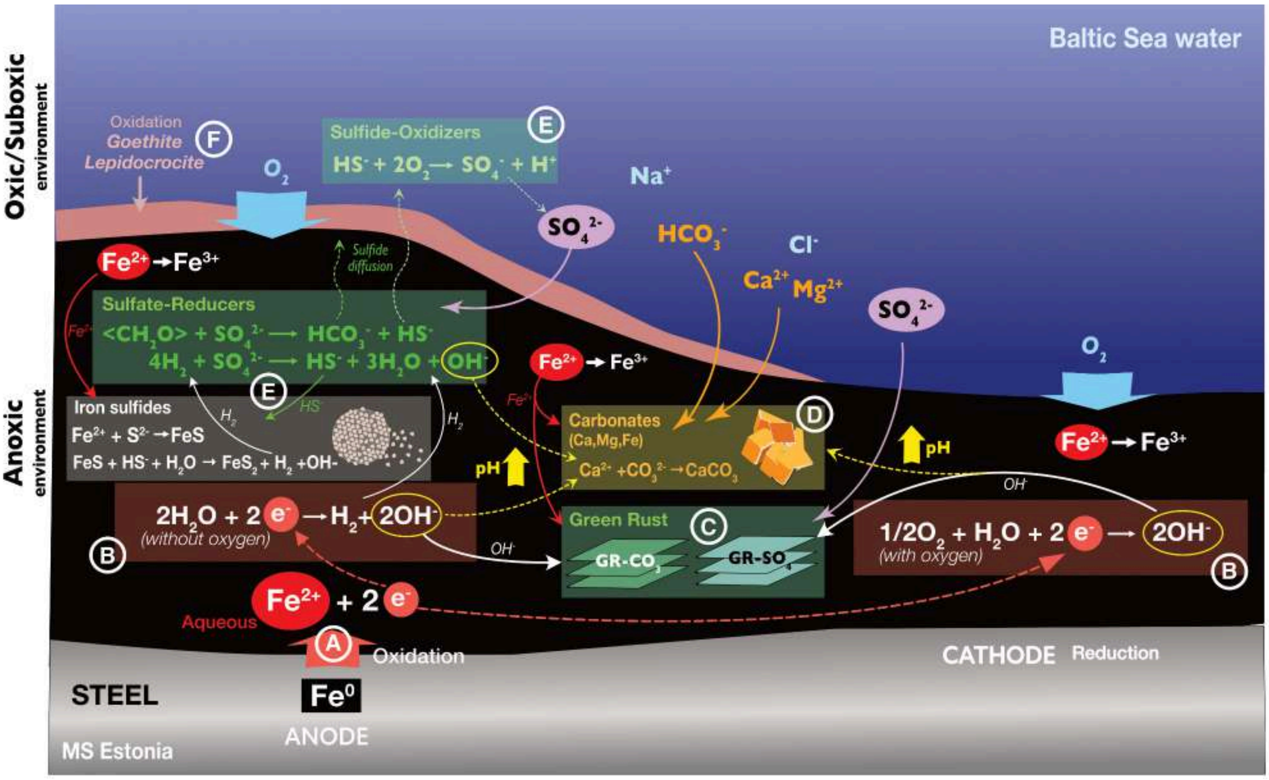

A

Fe^0 oxidation (Anode)

$Fe^0 \rightarrow Fe^{2+} + e^-$ (chemical)

B

O_2 and H_2O reduction (Cathode)

$\frac{1}{2}O_2 + H_2O + 2e^- \rightarrow 2OH^-$ (chemical)

$2H_2O + 2e^- \rightarrow H_2 + 2OH^-$ (chemical)

C

Formation of iron hydroxide (Initial corrosion product)

$Fe^{2+} + 2OH^- \rightarrow Fe(OH)_2$ (chemical)

Formation of Green Rust (GR-SO_4) (Corrosion product)

$6Fe^{2+} + 10OH^- + SO_4^{2-} + 21O_2 + 9H_2O \rightarrow$ **GR(SO4)*** (chemical)

$6Fe^{2+} + 10OH^- + SO_4^{2-} + 10H_2O \rightarrow$ **GR(SO4)*** $+ H_2$ (chemical)

D

Formation of Carbonate ions and calcium carbonates

$HCO_3^- + OH^- \rightarrow CO_3^{2-} + H_2O$ (chemical)

$CO_3^{2-} + Ca^{2+} \rightarrow CaCO_3$ (chemical)

E

Sulfate reduction

$4H_2 + SO_4^{2-} \rightarrow HS^- + 3H_2O + OH^-$ (microbial)

$2CH_2O + SO_4^{2-} + OH^- \rightarrow 2HCO_3^- + HS^- + H_2O$ (microbial)

Sulfide oxidation

$HS^- + 2O_2 \rightarrow SO_4^{2-} + H^+$ (microbial, aerobic)

$5HS^- + 8NO_3^- \rightarrow 5SO_4^{2-} + 4N_2 + H_2O$ (microbial, anaerobic)

Formation of Iron sulfide

$FeS + HS^- + H_2O \rightarrow FeS_2 + H_2 + OH^-$ (chemical neutral)

$HS^- + OH^- \rightarrow S^{2-} + H_2O$ (chemical)

$Fe^{2+} + S^{2-} \rightarrow FeS$ (chemical basic)

F

Formation of Lepidocrocite from GR-SO_4 (More oxidized product)

$Fe^{II}_4Fe^{III}_2(OH)12SO_4 \cdot nH_2O + 1/2O_2 + 3H_20$
$\rightarrow 8FeOOH$ (Lepidocrocite) $+ 2SO_4^{2-} + (n+3)H_2O$

* *Green Rust incorporating sulfates with the formula* $(Fe^{2+}_4Fe^{3+}_2(OH)12SO_4 \cdot 8H_2O$

Fig. 1. **Corrosion Process of Steel in Baltic Sea water (MS *Estonia* Model).** This conceptual model represents a dynamic interplay of chemical and biological processes contributing to the corrosion system:

A. **Initial Oxidation of Fe^0 (Anode Reaction)**: The steel structure serves as an anode where metallic iron (Fe^0) is oxidized into Fe^{2+} and electrons. Fe^{2+} is soluble in water and will diffuse in the layer.

B. **Reduction of H_2O and O_2 (Cathode Reaction)**: The electrons produced in (A) reduce water to form hydroxide ions (OH^-) and hydrogen gas (H_2). In the presence of O_2, both water and O_2 are reduced into OH^-. This process consumes O_2 and may lead to the formation of an anoxic water layer at the steel surface. The dysoxic bottom water favors this process.

C. **Rust Formation**: Soluble Fe^{2+} ions react with OH^- to precipitate as iron hydroxide, a precursor to rust. In the neutral to slightly alkaline conditions of the MS *Estonia* shipwreck (typical for marine water), the partially oxidized form of $Fe(OH)_2$ leads to the formation of green rust. This occurs with the partial oxidation of Fe^{2+} in $Fe(OH)_2$, creating a mixed-valence material. The produced structure is characterized by alternating layers of Fe^{2+} and Fe^{3+} hydroxides, separated by layers of water molecules or ions (Fig. 2). GR formation can be enhanced by the presence of specific microbial communities found in investigated samples, such as sulfate-reducing bacteria (Desulfovibrio, Desulfobacter; Gomes et al, 2009, Refait et al., 2020). GR can incorporate other ions like chloride (Cl^-), sulfate (SO_4^{2-}), and carbonate (CO_3^{2-}) coming from the seawater in between the iron-hydroxide layers.

D. **Carbonate Precipitation**: Release of OH^- during corrosion may increase in pH near the cathode and can also facilitate the formation of carbonate ions from bicarbonate, which can bind to calcium from the seawater and form calcium carbonate. These carbonate minerals can incorporate various amounts of iron (Fe^{2+}) and magnesium (Mg^{2+}) ion.

E. **Microbial Influence**: Within the less oxygenated inner layers, anaerobic microbes thrive, notably driving the sulfur cycle. Sulfate-reducing bacteria (SRB) convert sulfate to sulfide, that in turn can react with Fe^{2+} to form iron sulfides (FeS, FeS_2 - pyrite). SR activity coupled to H_2 produced during water reduction (B), or, alternatively, organic matter (CH_2O). This reaction releases OH- ions, increasing pH that further favors the precipitation of carbonate minerals. Some dissolved sulfides may diffuse through the layer and be cycled back by sulfide-oxidizing bacteria, converting them into sulfate (SO_4^{2-}) or elemental sulfur (S^0), completing the sulfur cycle. Note: CH_2O is used as a generic formula for organic matter

F. **Further Oxidation**: When oxygen is available, intermediate compounds like green rust (GR) [and sulfide deposits can be further oxidized, leading to the formation of more stable Fe^{3+}-hydroxides such as goethite and lepidocrocite.

IRON (FE) OXIDATION STATES

The chemical element iron (Fe) can be found in this study in varying oxidation states, depending on its electron count. Elemental iron, or Fe^0, retains all its electrons, composing the bulk of steel. Fe(II) or Fe^{2+} has surrendered two electrons and is referred to as ferrous iron. Fe^{2+} is more chemically reactive than Fe^0 and typically exists in oxygen-poor environments, where it is soluble. In the report findings, Fe^{2+} appears in green rust (GR), GR(SO4), and within sulfide minerals like FeS and Pyrite (FeS_2). Fe^{3+} or Fe(III), also called ferric iron, has lost three electrons. This form is less soluble in water compared to Fe(II) and often forms minerals that display a distinctive red-orange hue. Hence, a typical iron oxidation sequence progresses from metallic iron (Fe0) to ferrous (Fe^{2+}), and ultimately to ferric iron (Fe^{3+}), which is accompanied by notable structural and color changes. Fe^{2+} and Fe(II) as well as Fe^{3+} and Fe(III) are used equivalently in this text.

CORROSION PRODUCTS LAYERS

The corrosion product layer (CPL) can develop at the surface of the seawater-exposed steel already after within a few months (Refait et al., 2020). This layer is generally composed of three strata (Fig. 1), which formation mostly result from the presence (oxic zone) or absence of oxygen (anoxic zone). (1) a biofouling zone composed of macroscopic encrusting eukaryotes, shells, and sediment (oxic environment) (2) An outer stratum composed of an orange-brown corrosion product, mainly composed of Fe(III)-oxyhydroxides (FeOOH) (in this case, lepidocrocite and goethite; (Sample H2)). (3) A black inner stratum directly in contact with the steel and generally composed of Fe^{2+}-rich or a mixed Fe^{2+}/Fe^{3+} corrosion products (GR and iron sulfides in this study).

Sample groups 3 and 4 that have a metal signature primarily consist of corrosion products such as GR and sulfide that form in the inner, oxygen-limited stratum. Only one of these samples (H2) shows more oxidized phases consistent with the outer oxic layer (Fe^{3+} hydroxides). In marine environments, the black inner stratum tends to increase in thickness with time (over years) compared to the outer, more oxidized layer (Refait et al.2020). This creates an anoxic environment (without oxygen) in which anaerobe microorganisms (living without oxygen) thrive (see below). The production of iron hydroxides at the steel surface is explained by the steel-water couple, functioning like a battery, with the metallic iron (Fe^0) being oxidized into Fe^{2+} at the anode side, O_2, and H_2O being reduced to OH^- at the cathode side (Eq. 1 and 2; Fig. 1). In contact with water, a redox reaction takes place, with the metallic iron being oxidized into Fe^{2+} (oxidation state +2; Eq. 1):

$$\text{(oxidation) } Fe^0_{(s)} \rightarrow Fe^{2+}_{(aq)} + 2e^- \qquad (1)$$

The two electrons that have been removed from Fe^0 (Eq. 1) can be transferred to water that will then be reduced to hydrogen gas (H_2) and hydroxide ions (OH^-), (Eq. 2). In the presence of oxygen, O_2 is reduced to yield OH^- ions, producing an oxygen-depleted environment (Eq. 3)

$$\text{(Reduction) } 2H_2O_{(l)} + 2e^- \rightarrow H_{2(g)} + 2OH^-_{(aq)} \qquad (2)$$

$$\text{(Reduction) } \tfrac{1}{2}O_{2(g)} + H_2O_{(l)} + 2e^- \rightarrow 2OH^-_{(aq)} \qquad (3)$$

Fe^{2+} and OH^- can combine in a solid Fe(II)-hydroxide phase, thereby forming one of the first corrosion products of the inner layer (Eq. 4).

$$Fe^{2+}_{(aq)} + 2OH^-_{(aq)} \rightarrow Fe(OH)_{2(s)} \qquad (4)$$

This inner black layer is anoxic, allowing bacteria using anaerobic metabolisms (respiration independent of O_2) to thrive (e.g., sulfate-reducing bacteria; see below). In the case of anoxic bottom seawater, the outer stratum may not form, and the corrosion layer main remain black. In the case of the MS *Estonia*, the oxygen level in the environment surrounding the hull likely fluctuated over time, leading to periods of dysoxic conditions. This could explain the generally dark color of the corrosion products.

PROCESSES INVOLVED IN THE FORMATION OF THE OBSERVED PHASES

GREEN RUST (FIG. 1C)

Green Rust (GR) is a major component of the investigated samples with a metal signature (group 3-4) detected, using XRD validated chemically by SEM-EDS. GR is known to be an intermediate product in the oxidative transformation of steel (Izadi et al., 2019, Pineau et al., 2008; Refait et al., 2020). It can be formed biotically or abiotically in suboxic, neutral to moderately alkaline environmental conditions.

The mineralogical structure of GR is layered with the general composition

$$[Fe^{II}_{(6-x)}\,Fe^{III}_{x}(OH)_{12}]^{x+}[(A)_{x/n} \cdot yH_2O]^{x-} \quad (5)$$

Where x ranges from 0.9 to 4.2, “A” is an n-valent anion such as CO_3^{2-}, Cl^- or SO_4^{2-}, and “y” indicates the number of interlayer water molecules (typically ranging from 2 to 4) (Williams and Scherer 2001; Gomes et al., 2009). GR is a pyroaurite-type mineral belonging to the group of layered double hydroxides (LDHs), in which positively charged layers of metal hydroxides alternate with layers of anions (in this case, sulfates and possibly carbonates, Fig. 2). The crystallographic classification of the mineral structures is dependent of the incorporated ions and can be subdivided into 3 variants: (1) GRI, which contains monovalent ions (e.g., F^-, Cl^-, Br^-), (2) GRII, which contains ions SO_4^{2-}, (3) GR-CO_3, with CO_3^{2-} as the anion.

The composition of green rust (GR) minerals can vary significantly and is influenced by the degree of Fe^{3+} incorporation within the iron-hydroxide layer as well as the type of ions present in the interstitial layers. X-ray diffraction (XRD) studies revealed the presence of an iron sulfate hydroxide hydrate phase in the investigated samples. Despite not being designated as GR(SO4) in the ICDD PDF-4+ database, the empirical formula of the phase detected in this study corresponds to that of GR(SO4). The samples may contain a diverse range of green rust (GR) compositions, with X-ray diffraction (XRD) only providing a broad perspective of the overall phase compositions.

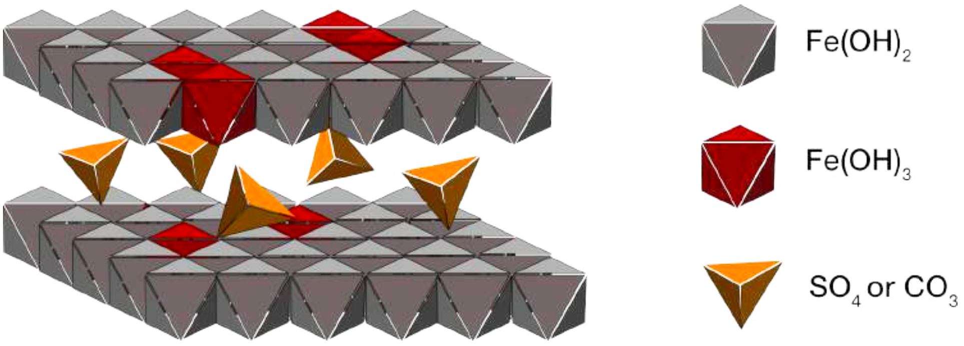

Fig. 2. Structure of the Green Rust (modified from Kim et al., 2017).

Green rust (GR) is recognized in the literature as an important transitional phase in the corrosion process of steel, where it forms an unstable mixture of ferrous and ferric hydroxides (e.g., Gomes et al., 2009, Refait et al., 2020). Given that the MS *Estonia* has been submerged in seawater for three decades, the persistently black appearance of the corroded area suggests that the environmental conditions have not permitted the formation of iron phases with a higher degree of oxidation than that of GR, resulting in a corrosion layer mainly comprising Green Rust and iron sulfides and iron-rich calcium carbonates, as observed.

Iron sulfides (Fig. 1E)

Many of the investigated samples contain iron sulfides, predominantly framboidal pyrite (FeS_2). To form iron sulfide minerals, there must be a supply of Fe^{2+} and sulfides ($H_2S/HS^-/S^{2-}$). The iron needed for this mineral to precipitate is derived from steel corrosion. While framboids can be synthetized in laboratory without the presence of microbes (Ohfuji and Rickard, 2005), in modern marine environments, these sulfides are predominantly formed by the action of sulfate-reducing bacteria, indicating a microbial origin of iron sulfide deposits found in this study (Sawlowicz, 2000). Within the oxygen-poor inner layers, anaerobic microbes thrive, especially the sulfur cycle organisms as sulfate is present in large amounts in seawater (ranging from 800 to 1,500 mg/L for the Baltic sea) Sulfate-reducing bacteria (SRB) convert sulfate to sulfide, which in turn reacts with Fe^{2+} to form iron sulfides (FeS, FeS_2 - pyrite). SR activity is supported by H_2 produced during water reduction (Annex I), or by CH_2O (Fig 65E). This reaction releases OH^- ions, increasing pH favoring the precipitation of carbonate minerals (Dupraz et al., 2009). Some dissolved sulfides may diffuse through the layer and be cycled back by sulfide-oxidizing bacteria, that depend on nitrate or low concentrations of oxygen (e.g., *Thiomicrospira* bacteria) for this, converting these sulfide into sulfate (SO_4^{2-}), “elemental” sulfur (S^0), polythionates ($((SO_3)_2S_y)$), or polysulfides (S_x^{2-})), completing the sulfur cycle.

Carbonates (Fig. 1D)

Calcium carbonates are found in many of the analyzed samples. At the cathode, the reduction of water or O_2 produces hydroxide ions (OH^-) that leads to an increase in the local pH. In the presence of other ions, such as bicarbonate (HCO_3^-, which is abundant in seawater) and calcium (Ca^{2+}), the precipitation of calcium carbonate ($CaCO_3$) minerals can take place (Fig. 64D; Möller et al., 2006). This phenomenon can be observed in marine environments, in which the carbonate precipitation acts like a shield against further Fe0 oxidation. This protective carbonate layer can thus slow down the corrosion process under certain conditions (Izadi et al., 2019). During calcium carbonate precipitation, iron (Fe^{2+}) and magnesium (Mg^{2+}, present in seawater) can be incorporated into the mineral. Carbonate precipitation can be influenced or induced by microbial activity (Dupraz et al., 2009). Bacterial metabolism, such as sulfate reduction, may increase the pH and reinforce the alkaline condition favoring the precipitation of carbonates (Visscher and Stolz, 2005; Dupraz and Visscher, 2005). This process explains the widespread distribution of iron-rich carbonates in the MS *Estonia* corrosion deposits.

Fe^{3+} HYDROXIDES (LEPIDOCROCITE, GOETHITE; FIG.1F)

Fe(II)-phases present at the surface of the inner layer and in contact with the surrounding oxygenated water can be further oxidized into Fe(II)Fe(III)-phases (mixing both, like in GR) or Fe(III)-phases that form the orange-colored outer layer (e.g., in lepidocrocite and goethite). Sample ES-23-H2 is the only in which Fe(III) hydroxides are present. No GR or iron sulfide is observed indicating a complete oxidation of the original intermediate rust phase. The sample was taken close to a reddish portion of the hull (Figs. 2, 5). It is possible that the higher relief of this section exposed the rust to more fluid flow, inducing a higher exposure of oxygenated water. It is also possible that the texture of the rust deposit allows for more diffusion.

TRACE ELEMENT ENRICHMENT

Microbial communities typically organize themselves into biofilms attached to a solid substrate. These communities are embedded in extracellular organic matter (EOM), which acts as diffusion barriers that allow for a wide range of metabolic activities to coexist. The protective effect of EOM combined with highly flexible metabolisms strongly improves the tolerance of those communities to environmental stressors (such as high salinity, desiccation, nutrient limitation, extreme pH predation by protozoa), which is why microbial mats and biofilms thrive in extreme conditions. Acidic functional groups (negatively charged organic molecules) within the EOM can chemically bind positively charged ions (cations) (Braissant et al., 2007, Dupraz et al., 2009.) In the case of rust, the gradual breakdown of steel releases various elements besides iron. Steel contains trace elements like Mn, Ni, Co, Cu, Cr, Ga, V, and As, all of which carry a positive charge and can be sequestered by EOM. Thus, as corrosion products like green rust (GR) and carbonates form within biofilms, these minerals can become enriched in such elements, explaining why some rust layers have higher trace element concentrations than the original steel.

CORROSION PRODUCTS AS AN 'ECOSYSTEM'

Rust is not solely a result of physicochemical processes; it also comprises a significant biological component, specifically that of microbial communities. Viewed from a geomicrobiology perspective, the product of steel corrosion can be interpreted as a dynamic ecosystem. Within this ecosystem, chemical elements undergo cycles of transformation, mediated by both physicochemical reactions and microbiological processes. In contrast to eukaryotic organisms such as plants and animals, which are generally confined to oxygen-rich (oxic) environments, microbial communities are capable of thriving in environments devoid of oxygen (anoxic), through chemical (redox) reactions involving a wide range of chemical components (e.g., S, N, Fe), thereby altering their solubility (i.e., phase dissolution and precipitation).

The mineral products observed in the investigated samples result from complex interactions between the physicochemical environmental characteristics (the shipwreck, the Baltic Sea water, and the surrounding sediment) and microbiological processes that are summarized in Figure 3. The environmental conditions not only control the composition of microbial communities but also affects the type and rate of their metabolic processes. It also influences the stability of the corrosion products. The microbial communities create micro-environments (e.g., anoxic micro-environments in oxic bulk water), facilitate the formation of new substrates, and modify the properties of the corrosion products (porosity, permeability, diffusion).

Microbes can play a passive or active role in the formation of rust, significantly influencing the corrosion process and its outcomes (Videla and Herrera, 2009; Lekbach et al., 2021; Kip and vanVeen, 2015). In a passive role, bacteria that are subjected to the physicochemical processes (e.g., electrochemical reactions), can still affect rust formation by their sheer physical presence. Their cell and exopolymer structures, once integrated into the rust, can alter its texture and structure, potentially affecting its porosity and the way it adheres to metal surfaces (e.g., encrusted filaments). In an active role, metabolic processes directly contribute to the initiation and progression of rust formation through biochemical reactions catalyzing the precipitation and dissolution of minerals (Kip and van Veen, 2015; Lekbach et al., 2021; Dupraz et al., 2009; Visscher and Dupraz, 2005). For example, microbial communities that perform aerobic respiration (i.e., the same respiration as us, breathing O_2) may consume all oxygen and create localized anoxic conditions that can modify both the rate at which rust forms and the nature of the rust itself. Other microbial processes may influence rust formation through the production of metabolites that either promote or inhibit the formation of rust Kip and van Veen 2015, Lekbach et al., 2021). This biochemical activity can lead to the formation of rust with distinct properties, which may differ significantly from rust formed purely through abiotic processes.

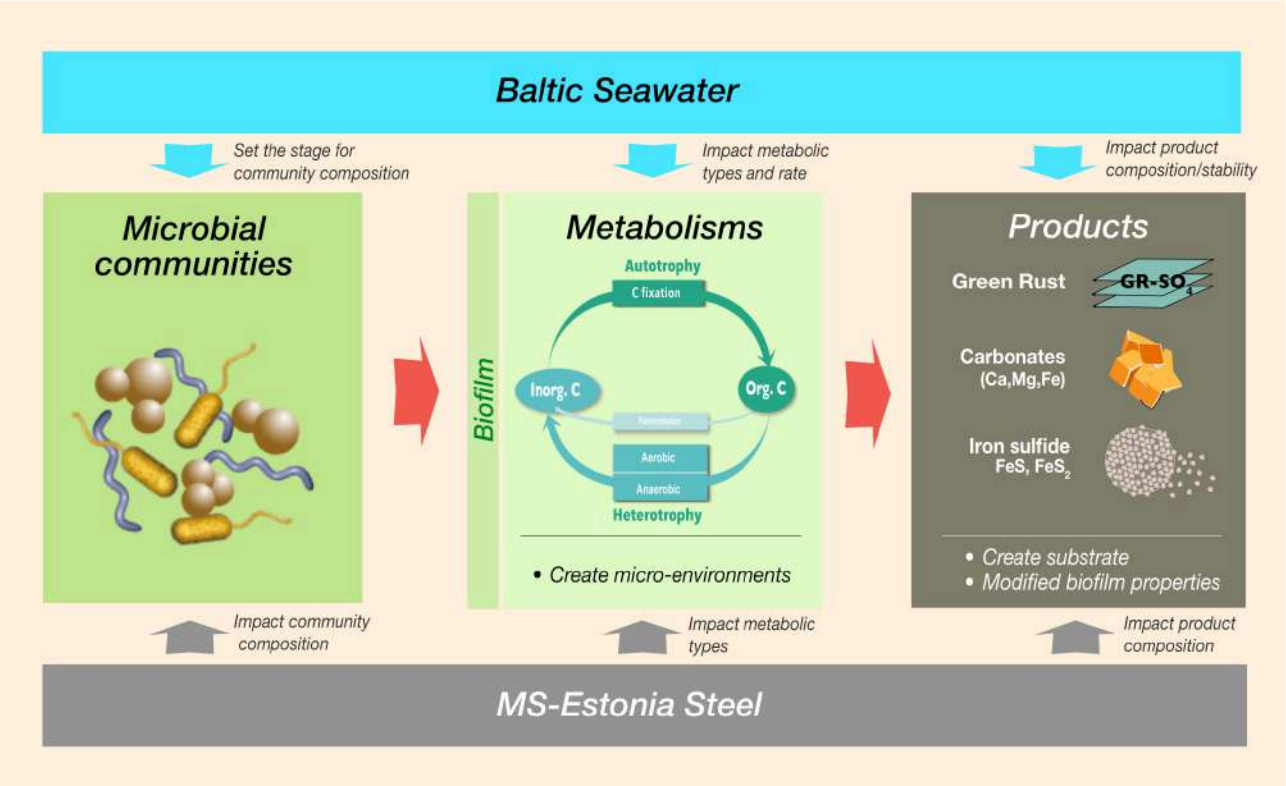

Fig. 3: The corrosion product ecosystem. The corrosion products result from the interaction between the physical environment (including the ship, the surrounding sediment, and the Baltic Sea water) and the associated microbial communities.

ANNEX II – EDS SPECTRUM OF THE ANALYZED SAMPLES

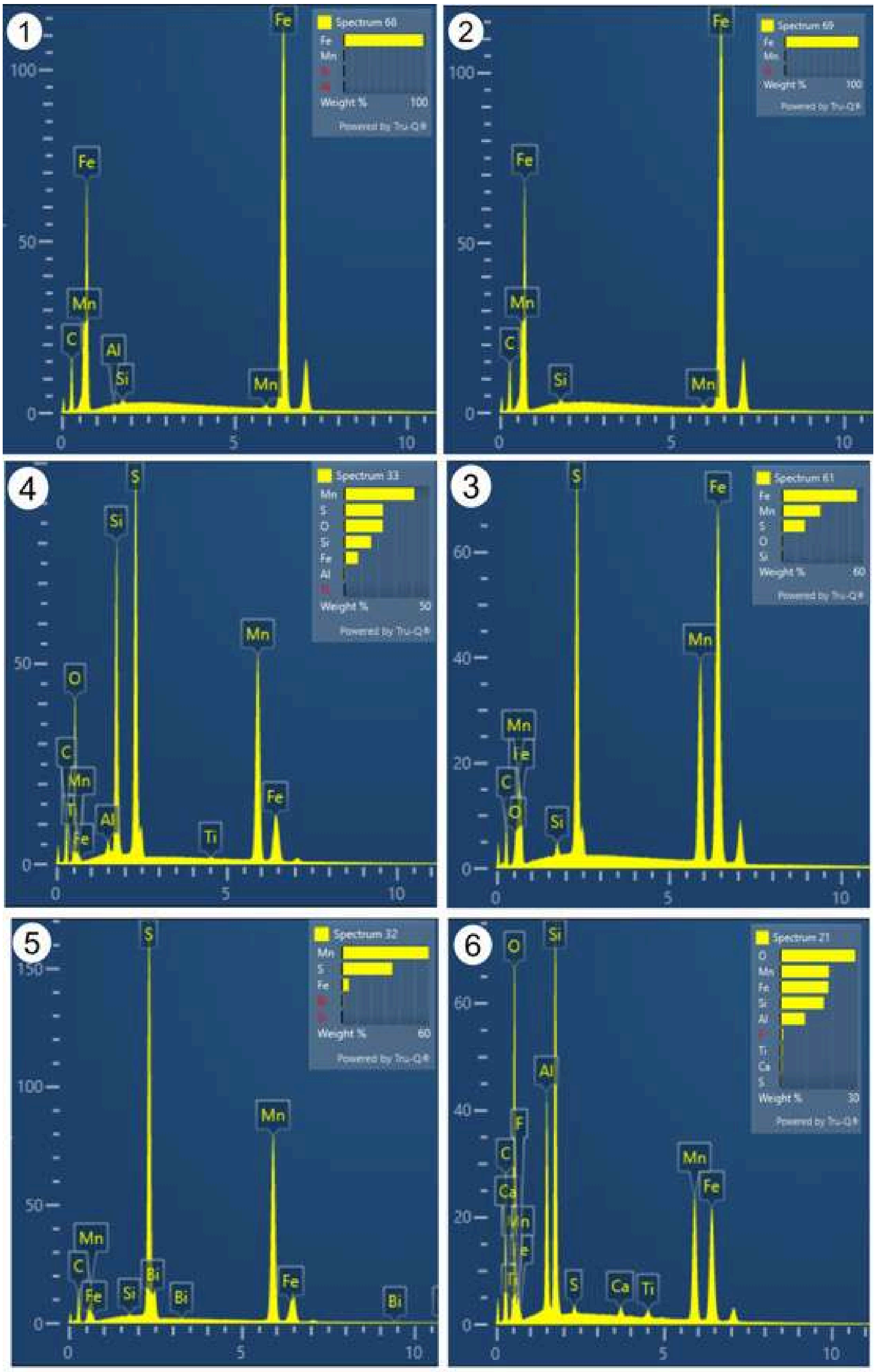

Figure 1. Cut out steel sample - EDS-derived chemical profiles defined in Fig. 8. **Phase 1 and 2**: Light and dark steel crystals show similar spectra a metal Fe phase. **Phase 3**: Spectrum showing Mn, S and Fe. **Phase 4**: Spectrum taken in the core of the angular inclusion showing Mn, S, and Fe as well as Si and O. **Phase 5**: Spectrum taken in the rim of the angular inclusion showing Mn, S, and Fe.

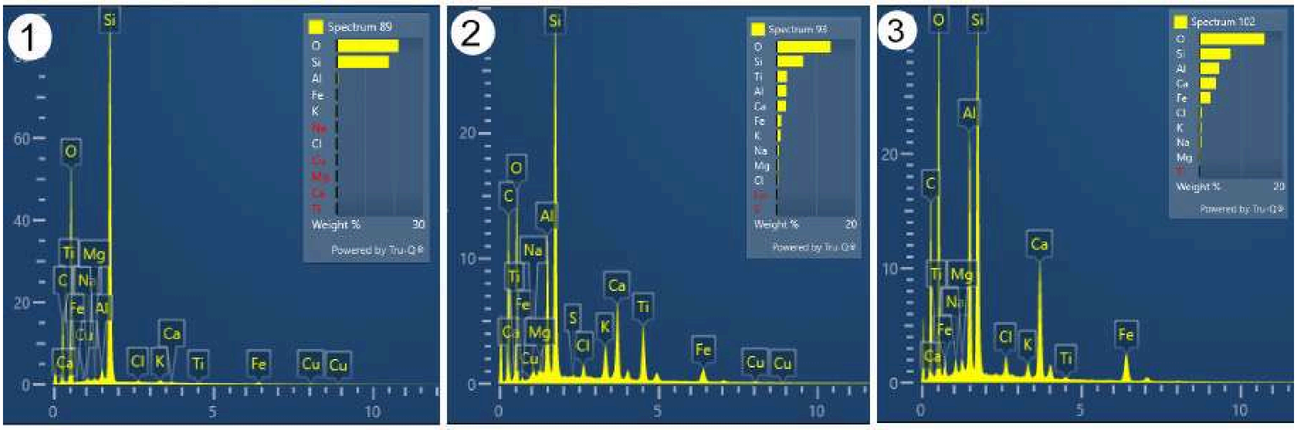

Figure 2. Sample ES-23-H4 - EDS-derived chemical profiles defined in Fig. 13.. Illustrating the range of different clastic grains. **Phase 1**: Quartz. **Phase 2**: Two phases are present: an aluminosilicate and possible TiO_2. **Phase 3**: Aluminosiclicate.

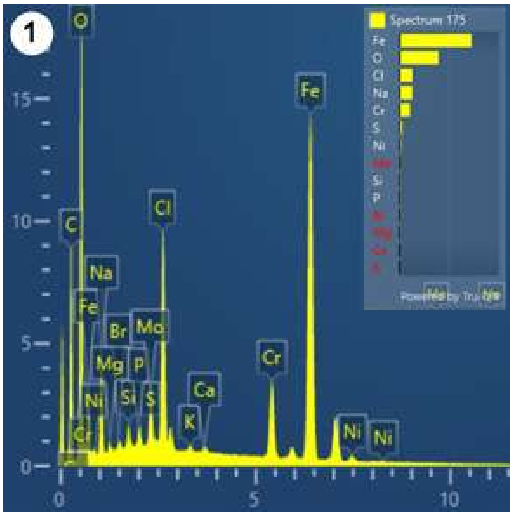

Figure 3: Sample ES-23-H5 - EDS-derived chemical profiles defined in Fig. 16. **Phase 1** found in sample ES-23-H5. Spectrum of iron-rich particle containing chromium and nickel, consistent with steel. The spectrum also picks up siliciclastic material and halite (NaCl) in the background (Phase 1).

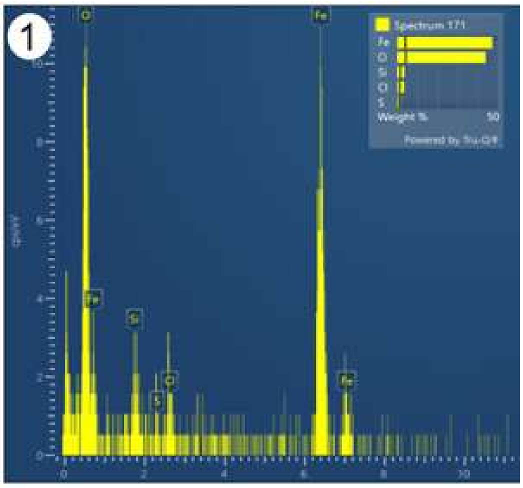

Figure 4. Sample ES-23-H6 - EDS-derived chemical profiles defined in Fig., 20. **Phase 1:** EDS-derived chemical profile of iron oxide encrusted filaments in ES-23-H6.

.

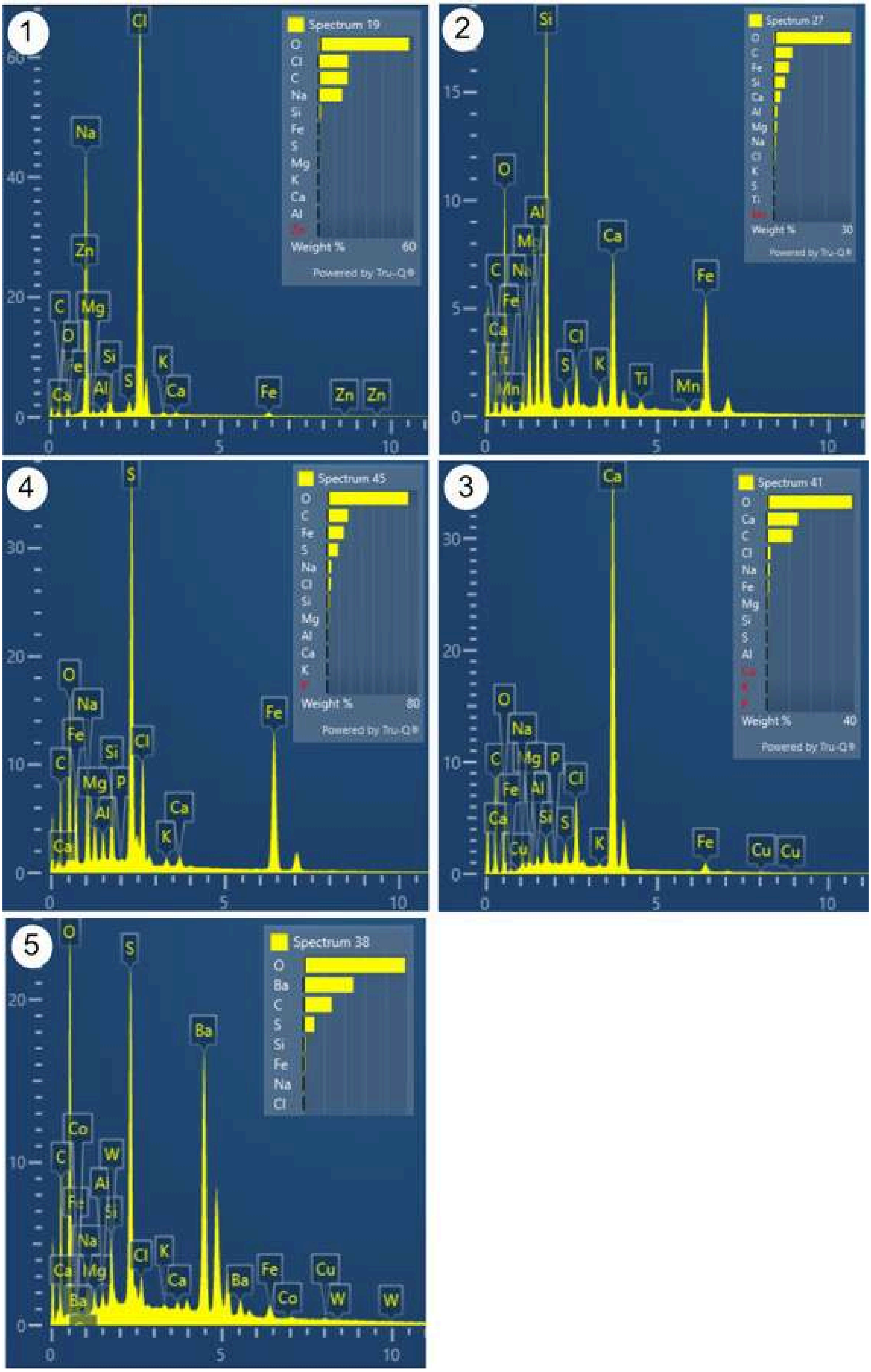

Figure 5. Sample ES-23-H7 - EDS-derived chemical profiles defined in Fig. 22. **Phase 1:** Halite (NaCl). **Phase 2:** **S**iliciclastic grains. **Phase 3:** Mg-bearing carbonate. **Phase 4:** Fe-S phase encrusting filaments. **Phase 5**: Baryte.

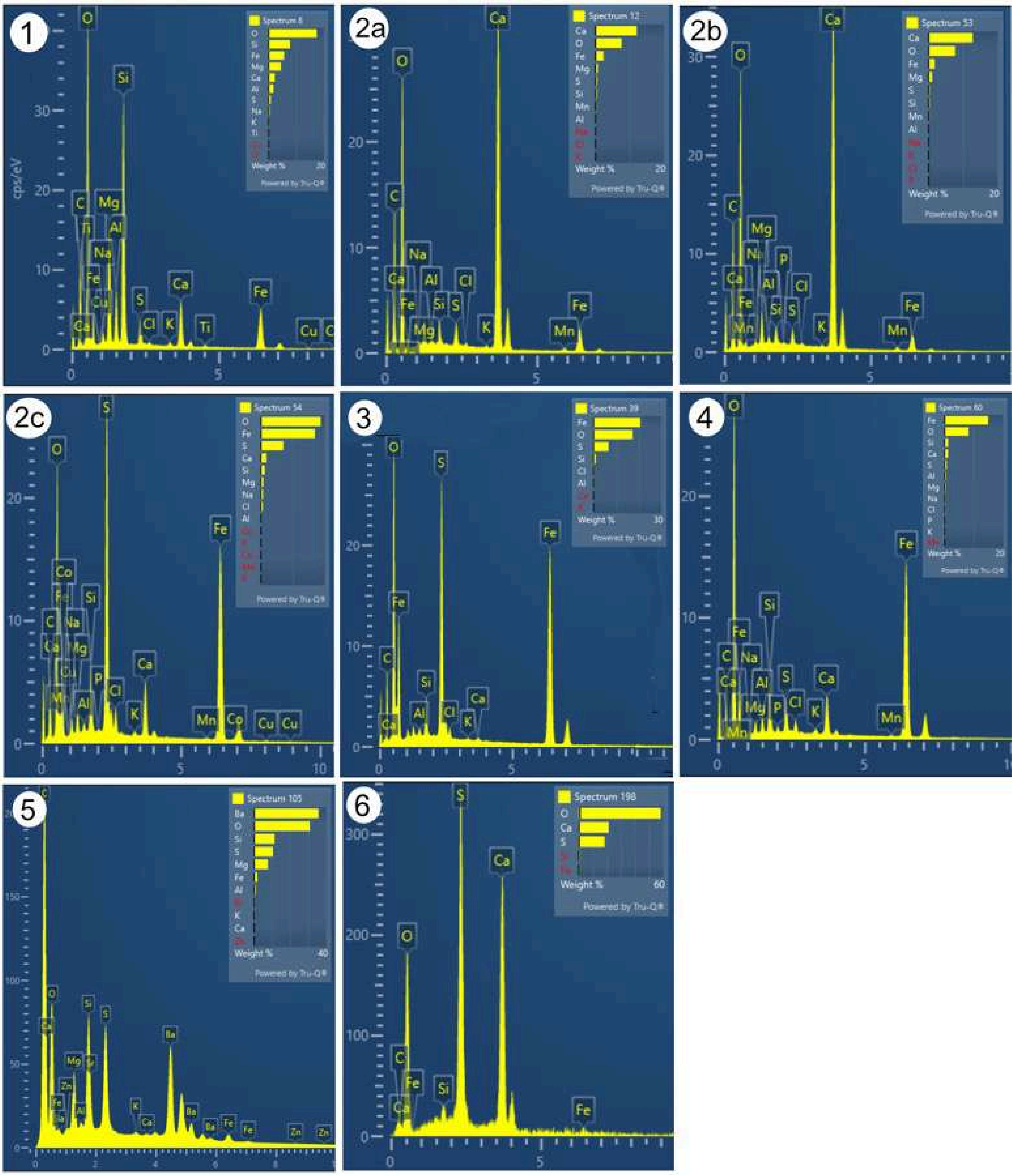

Figure 6. Sample ES-23-H1 - EDS-derived chemical profiles defined in Fig. 24. **Phase 1:** Silicate particle rich in magnesium, iron and calcium. **Phase 2a, 2b:** Calcium carbonate minerals rich in iron and magnesium (varying Ca:Fe and Ca:Mg ratios). **Phase 2c:** Iron-sulfate particles on top of the carbonate mineral. **Phase 3**: Rod-shaped iron-sulfate particles. **Phase 4**: Similar composition as Phase 3, but with less sulfur. **Phase 5:** Angular baryte particles. **Phase 6:** Gypsum.

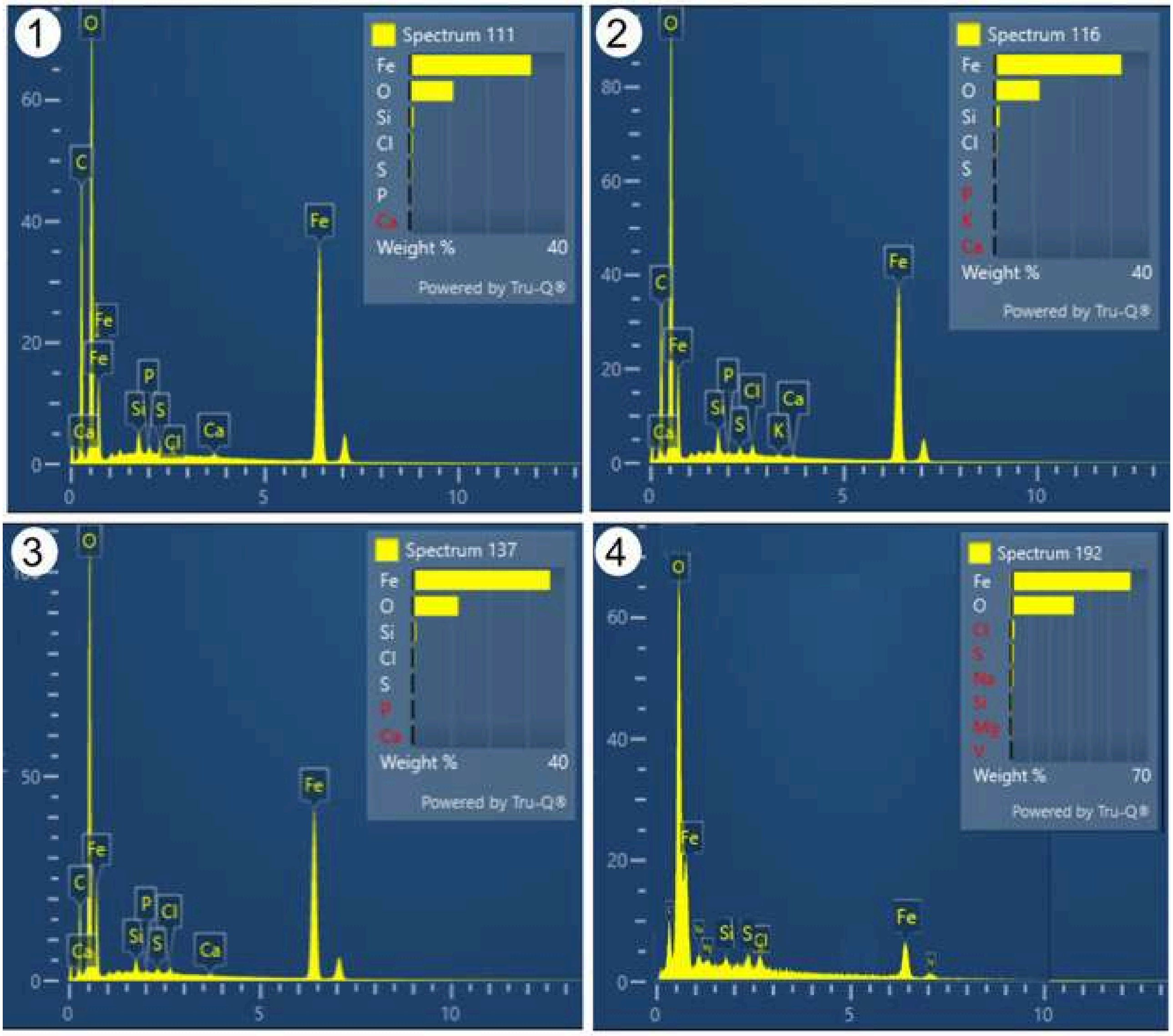

Figure 7. Sample ES-23-H2 - EDS-derived chemical profiles defined in Fig. 26, confirming the presence of iron-rich phases associated with the four microstructures in Fig. 32.

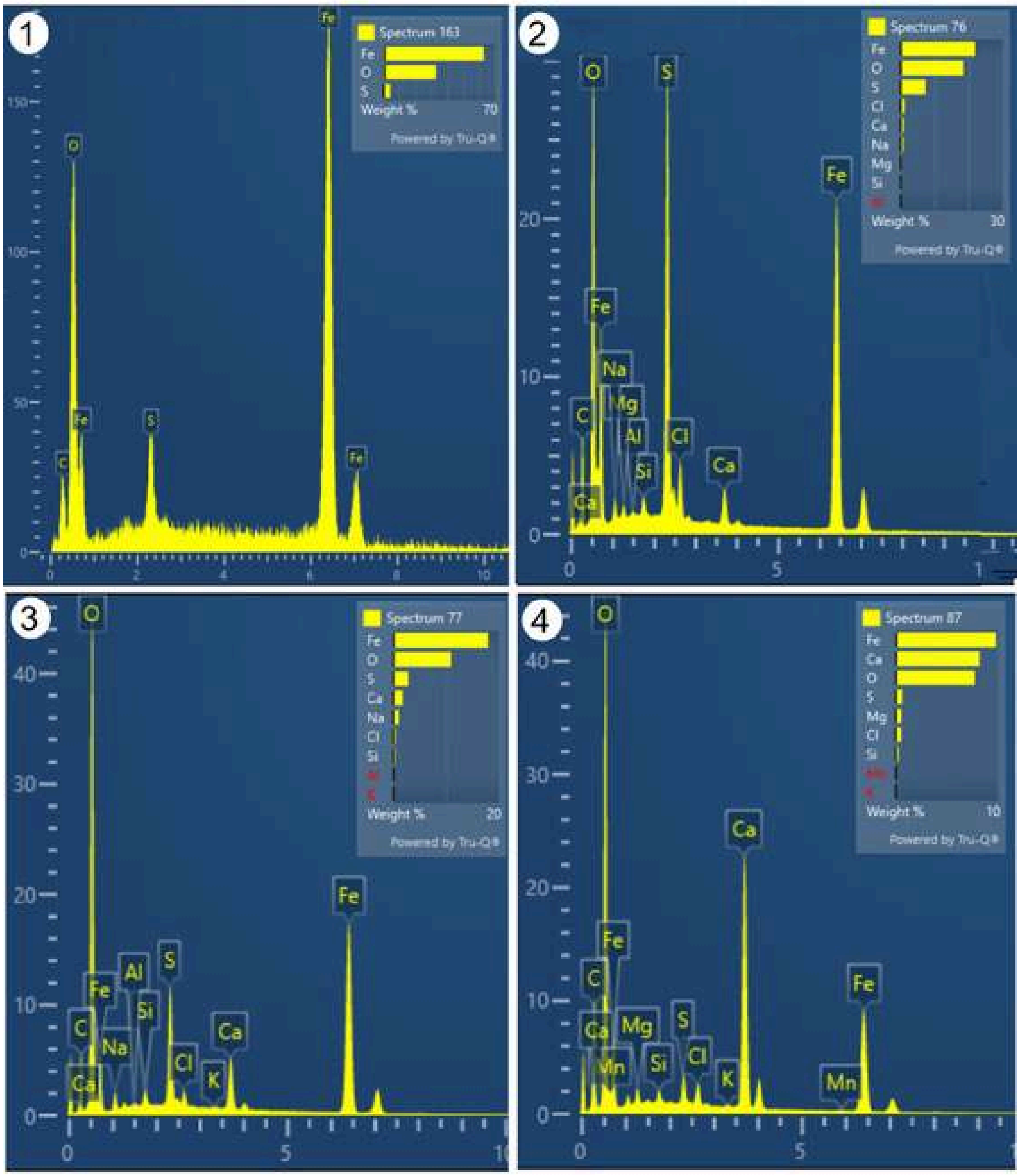

Figure 8. Sample ES-23-H3 - EDS-derived chemical profiles defined in Fig. 29. **Phase 1**: Iron oxides containing sulfur. **Phase 2**: Spherules mainly containing iron (Fe) and sulfur (S). **Phase 3:** Sulfur-bearing iron oxide. **Phase 4**: Calcium-iron carbonate with minor amounts of magnesium.

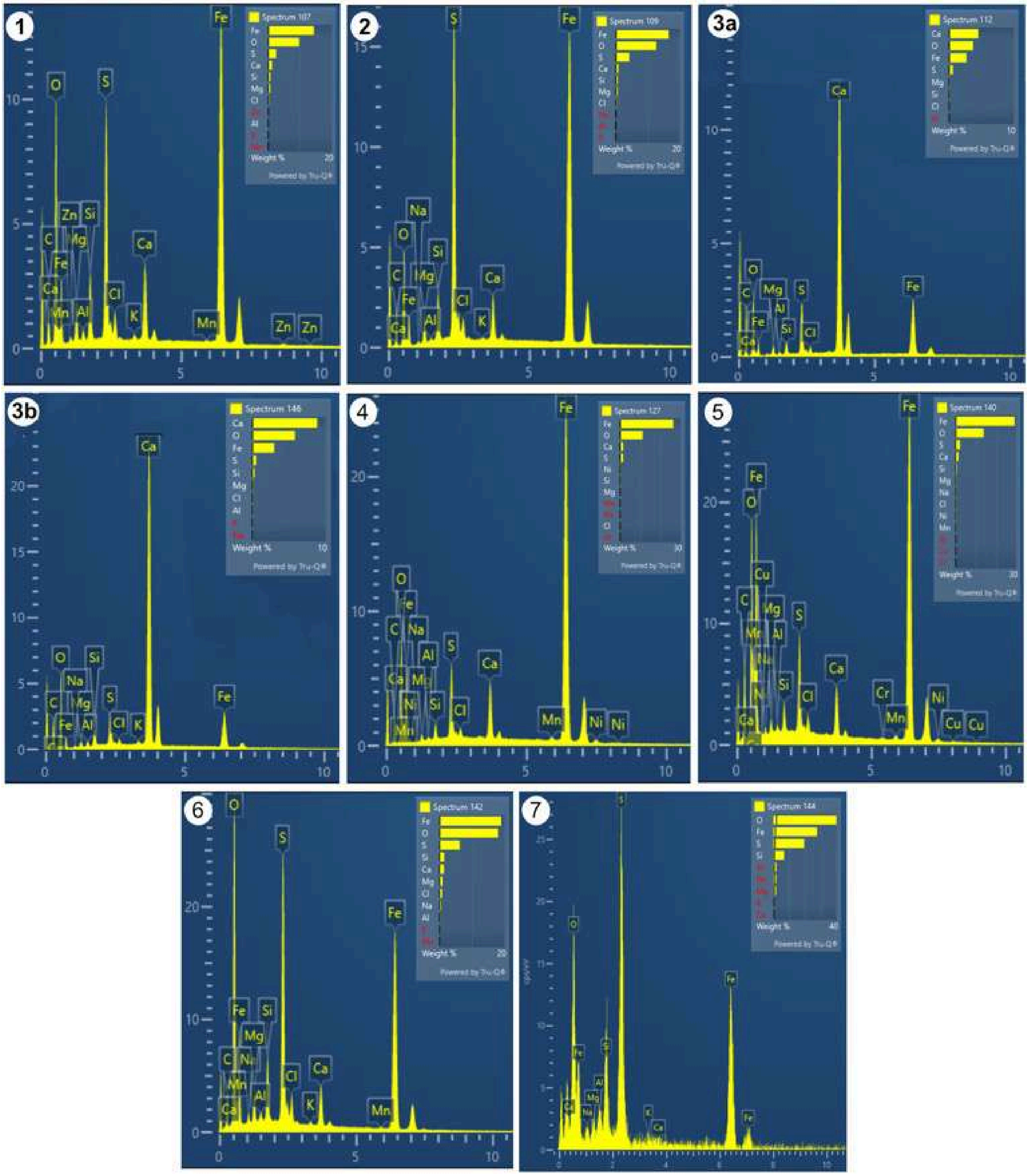

Figure 9. Sample ES-23-H10 - EDS-derived chemical profiles defined in Fig. 32. **Phase 1**. Matrix consisting of iron (Fe), oxygen (O) and sulfur (S). **Phase 2.** Matrix of similar composition as phase 1, but with higher concentrations of sulfur. **Phase 3a and 3b**: Carbonate minerals with varying Ca:Fe and Ca:Mg ratios. Phase 3a contains more iron and magnesium relative to calcium compared to phase 3b. **Phase 4**. Pearlitic steel fragment containing iron, oxygen and minor amounts of sulfur **Phase 5**. Degrading pearlitic steel structure showing higher level of sulfur compared to phase 4. **Phase 6**. Sulfur-enriched matrix associated with degraded steel fragments. **Phase 7**. Subcubic particles with high concentrations of sulfur and iron, consistent with iron sulfide minerals (e.g., pyrite).

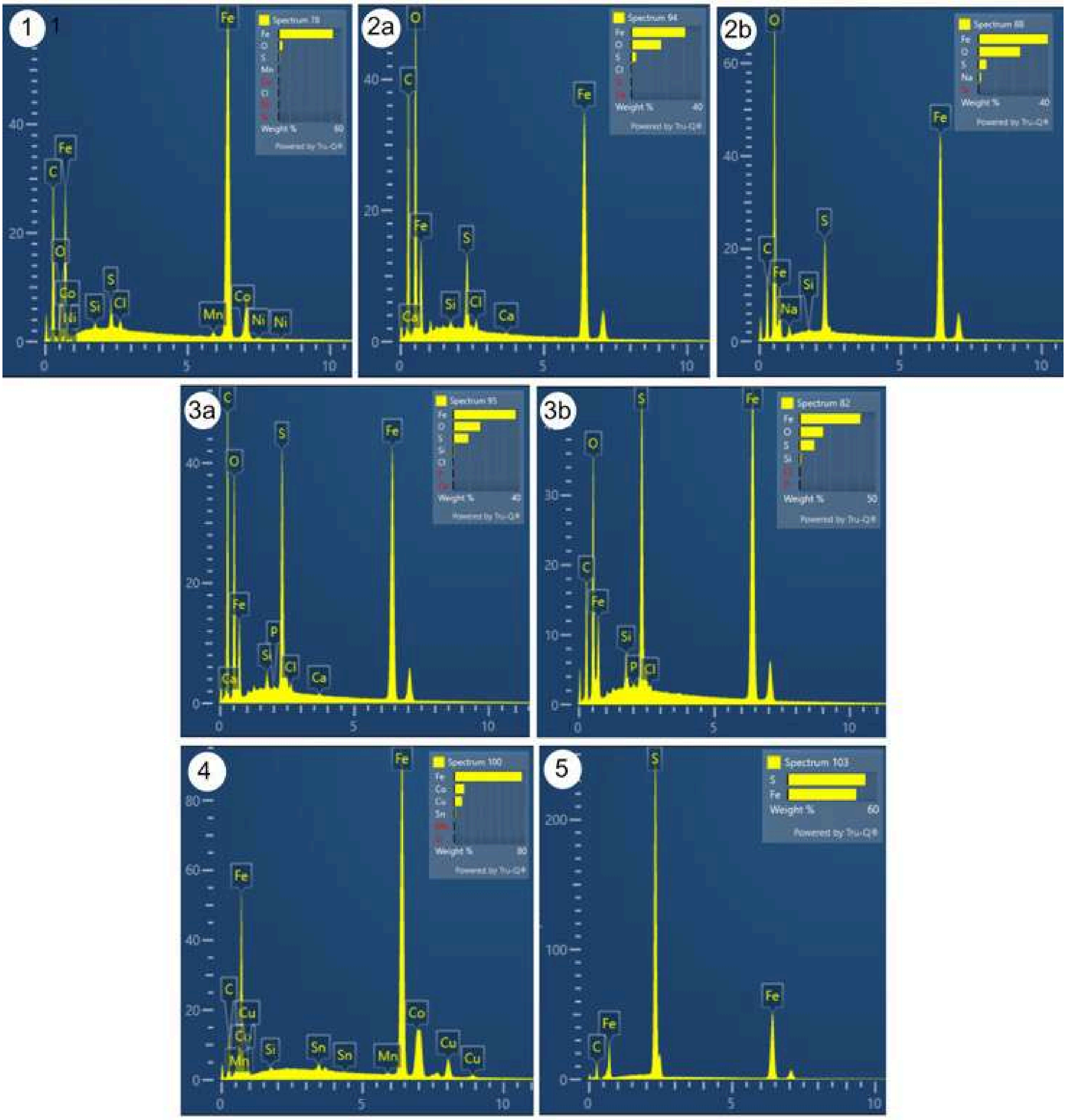

Figure 10. Sample ES-23-H13 - EDS-derived chemical profiles defined in Fig. 38. EDS-derived chemical composition of particles observed in sample ES-23-H13. **Phase 1**: Pearlitic steel fragment dominated by metallic iron. **Phase 2a, 2b:** Bladed crystals mainly containing iron and oxygen with minor amounts of sulfur. **Phase 3a, 3b**: Wad-like precipitates enriched in sulfur compared to the bladed crystals. **Phase 4:** Possible Paint fragment containing iron (Fe), Cobalt (Co) and (Cu), and traces of tin (Sn). **Phase 5**: Iron sulfides.

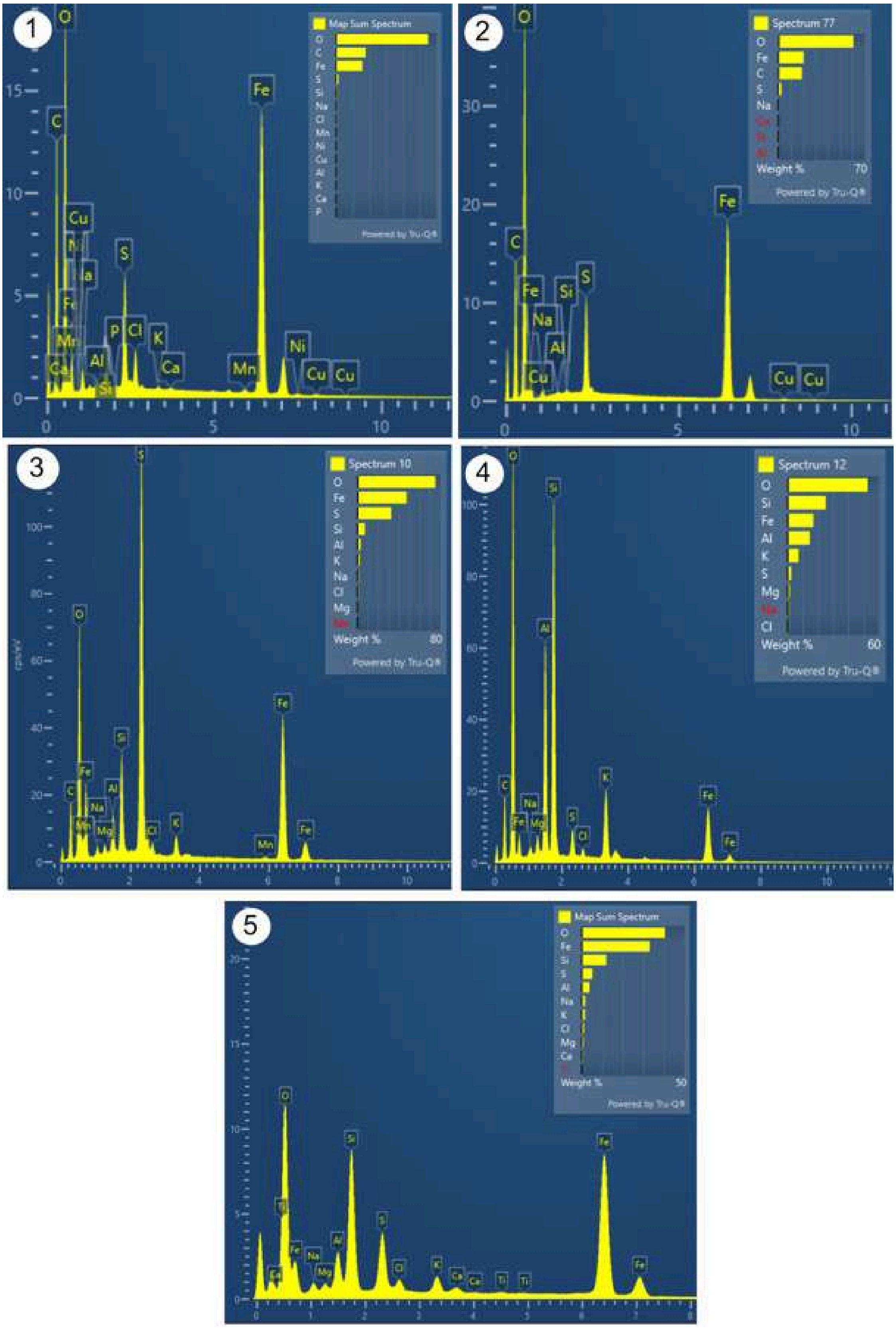

Figure 11. Sample ES-23-H8 - EDS-derived chemical profiles defined in Fig. 40. **Phase 1:** Spectrum represents an average of the entire area in Fig. 37A, which mainly consists of iron and oxide and to a lesser extent also sulfur. The carbon peak is mainly derived from the carbon stub upon which the sample was mounted and should therefore be disregarded in this spectrum. The analysis also shows traces of other elements linked to silicates (Si, Al, Ca), metals (Cu, Ni and Mn), as well as P. **Phase 2:** EDS of the pitted iron, oxide and sulfur particle. **Phase 3:** EDS showing the framboidal pyrite enriched in S and Fe. **Phase 4**: Evidence for an alumino-silicate particle. **Phase 5**: Sprectrum of the entire area showing enrichment in Fe and S. Si is related to silicate particles embedded in the filamentous structure.

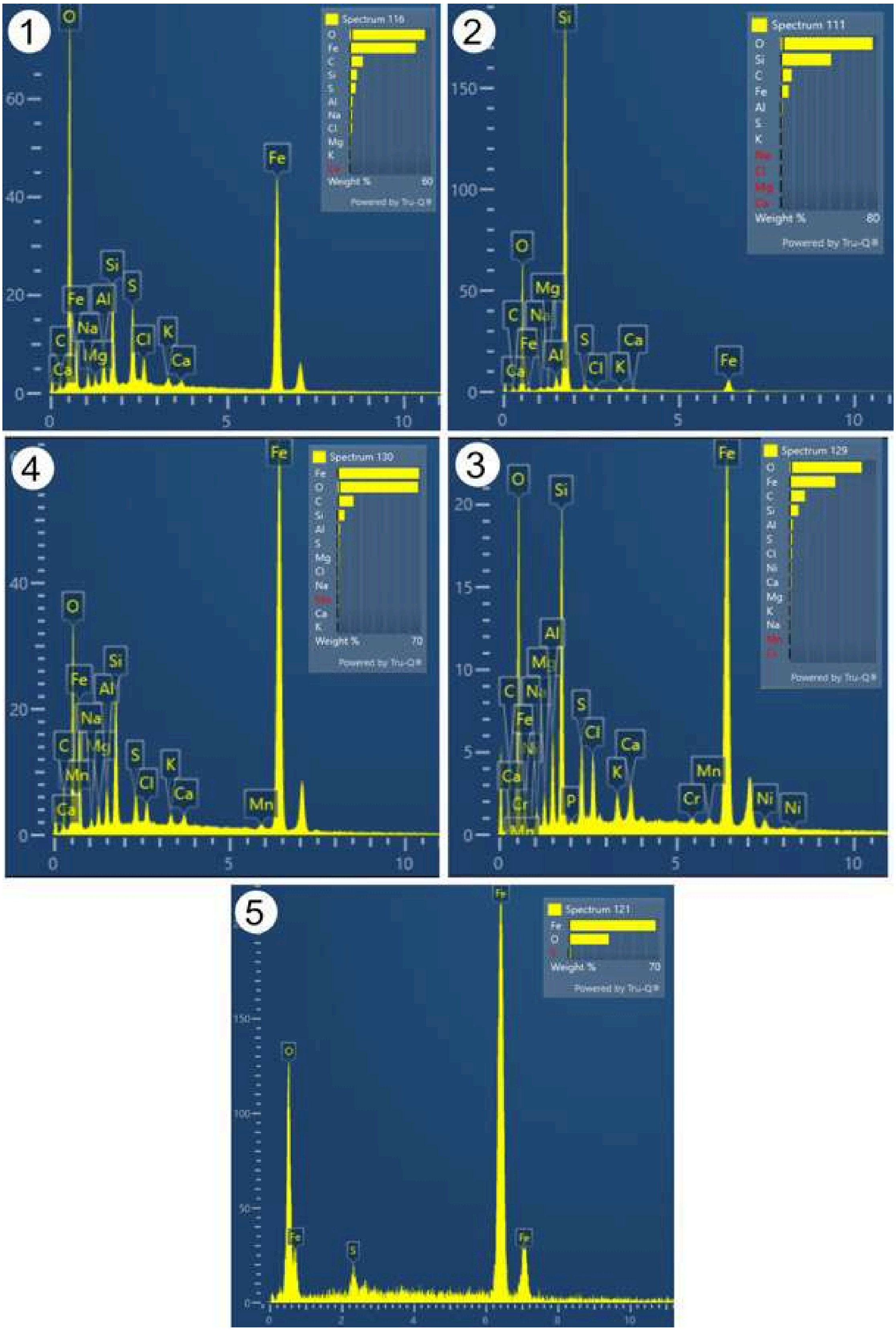

Figure 12. Sample ES-23-H9 - EDS-derived chemical profiles defined in Fig. 42. **Phase 1**: iron-oxides with minor amounts of sulfur. The silica (Si) signal is likely coming from the surrounding matrix. **Phase 2:** quartz (SiO_2) grain. **Phase 3:** iron-oxide matrix embedding the steel fragments. The silica signal indicates the proximity of siliciclastic particles**. Phase 4:** pearlitic steel containing iron (Fe) and oxygen (O). **Phase 5:** Platy mineral containing iron (Fe) and oxygen (O) and traces of sulfur (S).

MEDDELANDEN från STOCKHOLMS UNIVERSITETS INSTITUTION för GEOLOGISKA VETENSKAPER No 388

Rapportserie
ISBN 978-91-89107-42-7

No 387. Nosenzo, F.: Chemical and isotopic records of polycyclic histories in a subducted continental crust (Dora-Maira Massif, Western Alps). Stockholm 2023.

No 386. Muchowski, J.C.: Uncovering Ocean Mixing near Rough Bathymetry: Using Broadband Acoustics. Stockholm 2023.

No 385. Reed-Weidner, E.: The layer that did not swim away: Broadband acoustic discrimination and characterization of ocean stratification. Stockholm 2023.

No 384. Jakobsson, M., Stranne, C., Fornander, R., O’Regan, M., Wagner, A., and the EL21-Estonia Shipboard Party: EL21-Estonia – Report of the MS *Estonia* shipwreck site survey with RV Electra. Stockholm 2021.

No 383. West, G.: A multimethod approach to dating Quaternary sediments from the Arctic Ocean. Stockholm 2022.

No 382. Sjöström, J. Mid-Holocene mineral dust deposition in raised bogs in southern Sweden. Processes and links. Stockholm 2021.

No 381. Gdaniec, S. 231Pa, 230Th and 232Th as tracers of deep water circulation and particle transport. Insights from the Mediterranean Sea and the Arctic Ocean. Stockholm 2020.

No 380. Tollefsen, E. Experimental, petrological and geochemical investigations of ikaite (CaCO3·6H2O) formation in marine environments. Stockholm 2020.

No 379. Jansen, J. Carbon trace gas dynamics in subarctic lakes. Stockholm 2020.

No 378. Sjöberg, S. Microbially mediated manganese oxides enriched in yttrium and rare earth elements in the Ytterby mine, Sweden. Stockholm 2019.

No 377. Reghellin, D. Eastern equatorial Pacific bulk sediment properties and paleoceanography since the late Neogene. Stockholm 2019.

No 376. Bender, H. Assembly of the Caledonian Orogenic Wedge, Jämtland, Sweden. Stockholm 2019.

No 375. Hirst, C. Iron in the Lena river basin, NE Russia : insights from microscopy, spectroscopy and isotope analysis. Stockholm 2018.

No 374. Thiessen, F.K. The evolution of lunar breccias : U-Pb geochronology of Ca-phosphates and zircon using secondary ion mass spectrometry. Stockholm 2018.

No 373. Kielman, R. Assessing the reliability of detrital zircon in early-earth provenance studies. Stockholm 2018.

No 372. Hansman, R.J. Cryptic orogeny : uplift of the Al Hajar mountains at an alleged passive margin. Stockholm 2018.

Formerly/1990–2024: MEDDELANDEN från STOCKHOLMS UNIVERSITETS
INSTITUTION för Geologi och Geokemi (ISSN 1101-1599)
Department of Geological Sciences
Stockholms universitet SE-106 91 Stockholm www.geo.su.se

Department of Geological Sciences
Stockholms universitet SE-106 91 Stockholm www.geo.su.se